

**Progress Towards An Improved Quasiparticle
Camera In Superfluid $^3\text{He-B}$**

Tom Wilcox, MPhys (Hons.)

September 2019

A thesis submitted in fulfilment of the requirements of the degree of
Doctor of Philosophy
at Lancaster University

Abstract

The superfluid state, often obtained in the laboratory using liquid helium at very low temperatures, provides the basis for a wide range of interesting experiments. One large field of research relates to the study of turbulence in a superfluid, referred to as quantum turbulence due to the importance of quantum mechanical behaviour in the description of this phenomenon. An important experimental tool in the study of quantum turbulence is the mechanical resonator, with many different types of oscillator seeing use. Variations in the resonance can be related to the properties of the fluid through an understanding of the drag applied to the object.

The many seemingly disparate measurements reported here were performed in the hope of providing background for future development of improved experimental techniques. In an effort to develop an improved method for determining oscillator properties, measurements have been made using a multifrequency lock-in amplifier in superfluid ^4He . The results obtained show that the multifrequency lock-in can be used to obtain results equivalent to the traditional method while reducing the time required.

Due to the possibility of vastly increased sensitivity to changes in effective mass, tests were performed in ^4He using a new form of oscillator with a 100 nm by 100 nm square cross-section, significantly smaller than other available devices. The resonant frequency of these resonators, referred to as nanobeams, was varied from 0.6 MHz to 8.5 MHz by using beams of different length. Measurements of the resonator response as a function of temperature show that the beams can successfully probe the fluid, though the current theory is found to be insufficient to exactly quantify the dependence seen. A possible observation of turbulence generated by a nanobeam is also reported. Despite an observed critical velocity significantly different to theoretical predictions, all other measurements are consistent with a turbulent transition.

As the eventual goal is to use nanobeams for measurements in $^3\text{He-B}$, the drag on high

frequency oscillators in $^3\text{He-B}$ was also studied. Measurements on 4 devices of different frequencies found that the current model of damping remains adequate beyond the expected frequency limit for this model. Observations of anomalous increases in the damping for a single resonator in $^3\text{He-B}$ are also discussed. As this unexpected damping is only seen for small, sensitive resonators there is concern that similar effects could hinder interpretation of future nanobeam measurements in $^3\text{He-B}$. Efforts were made to understand the source of this damping, and hence explain why it is seen for only one of three nominally identical oscillators, though no conclusive explanation could be found.

Declaration

All research described in this thesis was performed collaboratively within the Lancaster University Ultra Low Temperature group. This thesis contains the author's own work and has not previously been submitted for a higher degree.

Publications

Some of the results described in this thesis are included in the following papers:

- Probing Liquid ^4He with Quartz Tuning Forks Using a Novel Multifrequency Lock-in Technique, D. I. Bradley, R. P. Haley, S. Kafanov, M. T. Noble, G. R. Pickett, V. Tsepelin, J. Vonka and T. Wilcox, *J. Low Temp. Phys.* **184**, 1080 (2016)
- Operating Nanobeams in a Quantum Fluid, D. I. Bradley, R. George, A. M. Guénault, R. P. Haley, S. Kafanov, M. T. Noble, Yu. A. Pashkin, G. R. Pickett, M. Poole, J. R. Prance, M. Sarsby, R. Schanen, V. Tsepelin, T. Wilcox and D. E. Zmeev, *Sci. Rep.* **7**, 4876 (2017)

Acknowledgements

As all of this research was performed within the Ultra Low Temperature research, thanks must go to my colleagues for their assistance. It is impossible to keep track of all the help provided, so I would like to extend a general thank you to all members of the group.

In particular I would like to thank my supervisor, Viktor Tsepelin, for his support and seemingly infinite patience. None of this would have been possible without his help.

Special thanks also go to Theo Noble, for working with me to keep the dilution fridge running for over a year. His help was invaluable both in terms of the experiments within the fridge and with the more mundane jobs required to keep it operational.

Finally I would also like to thank my family for supporting me throughout, in countless ways big and small.

Contents

1	Introduction	1
2	Theoretical Details	5
2.1	Helium 4	5
2.1.1	Superfluid Helium 4	5
2.1.2	Vorticity	8
2.1.3	Quantum Turbulence	13
2.1.4	Damping in Superfluid Helium 4	14
2.2	Helium 3	17
2.2.1	Liquid Helium 3	17
2.2.2	Superfluid Helium 3	20
2.2.3	Turbulence in Superfluid Helium 3	23
2.2.4	Excitations in Superfluid Helium 3	24
2.2.5	Drag in Helium 3	26
3	Experimental Methods	35
3.1	Oscillating Devices	35
3.1.1	Oscillator Theory	37
3.1.2	Current Driven Oscillators	42
3.1.3	Vibrating Wire Resonators	44
3.1.4	Nanobeams	45
3.1.5	Tuning Forks	47

3.2	Measurement Techniques	49
3.2.1	Frequency Sweep	50
3.2.2	Resonance Tracking	52
3.2.3	Amplitude Sweep	53
3.2.4	NEMS Measurements	53
3.2.5	Multifrequency Measurement Methods	57
3.3	Thermometry	59
3.4	Experimental Cell Layouts	64
4	Multifrequency Lock-in Measurements	66
5	Probing Superfluid ^4He with Nanomechanical Resonators	75
6	Frequency Dependence of Thermal Drag in $^3\text{He-B}$	92
7	Anomalous Damping of a Wire Resonator in Superfluid $^3\text{He-B}$	107
7.1	Expected Damping in Superfluid $^3\text{He-B}$	107
7.2	Observed Deviations from Expected Damping	108
7.3	Potential Physical Explanations	112
8	Conclusions	119

List of Figures

1.1	Photograph of the Quasiparticle camera array	3
2.1	Normal and superfluid fractions in ^4He as a function of temperature	7
2.2	Landau's dispersion relation for ^4He	8
2.3	Example Fermi-Dirac distribution function	18
2.4	Dispersion curve for superfluid $^3\text{He-B}$	25
2.5	Shifted Dispersion curve for $^3\text{He-B}$ in the presence of superfluid flow	28
3.1	SEM image of a sample doubly-clamped beam	46
3.2	Example f-sweep results	51
3.3	Thermal width of wire mmm2 plotted against thermal width of wire mmm1	62
3.4	Thermal width of wire Mg plotted against thermal width of wire mmm2.	63
3.5	Diagram of the devices inside the cell used for all ^3He measurements.	65
4.1	In-phase resonance component as measured using frequency combs	67
4.2	Schematic of the circuit used for MLA measurements	69
4.3	Comparison between frequency sweep and frequency comb measurements of a resonance	70
4.4	Resonance width as a function of temperature, measured with both MLA and SR830	72
4.5	Frequency ratio as a function of temperature, measured with both MLA and SR830	73
4.6	Frequency ratio as a function of temperature, measured with both MLA and SR830, treating vacuum frequency as a fitting parameter	74

5.1	NEMS output power as a function of frequency, measured at a range of different input powers	77
5.2	NEMS velocity as a function of frequency at a range of temperatures	78
5.3	Comparison between experiment and theory for the frequency shift observed as the helium temperature changes	80
5.4	Comparison between experiment and theory for the change in width measured as the cryostat is cooled	81
5.5	Calculated values of viscous penetration depth for the 50 μm beam as a function of temperature	83
5.6	Width as a function of normalised frequency ratio for beams of different length	85
5.7	Width as a function of temperature for the 75 μm long beam	86
5.8	Device velocity as a function of force for the 25 μm beam	89
5.9	Raw frequency sweep data as measured in vacuum and in superfluid	90
6.1	Intrinsic Force-Velocity plots for the four devices used	96
6.2	Force-Velocity plots for Mg at a range of temperatures	97
6.3	Force-Velocity plots for D2ov1 at a range of temperatures	98
6.4	Thermal force as a function of peak velocity for D2ov1 results taken at a range of temperatures	100
6.5	Thermal force as a function of peak velocity for Mg results taken at a range of temperatures	101
6.6	Reduced Force-Velocity plot for D2ov1	103
6.7	Combined plot of reduced Force-Velocity data taken for all 4 devices	105
6.8	Lambda as a function of normalised frequency for a range of devices	106

7.1	Force-Velocity plot for mmm3, showing expected damping	108
7.2	Force-Velocity plot for vibrating wire mmm1, showing unexpected increases in the damping	109
7.3	Derivative of force with respect to velocity for the mmm1 data	111

1 Introduction

When thinking about classical physics from a modern perspective, it is tempting to assume all the answers are already known. Further consideration reveals this is not the case, with the problem of fluid turbulence in particular far from being solved. It may however be possible to obtain a deeper understanding by considering similar problems in superfluids, as the quantum nature of these systems places restrictions on the motion of the fluid. Rotational flow is only possible in the form of vortex lines with quantised circulation, so all turbulent motion must be describable in terms of the interactions of a large number of these lines. Due to the importance of this quantisation, turbulence in superfluids is typically referred to as quantum turbulence [1, 2].

The range of superfluid systems accessible by experiments is highly limited, with liquid helium at very low temperatures historically providing the only experimentally accessible superfluid system [3–6]. However, recently atomic Bose-Einstein condensates have emerged as an alternative system for experiments involving superfluids [7, 8]. Despite these recent breakthroughs, all our experiments are performed in liquid helium to take advantage of the wealth of prior research performed on this system.

To understand how the liquid state is maintained at these low temperatures, we must consider the quantum mechanical properties of helium. Due to the full outer shell of electrons, the interatomic forces between helium atoms are very weak. In addition to this, helium has a large zero point energy due to its low mass. The combination of these effects means helium never solidifies under atmospheric pressure. Helium can therefore be cooled to temperatures at which quantum effects become relevant while still in the liquid state. As quantum effects become important the two stable isotopes of helium, ^3He and ^4He , begin to behave very differently. Due to the different numbers of nuclei, a single ^3He atom is a fermion, while the extra neutron means each ^4He atom is a boson. Since fermions and bosons are described by entirely different statistics this leads to drastic differences in their

quantum mechanical behaviour. These differences will be discussed in detail in sections 2.1 and 2.2.

One of the most promising methods of investigating quantum turbulence only works in superfluid ^3He as the fermionic nature of this isotope leads to a more complex superfluid state with a larger number of possible excitations. Interactions between these excitations and the vortex lines in superfluid ^3He can be studied to obtain information about the vorticity. The excitations, referred to as quasiparticles, undergo Andreev reflection when approaching vortex lines, a process that results in perfect retroreflection of the excitation particle with minimal momentum transfer to the vortex line. Properties of the turbulence can then be derived from effects caused by the reflection of excitations incident on the vorticity [9–11]. The lack of momentum transfer between excitation and vortex means this is a non-invasive measurement technique, and so allows us to study the vorticity without affecting it.

The most advanced application of this technique uses a 5×5 array of excitation detectors as a rudimentary camera, referred to as the quasiparticle camera, in an effort to produce images of vortex lines [12]. A photograph of this array is shown in figure 1.1.

All five pixels in a row are driven using a common electrical line, with these common connections clearly visible in figure 1.1. By using a summation amplifier to combine signals from five different generators and ensuring every fork on a common line has significantly different resonant frequencies this method can be used to reduce the amount of wiring required without any loss in measurement performance.

Another critical component required to operate the quasiparticle camera is a black-body radiator, placed in front of the detector. This radiator consists of two vibrating wire resonators placed inside a box with a single small aperture. One wire is driven to a high velocity to produce a large number of thermal excitations. This rapidly creates a large number of thermal excitations within the box, this then creates a beam of these excitations

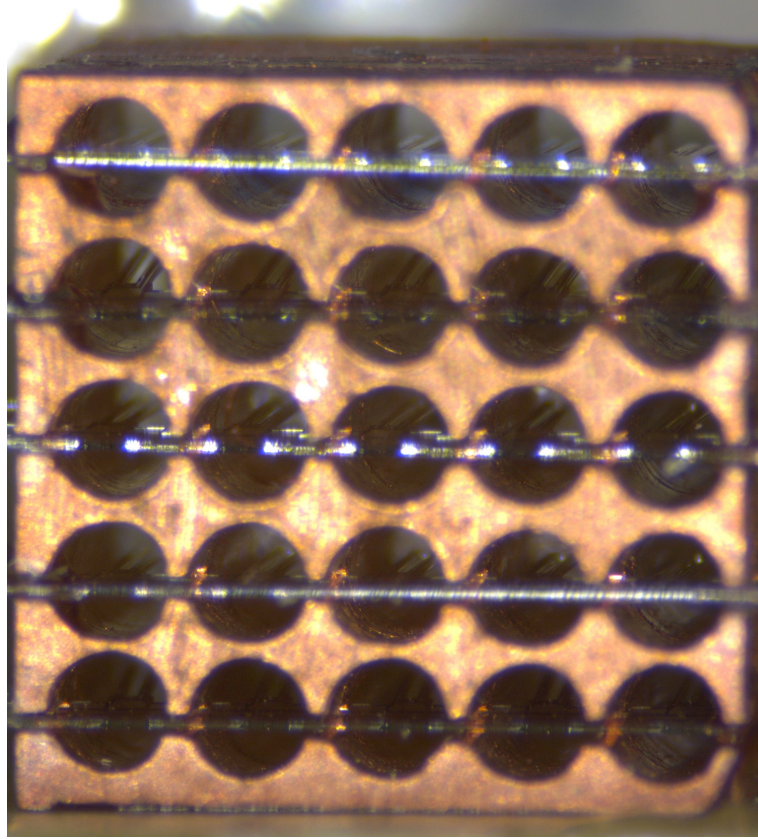


Figure 1.1: Photograph of the reverse of the quasiparticle camera array. The camera was made by drilling a 5×5 array of holes into a copper block and placing a tuning fork within each hole.

as they exit the box through the aperture. The second wire is used as a thermometer to measure the temperature within the box and so quantify the amount of energy contained within the beam. An additional thermometer placed in the bulk fluid allows comparison of the temperatures inside and outside the box.

A fourth wire, placed between the detector array the black-body radiator, can then be used to generate vorticity. This vorticity causes some of the thermal excitations to undergo Andreev reflection, reducing the number of quasiparticles that reach the array. By comparing these results to a fixed reference, calculated for each detector in the absence of vorticity, the percentage of incident excitations reflected by the vorticity can be calcu-

lated individually for each detector. As a higher vorticity density corresponds to a larger number of excitations reflected, this data can then be used to reconstruct a rough image of the vorticity.

The first test of the quasiparticle camera serves as a successful demonstration of the concept, with the damping experienced by the pixels clearly observed to decrease when the vorticity generator is activated [12]. With analysis of further data obtained using the original camera currently ongoing, planning has begun on possible improvements that could be applied to a second generation camera.

In this thesis, details are given of seemingly disparate results that will hopefully lay the groundwork for this second generation camera. First, in section 4, we discuss a novel new method of operating the detectors used as the camera pixels. Depending on the method of operation used, the new approach could either reduce the time taken per measurement or allow more detectors to be operated with a single instrument. This could provide either a greater time sensitivity or greater number of pixels respectively.

In section 5 we describe measurements of superfluid ^4He taken using nanomechanical oscillators, proving that these nanoscale structures can be used to successfully measure the properties of a superfluid. This demonstrates that these devices are suitable for use as detectors in the quasiparticle camera. Due to the tiny size of these oscillators, it should be possible to reduce the spacing between camera pixels and therefore produce a next generation quasiparticle camera with vastly improved spatial resolution.

Finally, we describe a range of results that may prove useful in anticipating the response of nanomechanical oscillators in superfluid ^3He . In section 6, we discuss results comparing measurements of the drag obtained using a range of different oscillations. As the theory used to explain this drag only applies below a certain frequency, these measurements were intended to study what happens when this frequency limit is approached. As nanomechanical oscillator operate at much higher frequencies than the traditional oscillators, it is

possible that they will also exceed the frequency limit of the theory and so understanding this limit will likely prove useful when these devices are used in superfluid ^3He .

Section 7 details a series of measurements that show anomalous damping of an oscillator in ^3He , with the damping observed unexplainable in terms of the current theory. These results do have precedent, with similar anomalies reported previously. These discrepancies appear to be more likely to occur with highly sensitive oscillators, and so are liable to be an issue when nanomechanical oscillators are used for measurements in ^3He .

Before these discussions of the experiments, a wide range of relevant supporting information is provided. Section 2 covers the important theoretical underpinning of the experiments performed. The practical methods used are then described in section 3.

2 Theoretical Details

Due to the quantum nature of phenomena at very low temperatures, there are many significant differences between the properties of ^4He and ^3He under these conditions. Both isotopes were used for different parts of these experiments, and so the properties of both will be discussed. As the simpler case, we start by describing the properties of ^4He .

2.1 Helium 4

2.1.1 Superfluid Helium 4

As the vastly more common isotope, all early experiments involving helium were performed on this isotope. Though highly uninteresting from a chemical perspective, helium became important to low temperature research when it was discovered that helium only liquifies at a temperature of 4.2 K. The unexpected potential of liquid helium was revealed by the discovery of zero viscosity motion in the fluid, observed below a transition temperature of approximately 2.17 K at saturated vapour pressure [13,14].

A theoretical explanation of these unusual properties was then provided by the two-fluid model [15,16]. This model explained the behaviour observed by treating the helium as a mixture of two interpenetrating, non-interacting fluids. The normal fluid, defined by the density ρ_N , behaves like a classical fluid with finite viscosity. In contrast the superfluid component, with density ρ_S , has zero viscosity and zero entropy. As both components must be accounted for in the overall helium density ρ_{He} , a simple expression for the densities can be written:

$$\rho_{\text{He}} = \rho_N + \rho_S. \quad (2.1)$$

The densities of the different fluid components are highly temperature dependent, with the fluid changing from entirely normal fluid at the transition to become completely superfluid at zero temperature. The relative fluid densities as a function of temperature are shown in figure 2.1.

The nature of the superfluid fraction can be explained by considering Bose-Einstein condensation [17]. When applied to gases of bosons, Bose-Einstein statistics show that cooling these bosons below some transition temperature causes the majority of the particles to condense into the ground state. The Bose-Einstein condensate that forms is then described by a macroscopic wavefunction. At non-zero temperatures there will always remain a finite number of bosons above this ground state which are not described by the macroscopic wavefunction and therefore account for the normal fluid component.

Although we cannot apply Bose-Einstein statistics directly to ^4He , the properties of the superfluid can be well explained by considering the same concepts. By assuming that the superfluid fraction is analogous to a Bose-Einstein condensate, we can define a macroscopic wavefunction Ψ for this fraction,

$$\Psi = |\Psi_0| \exp(i\theta), \quad (2.2)$$

where Ψ_0 is the amplitude of the wavefunction and θ is a macroscopic phase.

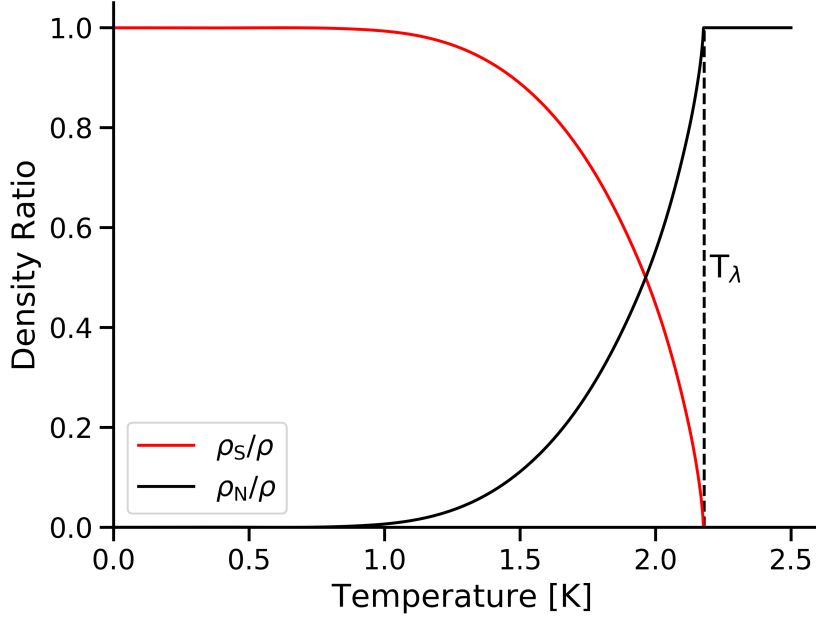


Figure 2.1: Normal and superfluid fractions in ^4He as a function of temperature. Note that below 1 K the fractions barely change, with the fluid consisting of almost exclusively superfluid in this range.

In addition to this, Landau showed that a gap was required in the dispersion curve for the superfluid state to remain stable as the fluid moves [16]. Without this gap there would be zero energy barrier to excitation production during motion of the fluid and superfluidity would rapidly break down in response to the slightest motion. An example of the simplest possible dispersion curve that satisfies this condition is given in figure 2.2. The gap energy is labelled Δ and occurs at a momentum of p_0 .

This dispersion curve then introduces the Landau velocity, v_L , defined as the lowest velocity which intersects the dispersion curve, $v_L = \frac{\Delta}{p_0}$. Above this velocity excitations are produced, with the energy needed to produce these excitations being taken from the moving object, resulting in the loss of kinetic energy from the object and so causing a large

increase in the drag.

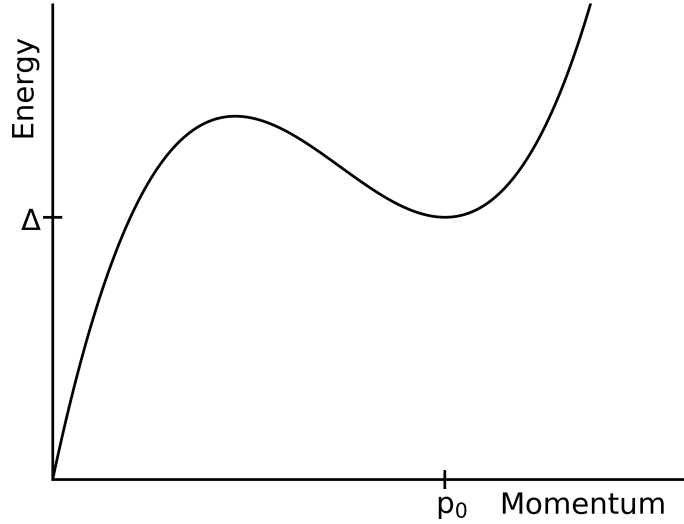


Figure 2.2: Landau's dispersion relation for ${}^4\text{He}$, defined by the minima at momentum p_0 and energy Δ .

However, all experiments measuring the drag on macroscopic objects in ${}^4\text{He}$ contradict this, finding that drag increases sharply well below the Landau velocity [18–21]. To explain this discrepancy requires an alternative drag mechanism in the superfluid. Through comparisons to classical fluid dynamics, the most obvious explanation for this additional drag would be the generation of turbulence.

2.1.2 Vorticity

At first glance, a simple argument would appear to suggest that vorticity is impossible in a superfluid, preventing the formation of more developed turbulence. To start, we define superfluid vorticity ω_S as a way to quantify rotational flow,

$$\omega_S = \nabla \times \mathbf{v}_S, \quad (2.3)$$

where \mathbf{v}_S is the velocity field for the superfluid. To obtain the superfluid velocity, we can apply the quantum mechanical momentum operator $\hat{p} = -i\hbar\nabla$ to the macroscopic superfluid wavefunction. When used with the definition of momentum $\mathbf{v} = \frac{\mathbf{p}}{m}$ this gives:

$$\mathbf{v}_S = \frac{\hbar\nabla\theta}{m}. \quad (2.4)$$

This can then be used in the expression for vorticity,

$$\omega_S = \frac{\hbar}{m}(\nabla \times \nabla\theta). \quad (2.5)$$

From the mathematical definitions, it is known that the curl of the gradient of a scalar field is always zero. Hence $\nabla \times \nabla\theta$ is zero for all values of θ , the vorticity must always be zero and the superfluid flow is therefore irrotational.

The same result can be also be obtained by considering the circulation, κ , defined as a line integral of the velocity over any closed path in a simply connected volume:

$$\kappa = \oint \mathbf{v}_S \cdot d\mathbf{l}, \quad (2.6)$$

where \mathbf{l} is the line element for the closed path chosen. For a singly connected line this can then be converted into a surface integral by applying Stokes' Theorem:

$$\kappa = \int \nabla \times \mathbf{v}_S \cdot d\mathbf{S}, \quad (2.7)$$

where \mathbf{S} is the surface element for the surface bounded by the line l . By applying the previously proven condition $\nabla \times \mathbf{v}_S = 0$ we find that the circulation must be zero, further supporting the condition that the superfluid flow must be irrotational.

This calculation becomes more complex if we instead consider a multiply connected volume

such as an annulus of fluid. Equation 2.6 still applies, but Stokes' Theorem is no longer valid. Instead, we can substitute equation 2.4 into equation 2.6,

$$\kappa = \frac{\hbar}{m} \oint \nabla\theta \cdot d\mathbf{l}. \quad (2.8)$$

To preserve the macroscopic wavefunction required for superfluidity the wavefunction must remain single-valued on full rotations around the loop. Therefore, the phase change on a full rotation around the loop must be an integer multiple of 2π . Using this we can solve the line integral in equation 2.8:

$$\oint \nabla\theta \cdot d\mathbf{l} = 2\pi n, \quad (2.9)$$

$$\kappa = \frac{h n}{m}. \quad (2.10)$$

We therefore see that rotational flow is indeed possible in superfluid, but only for multiply connected volumes and only if the circulation of the flow is quantised in units of $h/m = 9.97 \times 10^{-8} \text{ m}^2\text{s}^{-1}$.

To explain how these vortices can be created in bulk superfluid, we must first derive an alternative expression for the superfluid velocity flow due to a vortex. This expression can be obtained by considering equation 2.6 for the case of a circular line element centered on the core of the vortex.

Due to the nature of the rotational flow around a straight vortex, the superfluid velocity cannot have a radial component and so will be parallel to the line element at all points. The dot product of these quantities is therefore equal to the product of their magnitudes. From symmetry considerations, the superfluid velocity will be the same at all points along the line element, and so can be removed from the integral:

$$\kappa = v_S \oint dl, \quad (2.11)$$

where v_S and dl are the magnitudes of the superfluid velocity and the line element. Since integrating over just the line element gives the length of that line, this expression can be simplified further by replacing the integral with the circumference of the circular path considered,

$$\kappa = 2\pi r v_S. \quad (2.12)$$

Equation 2.12 can then be rearranged to find the superfluid velocity profile as a function of the radial distance from the center of the vortex,

$$v_S = \frac{\kappa}{2\pi r}. \quad (2.13)$$

Equation 2.13 shows that the superfluid velocity increases asymptotically as the distance from the vortex centre decreases. There will therefore be a point close to the centre of the vortex where the superfluid velocity exceeds the Landau velocity, meaning the superfluid state cannot exist within this volume, referred to as the vortex core. The core then creates the multiply connected geometry required, with the superfluid vorticity occurring around this. The size of this core can then be estimated by rearranging equation 2.13:

$$r_0 = \frac{\kappa}{2\pi v_L}. \quad (2.14)$$

By substituting known values for the circulation quantum and Landau velocity, equation 2.14 predicts the radius of the vortex core is on the order of $r_0 = 0.1$ nm.

In experiments performed on steadily rotating volumes of ^4He , a hexagonal lattice of vortex

filaments appears and the overall behaviour closely mimics that of a classical fluid [22,23]. This observation can be explained by considering the kinetic energy per unit length of a vortex line, labelled ϵ . An expression for the energy of the vortex line can be obtained by integration:

$$\epsilon = \int_a^b \oint \frac{1}{2} \rho_S v_S^2 dl dr, \quad (2.15)$$

where the integral dl is the line integral around the vortex and the integral dr integrates radially from the outside of the vortex core a to some upper cutoff b . For the case of a single vortex this cutoff is given by the size of the container. If multiple vortices are present, the cutoff is instead given by the average spacing between vortices. Removing constants from the integral and substituting the expression for the superfluid velocity gives:

$$\epsilon = \frac{1}{2} \rho_S \int_a^b \oint \left(\frac{\kappa}{2\pi r} \right)^2 dl dr. \quad (2.16)$$

Symmetry considerations state that all quantities involved must be invariant under rotation, which simplifies things further:

$$\epsilon = \frac{\rho_S \kappa^2}{8\pi^2} \int_b^a \frac{1}{r^2} \oint dl dr. \quad (2.17)$$

As has already been shown when obtaining the expression for the superfluid velocity profile around the vortex, the line integral can now be replaced with the circumference of the line, $2\pi r$:

$$\epsilon = \frac{\rho_S \kappa^2}{4\pi} \int_b^a \frac{1}{r} dr. \quad (2.18)$$

Solving the remaining integral then gives:

$$\epsilon = \frac{\rho_S \kappa^2}{4\pi} \ln \left(\frac{b}{a} \right). \quad (2.19)$$

The experimental observations of vortex lattices in ^4He are easily explained by applying energetic arguments to equation 2.19. Due to the factor of κ^2 singly quantised vortices are energetically favourable and therefore a lattice of vortices is the only stable configuration.

2.1.3 Quantum Turbulence

As rotational flow in superfluid ^4He can only exist in the form of singly quantised vortex lines, superfluid turbulence must also be explained in terms of these vortices. The chaotic flow patterns characteristic of turbulence can only be created by a disorganised tangle of vortex lines.

In ^4He , two distinct types of quantum turbulence exist. The first to be observed, referred to as counterflow turbulence, is created when the flow of the normal and superfluid components are in antiphase [3,4]. This counterflow arises as a means of heat transport, with the normal fluid component carrying the heat and an equal and opposite flow of superfluid component ensuring there is no overall mass flow. Counterflow turbulence is then produced when the relative velocity between the two components exceeds some critical value.

The other possible form, generated by the motion of objects immersed in the fluid, is much more closely analogous to classical turbulence. A wide variety of different objects have been used in experiments on this form of turbulence, ranging from large rotating disks [6] to wire resonators [24,25] and quartz tuning forks [26]. Intriguingly, this form of superfluid turbulence can be shown to have significant similarities with the classical case [6,21,27].

Since the existence of the turbulent state requires a large number of vortex lines, a mechanism for generating a large number of lines is necessary for turbulence to exist. Exper-

iments have shown that generating turbulence in ^4He is highly dependent on remanent vortices [28]. These remanent vortices remain stable even in stationary superfluid and exist as small lengths of vortex line pinned to the microscopic roughness of objects in the fluid or the walls of the cell [29]. The remanent vortices then expand back into full vortex lines when exposed to flow above a certain velocity, causing the transition to turbulence [30]. It is this mechanism, and this form of turbulence, that accounts for the large amounts of drag observed below the Landau velocity.

The ease of generating quantum turbulence implies that these remanent vortices are present in almost all samples of superfluid ^4He , so a very generic explanation is necessary to explain the ubiquity of these remanents. This explanation is provided by the Kibble-Zurek mechanism, which states that vorticity arises from discontinuities in phase caused by the move to a macroscopic wavefunction during the transition to superfluid [31].

2.1.4 Damping in Superfluid Helium 4

For oscillating structures in ^4He , the most general description of the damping is highly complicated, with multiple different components contributing to the overall force. Thankfully, many of these components of the drag are only relevant under particular conditions. As a simple example, the turbulent contribution to the drag can be safely ignored if the velocity is kept below the critical velocity of the object used. Another interesting contribution to the drag is caused by acoustic emission, which can become important for high frequency oscillators [32]. Sharp increases in drag have also been seen at specific frequencies, with this additional drag attributed to the excitation of acoustic resonances [33, 34].

Under the conditions used for our experiments only two components of the drag are relevant, allowing us to neglect all other contributions and consider a simplified picture of the damping. One of these is the intrinsic drag, which is entirely dependent on the properties of the oscillator and therefore remains constant regardless of the external conditions. The

drag is therefore dominated by the other component, caused by the interaction of the oscillator with the surrounding fluid and referred to as hydrodynamic damping. A solid theoretical understanding of the drag in this regime can therefore be obtained solely from study of this hydrodynamic drag [26].

To derive expressions for the hydrodynamic drag we start by treating the dissipative force as the sum of two components, a drag component proportional to velocity and a mass-enhancement term proportional to acceleration. The mass-enhancement contribution to the dissipation can be understood by introducing an effective mass, m^* , which becomes larger than the base mass of the object m due to the dissipative effects. The first enhancement to the effective mass, caused by the backflow of fluid around the structure, depends on the total density of the helium, ρ_{He} , and the volume of the object, V . If any normal fluid is present, the viscous clamping of this component to the device also contributes to the effective mass. This viscous drag depends on the normal fluid density ρ_{N} , the viscous penetration depth δ , and the surface area of the object S . The effective mass is then found by adding both mass enhancement terms to the mass of the oscillator:

$$m^* = m + \beta\rho_{\text{He}}V + B\rho_{\text{N}}\delta S, \quad (2.20)$$

where β and B are dimensionless factors of order unity, determined by the geometry of the oscillating object. This expression can be expanded by defining the viscous penetration depth in terms of dynamic viscosity η , normal fluid density and resonant frequency of the oscillator in helium f_{He} ,

$$\delta = \sqrt{\frac{\eta}{\pi\rho_{\text{N}}f_{\text{He}}}}, \quad (2.21)$$

$$m^* = m + \beta\rho_{\text{He}}V + B\rho_{\text{N}}S\sqrt{\frac{\eta}{\pi\rho_{\text{N}}f_{\text{He}}}}. \quad (2.22)$$

An expression for the frequency shift when immersed in helium can then be obtained by considering the product of resonant frequency squared and effective mass, which remains constant:

$$f_0^2 m = f_{\text{He}}^2 m^*, \quad (2.23)$$

where f_0 is the resonant frequency in vacuum at low temperature. By rearranging and applying equation 2.22, we then find:

$$\frac{f_0^2}{f_{\text{He}}^2} = 1 + \frac{\beta \rho_{\text{He}} V}{m} + \frac{B \rho_{\text{N}} S}{m} \sqrt{\frac{\eta}{\pi \rho_{\text{N}} f_{\text{He}}}} \quad (2.24)$$

For consistency, it makes sense to express all masses as densities. Converting the object mass into density:

$$\frac{f_0^2}{f_{\text{He}}^2} = 1 + \frac{\beta \rho_{\text{He}}}{\rho} + \frac{B \rho_{\text{N}} S}{\rho V} \sqrt{\frac{\eta}{\pi \rho_{\text{N}} f_{\text{He}}}}, \quad (2.25)$$

where ρ is the density of the oscillating object. Equation 2.25 now gives a usable theoretical values for the shift in resonance frequency as a result of the fluid dissipation. Since fluid density and dynamic viscosity are both known functions of temperature [35], this equation can be used to calculate the frequency shift at a given temperature so long as the values for the geometric coefficients are known from previous experiments.

To derive an expression for the change in resonance width, we must now consider the drag component of the overall dissipation. The resonance width in fluid, Δf_2 , can be described in terms of an intrinsic width, $\Delta f_{2,\text{int}}$, and an associated shift in the width:

$$\Delta f_2 = \Delta f_{2,\text{int}} \frac{m}{m^*} + \frac{b}{2\pi m^*}, \quad (2.26)$$

where b is the coefficient of the drag term. If the flow field around the object is potential, a solution for this coefficient can be found [26]:

$$b = CS\sqrt{\pi\rho_{\text{He}}\eta f_{\text{He}}}, \quad (2.27)$$

where C is a geometry dependent constant of order unity. Equation 2.27 can now be used to obtain the change in resonance width due to the fluid dissipation, labelled Δf ,

$$\Delta f = \frac{CS}{2m^*} \sqrt{\frac{\rho_{\text{He}}\eta f_{\text{He}}}{\pi}}. \quad (2.28)$$

By substituting equation 2.23, the effective mass can be replaced by the more experimentally accessible quantities of vacuum mass and frequency ratio,

$$\Delta f = \frac{CS}{2m} \sqrt{\frac{\rho_{\text{He}}\eta f_{\text{He}}}{\pi}} \left(\frac{f_{\text{He}}}{f_0}\right)^2. \quad (2.29)$$

Equation 2.29 can now be used, along with the known temperature dependence of the density and viscosity, to calculate the change in the resonance width due to hydrodynamic effects.

2.2 Helium 3

2.2.1 Liquid Helium 3

Before attempting to understand the superfluid phases of ^3He , it is worth first discussing the basic properties of the normal fluid phase. As the two-fluid model can also be applied to ^3He , understanding the behaviour of normal fluid can prove useful when interpreting results in which both components are present.

Since ^3He is a fermion, the simplest way to describe liquid ^3He is as a Fermi gas. An

understanding of Fermi gas behaviour must start with the distribution function, $f(E)$:

$$f(E) = \frac{1}{\exp\left(\frac{E-E_F}{k_B T}\right) + 1}. \quad (2.30)$$

At zero temperature this function is very simple, with all states filled below the Fermi energy, E_F , and all states above empty. At higher temperatures the transition becomes smeared out, with some states below the Fermi energy left empty and some above filled. The energy range this smearing is seen over is roughly equivalent to $k_B T$. An example of the distribution function at both zero and finite temperature is shown in figure 2.3.

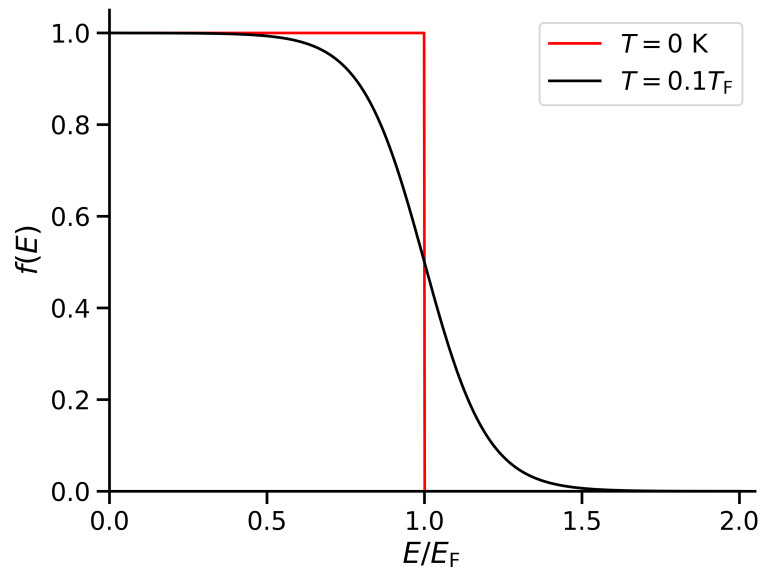


Figure 2.3: Fermi-Dirac distribution function, comparing behaviour at zero temperature with that at a finite temperature.

A value for the Fermi energy is therefore essential to understanding the properties of the Fermi gas, as it defines the boundary between filled and empty states. From statistical physics, we can obtain an expression for the Fermi momentum, p_F and then define the Fermi energy from this using the classical relation [36]:

$$p_F = \hbar \left(\frac{3\pi^2 N}{V} \right)^{\frac{1}{3}}, \quad (2.31)$$

$$E_F = \frac{p_F^2}{2m_3}, \quad (2.32)$$

$$E_F = \frac{\hbar^2}{2m_3} \left(\frac{3\pi^2 N}{V} \right)^{\frac{2}{3}}, \quad (2.33)$$

where N is the number of ${}^3\text{He}$ atoms present, V is the volume of the container considered and m_3 is the mass of each ${}^3\text{He}$ atom. The Fermi momentum can also be used to calculate the Fermi velocity by applying another familiar classical equation,

$$v_F = \frac{p_F}{m_3}. \quad (2.34)$$

However, this simple Fermi gas explanation is only valid if the particles considered do not interact with each other. This is obviously untrue for the case of liquid helium, as interactions between particles are an essential part of any liquid state. The adjustments required to successfully describe liquid ${}^3\text{He}$ were first described by Landau in a model referred to as a Fermi liquid [37–39].

The simplest major difference between a Fermi liquid and a Fermi gas is the introduction of quasiparticles. In Fermi liquid theory the atoms considered previously are replaced by quasiparticles with effective mass m_3^* . In ${}^3\text{He}$, this effective mass is always larger than the bare mass m_3 . In many ways this change leaves the structure of the theory unaltered, as equations 2.32, 2.33 and 2.34 still apply so long as the bare mass is replaced with the quasiparticle effective mass.

The second step in defining a Fermi liquid is the definition of an interaction between the particles. The interaction introduced can be quantified in terms of two infinite sets of

coefficients, F_1^s and F_1^a , referred to as Landau parameters. The superscripts s and a refer to spin-symmetric and spin-antisymmetric terms respectively. Each of these technically represents an infinite set of parameters, obtained by summing over the index l, though fortunately only a few of the low order terms are of experimental relevance. Perhaps the most important of these is the parameter F_1^s , which can be used to relate the effective mass to the bare particle mass,

$$\frac{m_3^*}{m_3} = 1 + \frac{F_1^s}{3}. \quad (2.35)$$

The other important Landau parameters are F_0^s , which is related to the sound velocity in the liquid, and F_0^a , which is related to the magnetic susceptibility. However, since these quantities are not important in the experiments discussed here, the full theoretical description will be neglected.

2.2.2 Superfluid Helium 3

Since helium 3 is a fermion the atoms must obey the Pauli exclusion principle, meaning the atoms cannot themselves undergo Bose-Einstein condensation. However, the existence of superconductivity proves that it is still possible for fermions to form a condensate under the correct conditions. To explain superfluidity in ^3He we will apply a variation on the theoretical framework used to describe superconductivity, known as BCS theory [40].

As applied to superconductivity, BCS theory solves the problem presented by the Pauli exclusion principle through the formation of Cooper pairs. At very low temperatures a weak, long-ranged attractive force, caused by phonon exchange due to lattice distortions, can bind two electrons to create Cooper pairs. The Cooper pairs have integer spin and it is the Bose-Einstein condensation of these pairs that causes the transition to superconductivity. The defining feature of the superconductor state as derived using BCS theory is the ap-

pearance of an energy gap, Δ , between the bound Cooper pair states and the free electron states. The value of this gap at zero temperature, $\Delta(0)$, can be calculated from the critical temperature of the superconductor, T_c ,

$$\Delta(0) = 1.76k_B T_c. \quad (2.36)$$

This gap represents the energy required to break a single electron out of its Cooper pair. The existence of this gap explains the stability of superconductivity at low temperatures, as only interactions with energy greater than the gap are able to break the Cooper pairs and disrupt the superconducting state.

In conventional superconductors the attraction mechanism that forms the pairs prioritises interactions between electrons of opposite spins, such that the Cooper pairs produced have spin $S = 0$. As electrons can be considered point particles, it is possible for them to occupy the same point and therefore the Cooper pair can form with no angular momentum, $L = 0$. This combination of zero spin and zero angular momentum is known as s-wave pairing.

Due to the large size of ^3He atoms in comparison to electrons, the $L = 0$ pairing used for electrons is not possible in helium. This means that ^3He Cooper pairs must have non-zero angular momentum and we must therefore consider p-wave pairing. Defined by the conditions $L = 1$ and $S = 1$, this is the simplest case we can still apply to ^3He . A state with total spin $S = 1$ can be described by three different spin configurations, corresponding to the three possible projections of this spin. These states are $|\uparrow\uparrow\rangle$, with spin projection $S_z = 1$, $\frac{1}{\sqrt{2}}(|\uparrow\downarrow\rangle + |\downarrow\uparrow\rangle)$, corresponding to $S_z = 0$, and $|\downarrow\downarrow\rangle$ for $S_z = -1$. A full understanding of the mathematics behind this p-wave pairing is very complicated [36, 41], and significantly beyond the scope of this work.

Interestingly, much of the theoretical framework used to describe superfluid ^3He was derived before the existence of the superfluid state in ^3He was confirmed experimentally. The first suggested solution for p-wave pairing considered a ground state consisting exclusively

of parallel spins and therefore containing only the states with $S_z = \pm 1$ [42], described as an equal spin pairing ground state. Working from this postulate produces intriguing results, as the condensate produced from this ground state can be shown to have an anisotropic gap. The anisotropy is spatial, depending on the angle θ between the momentum of the quasiparticles and the direction of angular momentum of the Cooper pair, conventionally set parallel to the z axis. For clarity, the gap parameter for this phase will be labelled Δ_A to distinguish it from the s-wave pairing result detailed above,

$$\Delta_A(0) = 2.02k_B T_c \sin(\theta). \quad (2.37)$$

Although subsequently shown not to be the most energetically favourable pairing mechanism in ^3He under the majority of conditions [43, 44] a superfluid phase based around an equal spin pairing ground state, referred to as the A phase, can be created [45]. In the absence of magnetic field the A phase only exists at high pressures and temperatures close to T_c , while applying a large magnetic field allows this phase to be stabilised down to much lower temperatures.

In an effort to find an approach with greater similarity to the s-wave theory, a ground state containing all three possible spin projections was also considered [43]. The gap parameter in this phase, labelled Δ_B , is isotropic and can be shown to have exactly the same form as for s-wave pairing,

$$\Delta_B(0) = 1.76k_B T_c. \quad (2.38)$$

A superfluid phase based on this pairing mechanism, called the B phase, can then be shown to be energetically preferable to the A phase under most conditions, making the B phase by far the most common superfluid phase in ^3He [43]. One important point that enables the close comparisons between the B phase and s-wave pairing is the value of the

total angular momentum, J . Each Cooper pair formed in the B phase is created such that the total angular momentum satisfies $J = L + S = 0$. This is achieved when the direction of the orbital and spin components are opposed and ensures the system is invariant under rotation, allowing the existence of an isotropic energy gap.

2.2.3 Turbulence in Superfluid Helium 3

Unsurprisingly, the complex nature of superfluid ^3He gives a much wider range of possible vortices than is observed in ^4He . However, most of these unusual vortices exist only in the more unusual phases. For example, continuous vortices with no vortex core have been observed in $^3\text{He-A}$ [46] and half-quantum vortices which only carry half of the expected quantum of circulation can be created in confined ^3He [47].

In $^3\text{He-B}$ two main types of vortex are possible, with the type of vortex present dependent on the temperature of the sample and the difference between the types defined by differences in the vortex core [48–50]. At high temperatures, the vorticity occurs around a single core made up of a different superfluid phase. In contrast the low temperature case has two distinct cores and essentially consists of two half-quantum vortices bound together into a single structure [51]. Regardless of these differences, both types of $^3\text{He-B}$ vortex carry a single circulation quantum and the same arguments made for vortices in ^4He apply to both. As the superfluid condensate in $^3\text{He-B}$ consists of Cooper pairs, the circulation quantum in $^3\text{He-B}$ is:

$$\kappa = \frac{h\hbar}{2m_3}, \quad (2.39)$$

where m_3 is the mass of a ^3He atom and so $2m_3$ is the mass of a Cooper pair.

As in ^4He , the size of the vortex core is approximately equal to the coherence length. In ^3He the coherence length varies between ≈ 70 nm at zero pressure and ≈ 10 nm at high

pressure. Vortex cores in ^3He are therefore much larger than in ^4He , where the typical vortex core size is ≈ 0.1 nm.

One other intriguing phenomenon, unique to superfluid helium ^3He , is caused by the exceptionally high viscosity of the normal fluid component. In fact, the viscosity is large enough that all of the normal fluid can be considered clamped to the walls of the container. This therefore creates a unique turbulence regime defined by a coupling between the superfluid and the container walls, uniform throughout the entire experimental volume, facilitated by the clamped normal fluid [52].

At very low temperatures, where the normal fluid density is negligible, quantum turbulence in ^3He becomes very similar to that observed in the zero temperature limit for ^4He . As in that case experiments show a form of quantum turbulence that appears closely analogous to classical turbulence despite the complete absence of a normal fluid component [53].

2.2.4 Excitations in Superfluid Helium 3

Due to the complex nature of superfluidity in ^3He , a wide variety of different excitations are possible within the condensate. In addition to some familiar excitations, such as acoustic phonons, superfluid ^3He allows for a range of other more exotic excitations. Many of these excitation modes are of great theoretical interest, with analogues to Higgs modes [54] and Majorana excitations [55] proving particularly noteworthy. As the theoretical background for some of these modes can be very complicated, none of these unusual excitations will be described here.

The thermal excitations however are of major importance to some of the experiments performed and will therefore be described in detail. All future uses of the term excitation therefore refers solely to these thermal excitations. In ^3He the thermal excitations are produced in pairs, as exciting a particle leaves behind an empty space in the otherwise filled states. These excitations are referred to as quasiparticles and quasiholes respectively.

All experimental ^3He results discussed in this thesis were performed far below the transition to superfluid, with all measurements taken below $0.3T_c$ in what is referred to as the ballistic regime. At these temperatures the low thermal excitation density increases the mean free path of the excitations to the point where this value vastly exceeds the size of the experimental cell. The probability of collisions between thermal excitations then becomes infinitesimally small and can therefore be neglected entirely.

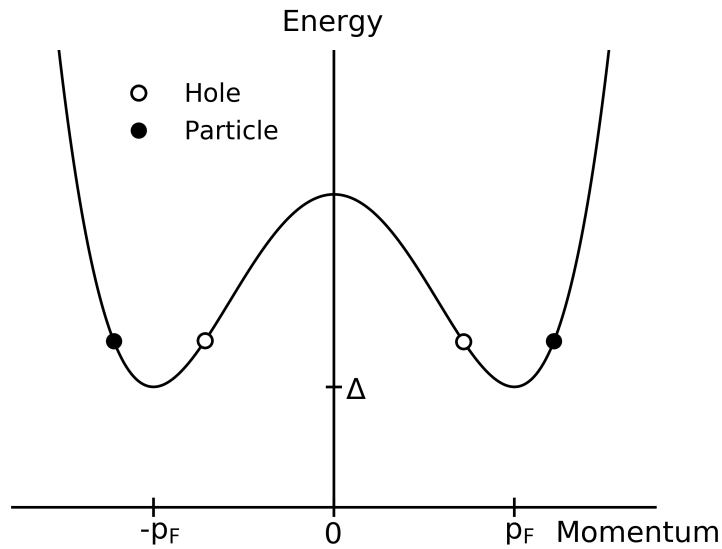


Figure 2.4: Dispersion curve for superfluid $^3\text{He-B}$, showing both particle and hole excitations.

One interesting interaction of quasiparticles in $^3\text{He-B}$, important even in the ballistic regime, is the possibility for perfect retroreflection through a process referred to as Andreev reflection. The theoretical explanation of this process can be obtained by considering the dispersion curve for $^3\text{He-B}$, shown in figure 2.4. Andreev reflection is made possible due to the minima in the dispersion curve around the Fermi momentum. At the Fermi momentum, a tiny change in momentum can push an excitation to the other side of the minima and therefore change the character of the excitation. Since quasiparticles have

velocity parallel to their momentum and quasiholes have velocity antiparallel to their momentum, this change in character reverses the direction of motion of the excitation with minimal change in the momentum magnitude.

From this dispersion curve, a value for the Landau velocity in $^3\text{He-B}$ can be obtained. As in ^4He , the Landau velocity is given by the gradient of the shallowest line that intersects the dispersion curve. In $^3\text{He-B}$, this gives:

$$v_L = \frac{\Delta}{p_F}. \quad (2.40)$$

Calculations using this equation at zero pressure give a value of $v_L = 27 \text{ mms}^{-1}$. Experiments using ions have verified this equation [56], though further experiments found the case is much more complicated when measuring with larger objects. The actual Landau velocity in these cases is found to be smaller than expected for oscillatory motion [57] and larger than expected in linear motion [58]. The theoretical reasons for the reduction in critical velocity during oscillations are now well understood [59,60], while the increase in critical velocity for linear motion remains a mystery.

2.2.5 Drag in Helium 3

In superfluid $^3\text{He-B}$, the drag caused by the motion of an object through the fluid can be split into three distinct components. The intrinsic component, determined exclusively by the properties of the structure, does not depend on external factors. At large velocities the response is dominated by the appearance of a temperature independent excess damping force. In $^3\text{He-B}$ the exact form of this excess damping is complicated, as vortex production and pair-breaking both become important at very similar velocities. The final component accounts for the temperature dependence of the damping, which can be understood by considering the interaction between thermal excitations and the object. Combining these three contributions gives an expression for the overall drag force:

$$F = F_0 + F_T + F_{\text{pb}}, \quad (2.41)$$

where F is the total drag, F_0 is the intrinsic component, F_T is the thermal drag and F_{pb} is the pair-breaking (excess damping) contribution.

To allow accurate interpretation of results obtained at non-zero temperatures in $^3\text{He-B}$, a detailed understanding of the thermal damping component is very important. To explain the mechanism behind this component we start by considering the heavily simplified case of a paddle of area A immersed in superfluid $^3\text{He-B}$. Firstly we apply a basic kinetic theory argument, representing the thermal excitations as a gas of particles, where N is the number of particles per unit volume. The paddle moves with velocity v while the particles have velocity v_g and momentum p_F . To keep things as simple as possible, only particles with velocity parallel to the object velocity are considered. Due to the relative velocity collisions are more likely with the front of the paddle and the applied force is:

$$F = 2Ap_F \left(\frac{N}{2}(v_g + v) - \frac{N}{2}(v_g - v) \right), \quad (2.42)$$

where the two terms on the right-hand side account for collisions with the front and rear of the paddle respectively. The resulting force is linear in v :

$$F = 2ANp_F v. \quad (2.43)$$

Experiments have shown that this is incorrect however, with the force measured in $^3\text{He-B}$ at very low temperatures proportional to v but more than 3 orders of magnitude larger [61]. In fact, the kinetic argument cannot possibly apply in ^3He as both particle and hole excitations are present. As holes have momentum antiparallel to their velocity, collisions with these excitations serve to reduce the drag force. With equal amounts of particles and

holes present we would therefore expect no net momentum transfer as the contributions of one type of excitations cancel those of the other.

To understand how the large drag force observed arises, we must consider the possibility of Andreev reflection. The easiest way to explain the process of Andreev reflection is to compare the dispersion curve in the stationary bulk fluid to that close to the object. This comparison is shown in figure 2.5, with the bulk fluid case on the left and the moving fluid on the right.

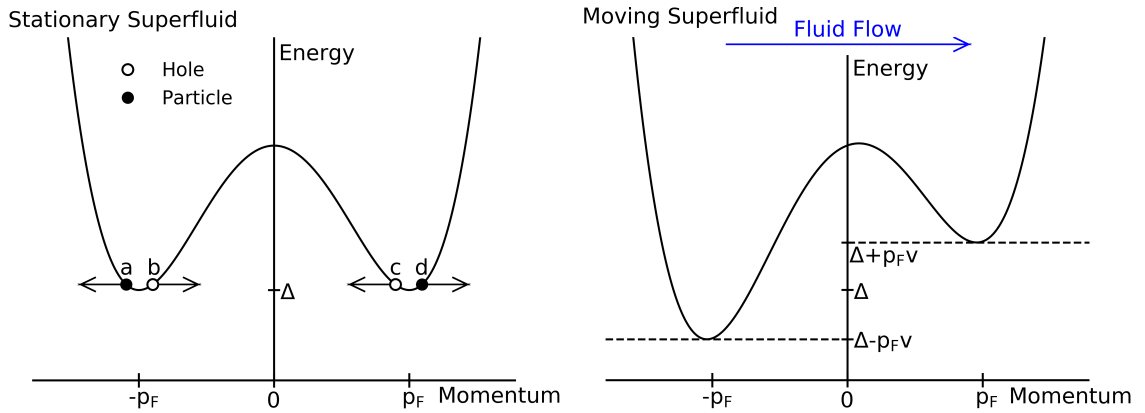


Figure 2.5: Dispersion curves for $^3\text{He-B}$ in stationary, bulk superfluid (left) and in the vicinity of the paddle (right). On the left-hand side the direction of motion for each excitation is represented by the attached arrow and the labels will be used for future reference. For a detailed description of the Andreev reflection process enabled by the shifted dispersion curve, see text.

As explained in section 2.2.4, Andreev reflection affects excitations near the minima of the dispersion curve, allowing small changes in momentum to change the character of the excitations and so reverse the direction of their motion. Andreev reflection effects become very important in the presence of moving superfluid, as the flow of the fluid shifts the dispersion curve. To return to our simple model, we assume the paddle has a positive velocity (defined here as left to right). As the fluid very close to the paddle must move with the object the superfluid velocity can be considered equivalent to that of the paddle.

The shifted dispersion curve in this region is shown on the right-hand side of figure 2.5.

As the superfluid velocity is positive, the shift in the dispersion curve due to the flow of the fluid raises the minimum allowed energy of excitations in the positive momentum branch (labelled c and d). Therefore only states with energy higher than this raised minima are allowed to propagate, with all excitations of lower energy undergoing Andreev reflection and reversing their direction of travel. This means excitations c and d are subject to Andreev reflection, reducing the number of holes incident on the front of the paddle and the number of particles colliding with the back. The negative momentum half of the dispersion curve undergoes a negative shift in the allowed energy, meaning the excitations in this branch (a and b) can propagate all the way to the paddle. In the ballistic regime only surface scattering is possible, meaning excitations a and b cannot scatter into the lower energy states produced by the shift of the dispersion curve and therefore still have the same energy as they did in the bulk fluid.

In front of the paddle, this means a larger proportion of the interactions are with particles. The momentum of the excitation is therefore opposite to that of the paddle and leads to a reduction in the paddle momentum. The reverse is true at the back of the paddle, with a greater number of interactions involving holes. However, as holes have momentum antiparallel to their velocity, these collisions also lead to a negative momentum transfer and apply a drag to the paddle. Through this mechanism, the screening of incoming excitations due to Andreev reflection leads to a significant increase in the damping experienced by the paddle.

One interesting consequence of this mechanism is that it places an unavoidable maxima on the drag possible. At high enough velocities a point must be reached where no excitations from the reflected branch are able to traverse the flow field. At this point, all collisions in front of the paddle will be with particles, and all behind the paddle with holes. Beyond this point additional increases in velocity cannot increase the drag any further and the

thermal drag must therefore become independent of velocity.

Provided the time taken for excitations to traverse the flow field is significantly smaller than the oscillation period, the same argument as above should apply to oscillatory motion as well. However, if the frequency of the oscillations becomes large this may no longer apply and we may have to consider the possibility of multiple Andreev reflections.

To quantify the thermal drag force due to these effects, we start by considering the force applied due to excitations with positive momentum. The force applied can be found from the change in momentum of the excitations during the collisions:

$$F_{1,2} = 2p_F \langle nv_g \rangle, \quad (2.44)$$

where $F_{1,2}$ is the force per unit area applied by the negative momentum branch excitations (a and b), p_F is the Fermi momentum and $\langle nv_g \rangle$ is the average excitation flux. The excitation flux is obtained from the number density of excitations, n , and the group velocity of these excitations, v_g . As collisions involving these excitations act to slow the paddle, we define the resulting drag force as positive. The number of collisions can be obtained by integrating the product of the group velocity of the excitations ($v_g(E)$) and the density of states for these excitations ($g(E)f(E)$):

$$\langle nv_g \rangle = \int_{\Delta}^{\infty} v_g(E) g(E) f(E) dE. \quad (2.45)$$

At velocities below those required for pair breaking all thermal excitations must originate in the bulk fluid, far from the oscillating structure. As the bulk dispersion curve applies to these thermal excitations, the minimum allowed energy for these states will be equal to the energy gap for superfluid $^3\text{He-B}$. For excitations in branches 1 and 2 close to the paddle, the dispersion curve contains energy states below Δ . However, in the ballistic regime the excitations do not scatter and so the minimum energy of the incoming excitations is still

equal to the energy gap. Therefore, to cover all available energy states, the integration must be performed from the gap energy to infinity.

In the ballistic regime, the distribution function can be simplified to a Boltzmann distribution:

$$f(E) = \exp\left(-\frac{E}{k_{\text{B}}T}\right). \quad (2.46)$$

A further simplification can be obtained by considering the density of states. As the number of momentum states must be equal to the number of energy states, we can equate these:

$$g(E)dE = g(p)dp. \quad (2.47)$$

The definition of group velocity, $v_{\text{g}} = \frac{dE}{dp}$, can now be used to rearrange equation 2.47:

$$g(E)dE = \frac{g(p)}{v_{\text{g}}}dE, \quad (2.48)$$

$$g(E)v_{\text{g}}dE = g(p)dE, \quad (2.49)$$

$$g(p) = v_{\text{g}}(E)g(E). \quad (2.50)$$

Since all states considered are close to the Fermi surface, the assumption $g(p) \approx g(p_{\text{F}})$ can be used to simplify things further:

$$g(p_{\text{F}}) = v_{\text{g}}(E)g(E). \quad (2.51)$$

By applying these simplifications, the integral can now be solved:

$$\langle nv_g \rangle = g(p_F) \int_{\Delta}^{\infty} \exp\left(-\frac{E}{k_B T}\right) dE, \quad (2.52)$$

$$\langle nv_g \rangle = g(p_F) \left[-k_B T \exp\left(-\frac{E}{k_B T}\right) \right]_{\Delta}^{\infty}, \quad (2.53)$$

$$\langle nv_g \rangle = g(p_F) k_B T \exp\left(-\frac{\Delta}{k_B T}\right). \quad (2.54)$$

The same procedure can now be applied for the positive momentum branches of the dispersion curve. In this region, the flow shifts the dispersion curve towards higher energies. Excitations with energy below the minimum of the shifted dispersion curve will undergo Andreev reflection and so be unable to participate in the interactions at the surface. The lower limit of the integral must therefore be adjusted to account for this,

$$F_{3,4} = -2p_F \int_{\Delta+p_F v}^{\infty} v_g(E) g(E) f(E) dE, \quad (2.55)$$

where $F_{3,4}$ is the force per unit area applied by excitations in the positive momentum branches. In the convention used here, this force must be negative as interactions with these excitations would reduce the drag experienced by the object. The same simplifications used previously can be applied here as well:

$$F_{3,4} = -2p_F g(p_F) \int_{\Delta+p_F v}^{\infty} \exp\left(-\frac{E}{k_B T}\right) dE, \quad (2.56)$$

$$F_{3,4} = -2p_F g(p_F) k_B T \exp\left(-\frac{\Delta}{k_B T}\right) \exp\left(-\frac{p_F v}{k_B T}\right). \quad (2.57)$$

Using the expression previously obtained for $\langle nv_g \rangle$, this can be simplified further:

$$F_{3,4} = -2p_F \langle nv_g \rangle \exp\left(-\frac{p_F v}{k_B T}\right). \quad (2.58)$$

The expressions for $F_{1,2}$ and $F_{3,4}$ can now be combined to find the total drag force per unit area due to interactions with the thermal excitations, F_A :

$$F_A = F_{1,2} + F_{3,4}, \quad (2.59)$$

$$F_A = 2p_F \langle nv_g \rangle \left(1 - \exp\left(-\frac{p_F v}{k_B T}\right)\right). \quad (2.60)$$

To move from the simplified view described here to a full three-dimensional picture we introduce two corrections, represented by two geometric coefficients, γ and λ , both of order 1. The coefficient λ modifies the velocity to account for non-linear variations while γ adds a pre-factor to the whole equation to adjust the overall magnitude of the force [62]. For example, in the case of a circular wire with length L and diameter d , the corrected expression is:

$$F_T = \frac{2p_F d \gamma \langle nv_g \rangle}{\lambda} \left(1 - \exp\left(-\frac{\lambda p_F v}{k_B T}\right)\right), \quad (2.61)$$

where F_T is the total force per unit length L . In general terms d is then the dimension of the oscillator perpendicular to the flow, introduced when converting to force per unit length and equivalent to the diameter for this specific case.

As derived earlier, the component of the drag force due to thermal excitations can be predicted using equation 2.61. Unsurprisingly, this force is heavily temperature dependent due to the increased density of thermal excitations at higher temperatures. To enable

comparisons between measurements of the drag taken across a range of temperatures, equation 2.61 must first be normalised.

To remove the dependence on excitation density, we first need to obtain an expression for the thermal drag force in the low velocity limit, $F_{v \rightarrow 0}^T$. In this limit we know that the energy associated with the flow is much smaller than the thermal energy, $p_F v \ll k_B T$, and so we can simplify equation 2.61 by considering the Taylor expansion of the exponential. In this limit the exponent is much smaller than 1 and we can therefore neglect all higher powers of the expansion:

$$\exp\left(-\frac{\lambda p_F v}{k_B T}\right) \approx 1 - \frac{\lambda p_F v}{k_B T}. \quad (2.62)$$

Using this approximation in equation 2.61 then gives:

$$F_{v \rightarrow 0}^T = \frac{2p_F^2 d\gamma \langle n v_g \rangle}{k_B T} v. \quad (2.63)$$

To demonstrate how much larger the drag becomes when excitation screening due to Andreev reflection is considered, we can compare equations 2.43 and 2.63. The ratio of the two forces is then given by $\frac{p_F \langle v_g \rangle}{k_B T}$. At a temperature of 150 μK , the force due to Andreev reflection is therefore approximately 7.2×10^3 times larger than would be expected from the kinetic model of drag. This is consistent with experimental measurements [61].

To enable normalisation, the velocity dependence can be removed from equation 2.63 by taking the derivative:

$$\left(\frac{dF^T}{dv}\right)_{v \rightarrow 0} = \frac{2p_F^2 d\gamma \langle n v_g \rangle}{k_B T}. \quad (2.64)$$

Dividing the thermal force by this derivative now gives a normalised thermal force, F_n^T :

$$F_n^T = \frac{F_T}{\left(\frac{dF^T}{dv}\right)_{v \rightarrow 0}}, \quad (2.65)$$

$$F_n^T = \frac{k_B T}{\lambda p_F} \left(1 - \exp\left(-\frac{\lambda p_F v}{k_B T}\right)\right). \quad (2.66)$$

From equation 2.66, we can see that this normalisation process has successfully removed the dependence on the excitation density. This expression is however still temperature dependent, so further normalisation is required. To remove the remaining temperature dependence we introduce the reduced velocity, v^* ,

$$v^* = \frac{p_F v}{k_B T}. \quad (2.67)$$

By repeating the derivation detailed above in terms of v^* , an expression for force can be obtained with no temperature dependence at all. We refer to this as the reduced thermal force, F_r^T :

$$F_r^T = \frac{(1 - \exp(-\lambda v^*))}{\lambda}. \quad (2.68)$$

Therefore, applying equation 2.68 should allow data taken at a wide variety of different temperatures to be collapsed onto a single dependence.

3 Experimental Methods

3.1 Oscillating Devices

Oscillating structures have long been a cornerstone of low temperature research, as their ability to accurately probe the properties of the surrounding fluid leads to a wide range

of potential uses. In the absence of any fluid flow these properties can be used to deduce the temperature of the fluid, as for sufficiently low velocities thermal effects dominate the damping experienced by the wire. If the oscillator is driven hard enough, the motion can be used to generate turbulence in the fluid. Depending on the arrangement of the devices, changes in the drag can also be used to detect turbulence generated elsewhere in the experimental volume.

Until recently, perhaps the most common type of immersed oscillator used in superfluid experiments was the vibrating wire resonator. Typically these resonators are made from a single loop of superconducting wire and driven to oscillate using the Lorentz force generated when an alternating current is applied in the presence of an external magnetic field.

For many applications, the traditional wire resonators have now been replaced by quartz tuning forks due to a few major advantages the forks provide [26]. In contrast to the wires, which must be created manually, suitable tuning forks are readily available commercially. Due to the piezoelectric driving scheme used the forks can also operate in zero magnetic field, which can be a major advantage in experiments involving a magnetically active medium such as superfluid ^3He . This is also beneficial in nuclear demagnetisation cryostats as the removal of a necessary field for device operation allows demagnetisation to a lower final field and hence a smaller base temperature.

Due to rapid advancements in the field of nanofabrication, nanoelectromechanical systems (NEMS) are becoming increasingly viable as alternatives. The major advantage these devices promise over traditional approaches is improved measurement sensitivity. While not yet tested in quantum fluids experiments, other applications of nanoscale oscillators have shown truly exceptional sensitivity to changes in oscillator effective mass [63–65]. In most cases this is used to enable sensitive measurements of the mass of an object attached to the beam. In our applications, the effective mass depends on the properties

of the surrounding fluid and NEMS should therefore enable more precise determination of these properties. The tiny size also presents a related drawback however as these devices are generally fragile, meaning care must be taken to avoid damaging the sensor. This is particularly problematic for measurements at ultra low temperatures as such experiments are frequently slow to prepare.

3.1.1 Oscillator Theory

Despite the significant differences between the various types of resonator available, the response of all kinds of device can be understood in terms of conventional oscillator theory. Following this approach, the resonators can be treated as a mass on a spring:

$$\omega_0 = \sqrt{\frac{k}{m}}, \quad (3.1)$$

where ω_0 is the natural resonant frequency of the system, k is the spring constant and m is the mass.

For experimental purposes the oscillators will always be driven, using some external force $F = F_0 e^{i\omega t}$, where F_0 is the amplitude of the force and t is the time. Though the nature of this force depends on the type of oscillator considered, the general form remains the same. In the presence of this driving force, the overall equation of motion for the oscillator becomes:

$$m\ddot{x} = F_0 e^{i\omega t} - kx - m\lambda\dot{x}, \quad (3.2)$$

$$F_0 e^{i\omega t} = m\ddot{x} + m\lambda\dot{x} + kx, \quad (3.3)$$

where x , \dot{x} and \ddot{x} are the position, velocity and acceleration of the oscillator respectively.

The term $-kx$ is therefore the restoring force and the term $-m\lambda\dot{x}$ describes the damping in terms of a damping coefficient λ . This damping coefficient is a complex variable and so is best considered in terms of a real and imaginary component:

$$\lambda = \lambda_2 + i\lambda_1. \quad (3.4)$$

Describing the damping requires a complex coefficient due to the nature of the drag force as a combination of two distinct components. Physically, λ_1 describes the non-dissipative drag component caused by the back-flow of fluid around the oscillator. The other coefficient λ_2 relates to the dissipative drag. For completeness, it must be noted that the back-flow will also increase the effective mass of the oscillator. However, since the fluid mass is typically much smaller than that of the oscillator, this effect contribution will be neglected for this discussion. Assuming the damping is much smaller than the other contributions to the force, equation 3.3 can be solved for position using a time dependent exponential,

$$x(t) = x e^{i\omega t}. \quad (3.5)$$

Differentiating this solution then gives the equations for velocity and acceleration:

$$\dot{x}(t) = i\omega x(t), \quad (3.6)$$

$$\ddot{x}(t) = -\omega^2 x(t). \quad (3.7)$$

Using these, we can now restate equation 3.3 entirely in terms of velocity and then rearrange this to get an expression for the velocity in terms of force and the resonance parameters:

$$F = i\omega m\dot{x} + m\lambda\dot{x} + \frac{m\omega_0^2\dot{x}}{i\omega}, \quad (3.8)$$

$$\dot{x} = \frac{F\omega}{m} \frac{1}{\omega\lambda_2 + i(\omega^2 + \omega\lambda_1 - \omega_0^2)}. \quad (3.9)$$

To allow us to separate this equation into real and imaginary components, the imaginary term must be removed from the denominator,

$$\dot{x} = \frac{F}{m} \frac{\omega^2\lambda_2 + i\omega(\omega_0^2 - \omega^2 - \omega\lambda_1)}{\omega^2\lambda_2^2 + (\omega_0^2 - \omega^2 - \omega\lambda_1)^2}. \quad (3.10)$$

This can now be broken down into the following two terms:

$$\text{Re}(\dot{x}) = \frac{F}{m} \frac{\omega^2\lambda_2}{\omega^2\lambda_2^2 + (\omega_0^2 - \omega^2 - \omega\lambda_1)^2}, \quad (3.11)$$

$$\text{Im}(\dot{x}) = \frac{F}{m} \frac{\omega(\omega_0^2 - \omega^2 - \omega\lambda_1)}{\omega^2\lambda_2^2 + (\omega_0^2 - \omega^2 - \omega\lambda_1)^2}. \quad (3.12)$$

Splitting the velocity in this way is worthwhile as these components have well defined physical meanings. The real part describes the component of the velocity in-phase with the driving force while the imaginary part corresponds to the component out-of-phase with the driving force, often referred to as the quadrature. Both of these are easily accessible experimentally for the oscillators discussed here.

By considering the expression for the real component we can estimate the maximum possible velocity, which will occur when the denominator is minimised. As the powers of two ensure the terms in the denominator can never become negative this occurs when the second term in the denominator is equal to zero, meaning the relevant condition is:

$$\omega_0^2 - \omega_1^2 - \omega_1 \lambda_1 = 0, \quad (3.13)$$

where ω_1 is the frequency at which the maximum velocity occurs. We can then use this condition to calculate the velocity the oscillator will have at this frequency:

$$\text{Re}(\dot{x})_{\text{max}} = \frac{F \omega_1^2 \lambda_2}{m \omega_1^2 \lambda_2^2} = \frac{F}{m \lambda_2}. \quad (3.14)$$

Equation 3.14 can now be used to derive an expression for the width of the oscillator, labelled $\Delta\omega_2$. For all future discussion, we use width to refer to the full width of the peak as measured at half of the maximum height. We can therefore combine the expression for the maximum velocity and the general expression for in-phase velocity to calculate the frequency at which the height has dropped to half its maximum value (labelled ω_2):

$$\frac{F}{2m\lambda_2} = \frac{F}{m} \frac{\omega_2^2 \lambda_2}{\omega_2^2 \lambda_2^2 + (\omega_0^2 - \omega_2^2 - \omega_2 \lambda_1)^2}. \quad (3.15)$$

By rearranging this, an expression for ω_2 can be obtained:

$$(\omega_0^2 - \omega_2^2 - \omega_2 \lambda_1)^2 = \omega_2^2 \lambda_2^2. \quad (3.16)$$

By assuming that the difference between the frequencies is much smaller than the frequencies themselves, the solutions to this can be found:

$$\omega_0 \pm \omega_2 = \frac{\lambda_1 \pm \lambda_2}{2}, \quad (3.17)$$

where the dual solutions account for the fact that half-maxima exist both above and below the peak and appear in the calculation when the square root is taken. The resonance width $\Delta\omega_2$ can then be calculated as the difference between the two solutions for ω_2 :

$$\Delta\omega_2 = \lambda_2. \quad (3.18)$$

This can then be converted to the measurable frequency width, Δf_2 :

$$\Delta f_2 = \frac{\Delta\omega_2}{2\pi} = \frac{\lambda_2}{2\pi}. \quad (3.19)$$

This expression is not particularly useful in our experiment as the drag coefficient λ_2 is never explicitly measured or calculated. By rearranging equation 3.14 and combining the result with 3.19, the drag coefficient can be replaced with more experimentally accessible quantities:

$$\Delta f_2 = \frac{F}{2\pi m \dot{x}_{\max}}. \quad (3.20)$$

Rearranging this then gives a very useful experimental quantity we refer to as the height-width-drive,

$$\frac{\dot{x}_{\max} \Delta f_2}{F} = \frac{1}{2\pi m}. \quad (3.21)$$

Although small variations in the effective mass of the oscillator do occur, these are largely negligible and so equation 3.21 can be considered constant and the height-width-drive proves very useful in certain measurements and calibrations.

Another important parameter of a resonance worth quantifying here is the quality factor, Q . This essentially describes the efficiency of the resonance and is defined in terms of the energy stored E_s and the energy lost per cycle E_l :

$$Q = \frac{2\pi E_s}{E_l}. \quad (3.22)$$

Quality factor is therefore maximised when the energy lost per cycle is small, meaning highly efficient oscillators will be described by large quality factors. Alternatively, the quality factor can also be defined in terms of the resonant frequency f_0 and resonant width:

$$Q = \frac{f_0}{\Delta f_2}. \quad (3.23)$$

This expression shows that resonances with a high quality factor are also defined by a narrow width. Additionally the quality factor is roughly equal to the number of cycles required for the oscillator to ring down, and is therefore very useful in ensuring a sufficient amount of time is given for a resonator to return to equilibrium between measurements.

3.1.2 Current Driven Oscillators

Despite the obvious differences, the traditional wire resonators and the NEMS considered here have very similar modes of operation. In both cases, oscillations are induced by applying an alternating current, $I = I_0 e^{i\omega t}$, in the presence of an external magnetic field, B . This then applies a Lorentz force to the object. Although both traditional vibrating wire resonators and the NEMS beams tested operate using the same physical mechanism, a detailed understanding of this process is only necessary for the conventional oscillators. A different measurement scheme is used for the NEMS that does not require accurate knowledge of the voltage generated. The method applied for the NEMS is described in section 3.2.4. As the drive signal is provided in the form of a current, these devices are referred to as current driven oscillators. The driving force produced is given by:

$$F = BlI_0 e^{i\omega t}, \quad (3.24)$$

where l is the spatial dimension of the oscillator perpendicular to the force. The periodic

nature of the current will therefore produce a periodic force, which causes the wire to oscillate. The oscillations produced lead to motion of the conductor perpendicular to the magnetic field, and therefore a voltage will be generated according to Faraday's law:

$$V = -\frac{d(\mathbf{B} \cdot \mathbf{A})}{dt}, \quad (3.25)$$

where V is the voltage generated, \mathbf{B} and \mathbf{A} are the field and area vectors respectively. In our experiments the field is kept constant during measurements, so has no time dependence. The magnitude of the area also does not change, so the time dependence required is introduced as a change in the angle between the area and the field.

To calculate the voltage, we must first obtain an expression for the area parallel to the field, labelled $A(t)$ to make the time dependence explicit. For the case of the semi-circular wire resonators we start by assuming that the area parallel to the field is given by the product of the area of the semicircle $\frac{\pi D^2}{8}$ and the angle between this area and the field, labelled ϕ . An expression for this angle in terms of the oscillation amplitude x and the leg spacing D can be found by applying trigonometry:

$$\tan(\phi) = \frac{2x}{D}. \quad (3.26)$$

Assuming the amplitude is always significantly smaller than the leg spacing we can apply the small angle approximation $\tan(\phi) \approx \phi$ to simplify this, giving $\phi = \frac{2x}{D}$. We can use this to calculate the area parallel to the field,

$$A(t) = \frac{\pi D x}{4}. \quad (3.27)$$

The voltage generated can now be calculated by combining equations 3.25 and 3.27:

$$V = -B \frac{dA(t)}{dt}, \quad (3.28)$$

$$V = -\frac{\pi B D v}{4}. \quad (3.29)$$

The factor of $\frac{\pi}{4}$ in this expression is essentially a geometric factor to account for the semi-circular shape of the wire used. In reality this result will only ever be an approximation as the derivation assumes that the wires are a perfect semicircle, a fact which definitely will not be true in practice. Fortunately this difference in shape will not cause too much change in the geometric factor, so for simplicity's sake the variations will be neglected.

3.1.3 Vibrating Wire Resonators

Vibrating wire resonators have a relatively long history in fluid research at low temperatures, a fact which can easily be understood by considering some of the strengths of these devices. As reasonably simple, highly sensitive ways of directly probing the properties of the experimental fluid, these resonators were for a long time one of the best options when deciding on a probe for low temperature fluid measurements. Although largely replaced by quartz tuning forks in many modern experiments, some measurements are still ideally suited to the traditional wire resonator.

All wire resonators used in these experiments were custom-made, starting with a commercial niobium-titanium superconducting wire consisting of many filaments of niobium-titanium surrounded by copper cladding. To make the resonator, the filaments of niobium-titanium are first exposed by using acid to remove the cladding. All but one of the many filaments are then painstakingly removed by hand, leaving a single thin niobium-titanium wire to serve as the resonator.

All of the vibrating wires used here are in the shape of a semicircular loop, with the legs

fixed into a sheet of stycast hardened paper. The resonators can be created in many different diameters by starting with niobium-titanium wires of different filament diameter. Three different diameters are used here, with $13.5\ \mu\text{m}$, $4.5\ \mu\text{m}$ and $0.9\ \mu\text{m}$ diameter wires all included in the ^3He cell used.

Due to the exceptional sensitivity provided by its small size, the $0.9\ \mu\text{m}$ diameter wire is used as the main thermometer for most measurements performed here. The other wires are used for a wide range of purposes such as additional thermometry, vorticity creation and heating (quasiparticle production).

Typically, the oscillation frequency of the wires used ranges from 100 Hz to 1 kHz. There is no correlation between filament size and frequency, with wires of all diameters found to have frequencies throughout the whole range.

3.1.4 Nanobeams

In recent years the field of nanoelectronics has advanced rapidly, with nanoscale devices shown to exhibit truly exceptional mass sensitivity in a range of different applications [63–65]. As probes in helium work by detecting the change in effective mass due to clamped fluid, these increases in sensitivity could prove highly beneficial to superfluid research if they can be replicated in this system. The application of these structures to low temperature helium research is still relatively new however, so much further development is necessary before nanoscale structures match the ubiquity of wire resonators or tuning forks.

In our experiments, the nanoscale structures used were doubly-clamped beams. Our devices consist of a thin, linear beam of aluminium, with an approximately 100 nm by 100 nm square cross-section. A wide range of different beam lengths can be created, with values ranging from $15\ \mu\text{m}$ to $100\ \mu\text{m}$. This approach produces beams with an oscillation frequency on the order of MHz. The suspended beams are fixed at both ends to a larger

area of aluminium and suspended above a silicon substrate, and so should technically be referred to as doubly-clamped beams.

In manufacturing terms, the nanobeams are made in a clean room using a range of well established nanofabrication techniques. The structure of the beam is built by depositing aluminium onto a silicon wafer, using electron-beam lithography to define the desired shape. The silicon is then etched away, leaving the aluminium beam suspended. An SEM image of a sample beam is shown in figure 3.1.

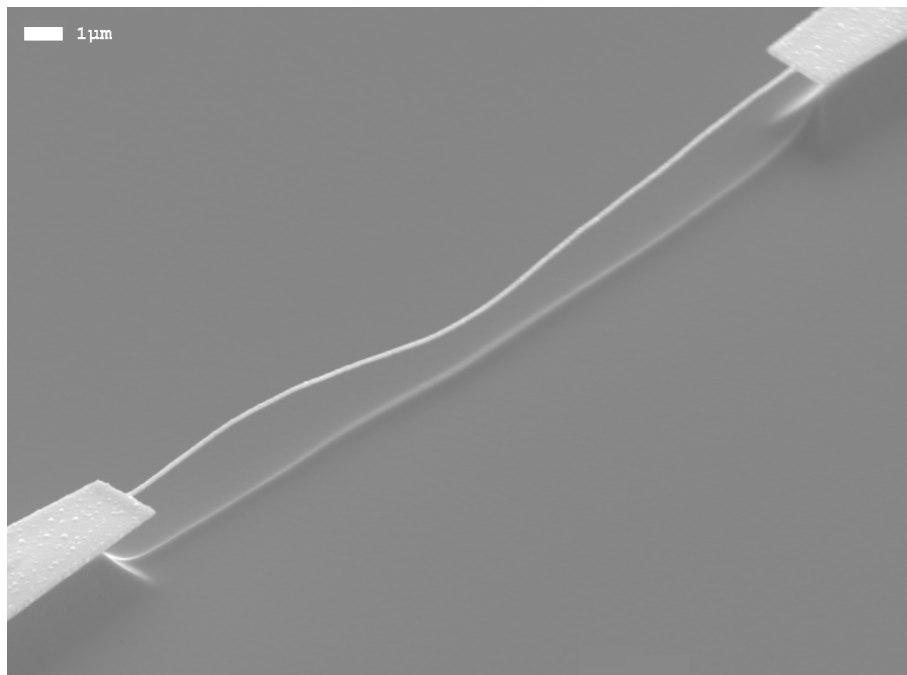


Figure 3.1: SEM image of a sample doubly-clamped beam, taken at room temperature.

An obvious concern visible in figure 3.1 is the shape of the beam, which is clearly not straight, indicating a lack of tension in the beam. This is due to the temperature, as the beams are designed to work at cryogenic temperatures while images are all taken at room temperature. Due to differences in the thermal contraction coefficient between the aluminium beam and the silicon substrate, the beam is pulled into tension as it is cooled. There is also the possibility that measurements in fluid will be compromised by effects

due to the proximity of the substrate surface. In ^4He this will not be a problem, as the height of the beam above the substrate ($2\ \mu\text{m}$) is significantly larger than the viscous penetration depth throughout the whole superfluid regime. For frequencies of the order MHz, the penetration depth in ^4He reaches a maximum value of about $0.5\ \mu\text{m}$ before the transition to a purely superfluid regime renders this quantity irrelevant. Unfortunately this does not hold for ^3He however, as the larger viscous penetration depth in ^3He means the beam is likely to exist in a region where a portion of the normal fluid is clamped. The devices used may therefore need to be redesigned to remove this drawback before they can be applied to measurements in ^3He at temperatures with a finite normal fluid fraction.

3.1.5 Tuning Forks

The use of quartz tuning forks as probes in superfluid helium began with the application of commercially available tuning forks [26]. Although these commercial forks are still suitable for many applications, the specialised nature of our measurements mean that the forks used in these experiments are all custom made. The design used remains very similar, with the forks consisting of two parallel quartz prongs, referred to as tines. Motion is induced through the piezoelectric effect, with the voltage applied by contacts on the surface of the tines. In the fundamental oscillatory mode, the tines of the fork move in anti-phase.

The primary reason to use custom produced forks is the wide variety of different dimensions available. Common to all forks used was the tine thickness, $T = 90\ \mu\text{m}$. Two possible values of width were used, $W = 25\ \mu\text{m}$ and $W = 50\ \mu\text{m}$. The tine length L was different for every fork, as this parameter determines the resonant frequency.

In terms of quantum fluids research it was initially hoped that the standardised production of commercial tuning forks would mean that all similar forks behaved the same and so remove the need for individual calibrations. Unfortunately this was quickly proved incorrect, with no common dependence possible [26]. Quartz tuning forks do however still

have a variety of advantages when compared to other probes.

One major benefit is availability, as suitable forks can be purchased from commercial sources. However, if custom made tuning forks are used instead, variation of the fork dimensions allows access to a wide range of oscillation frequencies. For example, the forks used in the quasiparticle camera included have frequencies ranging from 20 kHz to 100 kHz. If higher frequencies are needed most forks also have a readily available overtone mode at frequencies approximately 6.3 times that of the fundamental. Though the pattern of electrodes used to drive the forks should strictly be redesigned to optimise performance of these overtone modes, previous results have shown successful measurements of overtones without any such adjustments [32].

When compared to conventional wire resonators, perhaps the most significant advantage of quartz tuning forks is that they can be operated in the absence of any magnetic field. This is possible as a result of the different operation scheme used for tuning forks, which we refer to as voltage driven oscillators. As the name implies, applying an AC voltage $V = V_0 e^{i\omega t}$ to the electrodes induces oscillations. The resulting motion of the fork then creates a current through the piezoelectric effect, with the current produced proportional to the velocity of the oscillations:

$$I = av, \tag{3.30}$$

where a , referred to as the fork constant, depends on the properties of quartz and the dimensions of the tuning fork. A theoretical value of the fork constant, a_T is given by [26]:

$$a_T = 3d_{11}E_q \frac{TW}{L}, \tag{3.31}$$

where d_{11} and E_q are the piezoelectric modulus and Young's modulus of quartz respectively. To complete the mechanical picture of the oscillations produced, an expression for

the force can be obtained by considering equation 3.30 and equating the electrical and mechanical power during oscillations:

$$F = \frac{aV}{2}, \quad (3.32)$$

where the factor of 2 accounts for the fact that both fork tines are in motion.

Experimentally, the fork constant can be inferred from measurements of the resonance. By substituting the tuning fork velocity (equation 3.30) and force (equation 3.32) into equation 3.21, an expression for the fork constant in terms of measurable parameters can be obtained:

$$a = \sqrt{\frac{4\pi m_{\text{eff}} I \Delta f_2}{V}}, \quad (3.33)$$

where the effective mass m_{eff} is approximately a quarter of the base mass of a single tine [32]. Reliable values of the fork constant are very important, as it is this constant that we use to extract the physically relevant quantities of force and velocity from the measured values of voltage and current. Typically, the experimental fork constant is found to be approximately 30% of the theoretical prediction [26]. Previous experiments have shown that optically measured values of fork velocity are consistent with the values estimated from the experimental fork constant to within about 10% [66]. We are therefore confident that this method of estimating the fork constant is trustworthy.

3.2 Measurement Techniques

Due to the wide variety of different devices tested during our experiments, an equally large selection of approaches to measurement were required. For clarity the techniques used will be discussed in detail here. With the exception of two of the experiments described, which were performed using unique methods and will be described individually, the same scheme

is used for all other measurements. For both tuning forks and vibrating wire resonators, the drive is provided by a signal generator and the response is detected using a lock-in amplifier. As wire resonators respond to current and tuning forks respond to voltage, the exact setup used is different for the two different types of device.

For vibrating wires, a variable resistance drive box is placed between the generator and the device itself. This drive box converts the voltage supplied by the generator into a current, with the value of the variable resistor used to set the conversion ratio. A transformer within the drive box separates the device side of the circuit from the generator. This allows us to more accurately determine the resistance of the device side and hence the voltage to current conversion ratio. If further signal reduction is required, 20 dB of attenuation is added before the drive box. To make detection easier, the returning signal from the vibrating wires is typically increased using a low temperature transformer.

As tuning forks are voltage driven oscillators, a different measurement scheme is needed for these devices. To avoid the possibility of damaging the fork with excessive drive force, the amplitude of the voltage produced by the signal generator is reduced by adding either 60 or 80 dB of attenuation to the generator output. On the measurement side of the circuit, a custom current-voltage converter [67] is included to convert the response current into a voltage measurable by the lock-in amplifier.

3.2.1 Frequency Sweep

The simplest of the main measurement techniques used in these experiments, a frequency sweep (often referred to as an f-sweep) is a way of characterising a resonance regularly applied to both vibrating wire resonators and tuning forks. In an f-sweep, a fixed drive is applied to the oscillator and both the in phase and out of phase responses are recorded as the frequency is varied in steps. The properties of the resonance are then calculated by fitting a Lorentzian lineshape to the in phase (V_x) and out of phase (V_y) components. If

using a vibrating wire resonator, equations 3.24 and 3.29 can then be applied to calculate the force and velocity associated with the resonance. For tuning forks, equations 3.30 and 3.32 must be used instead. An example of the results obtained from an f-sweep is shown in figure 3.2.

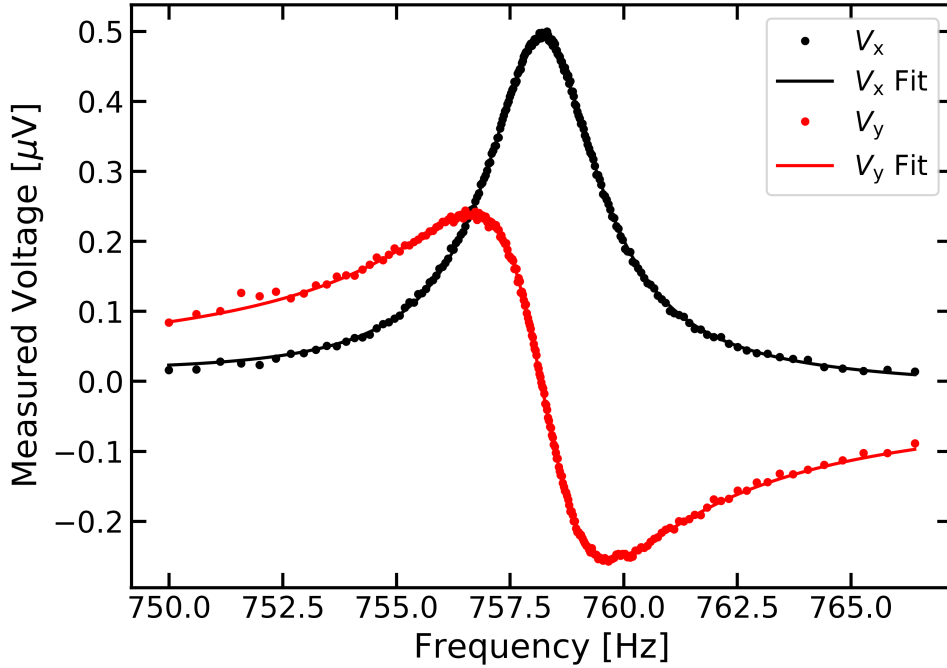


Figure 3.2: Example f-sweep results, taken for a $0.9 \mu\text{m}$ diameter wire resonator in superfluid $^3\text{He-B}$ at $140 \mu\text{K}$. Fits to a Lorentzian lineshape are performed to each components. When performing analysis, values for the amplitude, center frequency and width of the resonance are typically taken from the V_x fit. The V_y fit is mostly used as a diagnostic to ensure the two fits return similar values.

F-sweeps are useful as the most accurate method for determining the resonant properties of the device, with the resonant width often the most important of these due to its connection to damping and so therefore temperature. At the start of each demagnetisation of the fridge frequency sweeps are performed on all resonators to verify the resonant frequency and width, as well as ensuring the phase setting of the lock-in amplifier used correctly

matches that of the resonator.

Due to the inevitability of some background heat leak, the temperature of the experimental cell rises steadily over time. As the most accurate method of determining resonance width f-sweeps are often performed regularly throughout the experiment to quantify these temperature changes. When no measurement is being performed, common practice is to leave f-sweeps running on all oscillators. A feedback loop within the program used adjusts the input parameters based on the most recent output, ensuring the resonance is not lost as the frequency shifts.

3.2.2 Resonance Tracking

Although very accurate, the slow speed of each f-sweep means they are not ideal for thermometry in situations where the temperature changes rapidly. For more responsive thermometry we use resonance tracking, sometimes referred to as a time sweep.

In this technique, the values of in phase response V_x and out of phase response V_y are both monitored. On resonance, the in phase component of the Lorentzian will be at maximum while the out of phase component will be zero. Therefore, the ratio V_y/V_x will have a minimum at resonance. By varying the frequency to keep this ratio as small as possible, the oscillator can be kept on resonance. During a time sweep, the in phase component is also kept constant by varying the drive.

By applying the height-width-drive (equation 3.21), the value of V_x and the known drive can be used to find the resonance width, and therefore the temperature, for each data point taken. As data is typically taken once per second using this technique, resonance tracking can provide measurements of temperature at a very fast response rate at the cost of reduced accuracy when compared to an f-sweep. Due to this high response rate resonance tracking is typically used in parallel with other measurements to provide almost real-time thermometry data.

3.2.3 Amplitude Sweep

To investigate how the resonators used interact with the fluid, measurements of the force-velocity characteristics of an oscillator are often required as a means of determining the nature of the drag forces experienced by the device. While technically obtainable using a number of consecutive f-sweeps, this approach is very slow and a more efficient method is therefore required. Such measurements are instead made using an amplitude sweep, where the drive is varied while the oscillator is kept on resonance.

The range of an amplitude sweep is often very wide, typically covering multiple orders of magnitude in applied drive. This can lead to large variations in the measured drag during a single amplitude sweep, meaning the resonant frequency may also vary significantly. To keep the oscillator on resonance as the resonant frequency shifts we apply the same method as for resonance tracking, where the ratio V_y/V_x is minimised. In practice, this is applied by taking measurements only if this ratio is below a set threshold. If not the frequency is adjusted slightly, the measurement is retaken and the condition tested again.

To test for hysteresis, amplitude sweeps are usually performed from a low drive to a set maximum and then back down to the starting value. The results can be considered as two distinct sweeps, an up-sweep taken with increasing drive and a down-sweep taken with decreasing drive.

3.2.4 NEMS Measurements

Due to the significantly higher frequencies of the resonators, a different experimental setup was used with the NEMS. For these measurements, a high frequency network analyser was used to replace both the generator and the lock-in amplifier of the standard measurement scheme. While traditional lock-in amplifiers that function at these frequencies do exist, network analysers have become the standard method within the nanoelectronics community for similar measurements due to their improved performance at these frequencies.

Due to the high sensitivity of nanomechanical devices the input signal must be attenuated to prevent damage to the beam, with an attenuation of 40 dB typically used. A similar amount of gain (usually 40 dB) is then added to the returning signal to make it easier to measure.

In the experiments described here, two main types of measurement were performed using the network analyser. Despite the different instruments used, frequency sweeps using the network analyser are very similar to those described in section 3.2.1. The frequency is still swept through a chosen range of values while the drive is kept constant, though all data is now recorded by the network analyser.

Power sweeps are another frequently used technique, and are essentially a crude version of the amplitude sweep. Power sweeps using the network analyser consist of a series of consecutive frequency sweeps where the power applied to the beam is increased between sweeps. Power sweeps are usually performed in vacuum and used as calibrations before other measurements are carried out. Nanomechanical structures typically display a large amount of non-linearity, so vacuum power sweeps are an important way of ensuring all future measurements are kept within the linear regime.

The final technique we will use is referred to as a temperature sweep and, like the power sweep, essentially consists of a number of consecutive frequency sweeps. During a temperature sweep all parameters of the network analyser are kept constant while the temperature of the experimental cell is varied. This ensures all differences observed between sweeps are a result of the temperature changes.

In contrast to the traditional approach, measurements using the network analyser work in terms of the transmission and reflection of the electrical power applied to the circuit. Measurements of a resonance can be made by monitoring the transmission. When on resonance, some of the power provided is used to drive the motion of the beam and the resonance therefore appears as a drop in the transmitted power. Results from the network

analyser are given in terms of an electrical scattering matrix element, S_{21} , which can be defined in terms of the input voltage V_1 and the output voltage V_2 ,

$$S_{21} = \frac{V_2}{V_1}. \quad (3.34)$$

By squaring equation 3.34, we can obtain a similar expression in terms of the input power (P_1) and the output power (P_2):

$$|S_{21}|^2 = \frac{P_2}{P_1}, \quad (3.35)$$

where the resistance terms expected when converting voltages to power cancel, as both input and output are measured at the network analyser ports across a 50Ω impedance. In order to relate the measurements to physical properties of the resonance, we need to obtain an expression for the output power as experienced by the beam, labelled P_2^b . This can be related to the measured output power using the gain, G :

$$P_2^b G = P_2. \quad (3.36)$$

To be of practical use, we need to obtain P_2^b in terms of the experimentally measurable quantities S_{21} and P_1 . This can be achieved by substituting equation 3.36 into equation 3.35,

$$|S_{21}|^2 = \frac{P_2^b G}{P_1}. \quad (3.37)$$

Rearranging this for P_2^b then gives the expression required:

$$P_2^b = \frac{P_1 |S_{21}|^2}{G}. \quad (3.38)$$

Until now, this derivation assumes quantities are given in standard units, with P_2^b and P_1 given in Watts and $|S_{21}|^2$ and G treated as ratios. In reality, the network analyser measures the input power in dBm, so this must be converted to Watts:

$$P_1[\text{W}] = 10^{0.1P_1[\text{dBm}]}.$$
 (3.39)

To obtain the power loss caused by the resonance, P_r , we must first extract the change in the S_{21} signal due to the resonance. This can be done by subtracting the background, associated with other power loss such as Ohmic heating, from the measured value of S_{21} to obtain the amplitude of the peak, $S_{21,\text{Amp}}$. This is then used to calculate the power loss due to resonance:

$$P_r = \frac{P_1 |S_{21,\text{Amp}}|^2}{G}.$$
 (3.40)

To convert the measured signal and input power to physical quantities such as the velocity, we start by equating the two possible definitions of the quality factor (equations 3.22 and 3.23),

$$\frac{f_0}{\Delta f_2} = \frac{2\pi E_s}{E_1}.$$
 (3.41)

As we are working in terms of drops in transmission, in physical terms we can relate the S_{21} signal to the energy lost from the resonator, E_1 . By using the frequency to relate energy per cycle to power, $P_r = E_1 f_0$, equation 3.41 can be rewritten in terms of power:

$$\frac{1}{\Delta f_2} = \frac{2\pi E_s}{P_r}.$$
 (3.42)

The velocity can now be extracted from this by considering the stored energy E_s . Treating

the resonator as a simple harmonic oscillator, the stored energy is constantly converted between kinetic energy and potential energy. To find the peak velocity v_0 of the oscillations, we consider the point at which the stored energy is purely kinetic, $E_s = \frac{1}{2}mv_0^2$. Substituting this into equation 3.42 and rearranging for velocity now gives the desired expression:

$$\frac{1}{\Delta f_2} = \frac{2\pi m v_0^2}{2P_r}, \quad (3.43)$$

$$v_0 = \sqrt{\frac{P_r}{\pi m \Delta f_2}}. \quad (3.44)$$

An expression for the associated force can be found from this by using the definition of mechanical power, $P = Fv$,

$$F_0 = \sqrt{\pi m P_r \Delta f_2}. \quad (3.45)$$

If necessary, an expression for the maximum displacement of the beam can be found from the velocity by rearranging the traditional equation for velocity of an oscillator, $v = \omega x$:

$$x_0 = \frac{1}{2\pi f} \sqrt{\frac{P_r}{\pi m \Delta f_2}}. \quad (3.46)$$

3.2.5 Multifrequency Measurement Methods

One major drawback of the current approach used in operating the quasiparticle camera is the large number of instruments needed, as every pixel requires a unique lock-in amplifier to perform the measurements. An approach that allows measurement on multiple pixels using a single device is therefore desirable. With this in mind we investigated a multiple frequency lock-in analyser, referred to as the MLA, which enables excitation and measurement on up to 42 different frequencies simultaneously, so long as all frequencies

used are integer multiples of some minimum measurement frequency [68].

The MLA was originally developed for use in atomic force microscopy, where the oscillator used is a cantilever beam with a tip on one side. Contact between the tip and the surface being investigated alters the oscillations, with the variation in resonance behaviour used to deduce properties of the surface. In intermodulation atomic force microscopy the cantilever is instead driven at two different frequencies close to resonance. Contact between beam and surface then causes non-linearity in the resonance, introducing intermodulation products to the frequency spectrum measured. The measured intermodulation products can then be used to obtain information on the surface [69, 70].

For our purposes, we consider two potential use cases of this functionality. By connecting a large array of oscillators, it may be possible to use the MLA to measure the frequency characteristics of a large number of devices simultaneously. Performing separate frequency sweeps on all available MLA channels should in theory allow simultaneous measurements on 42 different oscillators. Unfortunately the requirement that all frequencies used are integer multiples of a set base frequency complicates this significantly. This drawback could potentially be worked around with very careful design of the devices used, but for now this possibility remains untested.

The MLA should also be able to characterise the resonance of a single oscillator by choosing excitation frequencies spaced around the resonance frequency of the oscillator. By measuring the response of all of these frequencies simultaneously, a profile of the resonance should be obtainable in a single measurement. This method, which we refer to as a frequency comb, should produce results equivalent to a conventional f-sweep in a shorter space of time. As an important note, this method is only valid for a linear resonance. Any non-linearity in the oscillator could introduce unpredictable intermodulation products and render the results unreliable.

In practice an upgrade to the camera based on multifrequency techniques could of course

apply both of these possible uses. In the case of 42 separate oscillators connected to the MLA through a common line, frequency combs could be taken of each device before the start of a measurement to rapidly and accurately characterise the resonances of every oscillator. A variant of the resonance tracking method currently used could then be applied to monitor all 42 devices simultaneously and record how they vary over time. Since the current measurement scheme requires a unique lock-in amplifier for every camera pixel, switching to a multifrequency approach may allow us to vastly increase the resolution of the camera while also reducing the number of instruments needed to take the measurements.

3.3 Thermometry

At very low temperatures accurately determining the temperature of an experiment is not trivial, with a wide variety of potential methods available. These different approaches all come with associated advantages and drawbacks, so the choice of which to use must be made carefully.

The available methods can be split into two categories. These are primary thermometers, which can be used reliably without any prior calibration, and secondary thermometers, which must be calibrated before they can be used. Although these definitions imply primary thermometers are universally better than secondary, in practice primary thermometers are frequently difficult to work with experimentally. Secondary thermometers are often preferred as they are easier to work with and no less accurate if calibrated successfully.

Due to the wide variety of measurements performed, a range of different methods were used to determine the temperature during these experiments. For the measurements performed in ^4He , the vapour pressure of the helium produced due to boil-off of the liquid was used to deduce the pressure. As the pressure is related to the temperature by the well known ^4He phase diagram, this can be considered a primary thermometer.

However, there is one major issue associated with the use of vapour pressure for thermometry. The relationship between pressure and temperature is only known along the boiling curve of the phase diagram, and it is therefore possible for this method of finding the temperature to become inaccurate if the state of the helium drifts away from this boiling curve. Even worse, it is impossible to tell if this has happened from the pressure measurements. Thankfully this only becomes an issue if the pressure is allowed to increase, so long as pressure is decreased steadily the helium can be kept safely on the boiling curve and the temperature readings provided by this approach remain reliable.

For the measurements performed in ^3He the thermometry required is more complicated as the temperature cannot be directly calculated from the cryogenic methods used. As the cell contains a wide range of different oscillators, it makes sense to use these resonators as thermometers.

In order to calculate temperature from measurements of these devices, we must combine the theory of drag in ^3He (section 2.2.4) with the theory of oscillating devices (section 3.1.1). As discussed earlier the drag in ^3He can be split into three components, $F = F_0 + F_T + F_{\text{pb}}$, where F_0 is the intrinsic drag, F_T is the thermal component and F_{pb} is the drag due to pair-breaking. To determine the temperature we are only interested in the thermal component.

In experimental terms the width of the oscillator resonance is connected to the drag, with the width increasing as drag increases. By combining an expression for the thermal width (equation 3.20) with an equation for the thermal force at low velocity (equation 2.63), an expression for the thermal width Δf_2^T can be derived:

$$\Delta f_2^T = \frac{F^T}{2\pi m v_0}, \quad (3.47)$$

$$\frac{F^T}{v_0} = \frac{F_{v \rightarrow 0}^T}{v} = \frac{2d\gamma p_F^2 \langle nv_g \rangle}{k_B T}, \quad (3.48)$$

$$\Delta f_2^T = \frac{d\gamma p_F^2 \langle nv_g \rangle}{\pi m k_B T}. \quad (3.49)$$

During the previous discussion of drag in ^3He an expression for the quasiparticle flux $\langle nv_g \rangle$ was obtained (equation 2.54), which can now be substituted into equation 3.49:

$$\Delta f_2^T = \frac{d\gamma p_F^2 g(p_F)}{\pi m} \exp\left(\frac{-\Delta}{k_B T}\right). \quad (3.50)$$

As all terms outside the exponential on the right-hand side of this equation are constant, we can simplify this by absorbing these into a single number, which we refer to as the width parameter, A :

$$\Delta f_2^T = A \exp\left(\frac{-\Delta}{k_B T}\right). \quad (3.51)$$

The value of this width parameter, different for each wire, is then determined experimentally [71]. To enable use for thermometry, equation 3.51 can be rearranged to find an expression for the temperature:

$$T = \frac{-\Delta}{k_B \ln\left(\frac{\Delta f_2^T}{A}\right)}. \quad (3.52)$$

So long as the value of the width parameter A is known, equation 3.52 can be applied to calculate the temperature. However, as the width parameter is determined experimentally, oscillators do not count as primary thermometers. Since there are so many oscillators present in the cell used here, it would be highly inefficient to perform full calibrations for each one individually. Conveniently, the width parameter is found to be almost identical

for devices of the same size. This can be seen by plotting the thermal width of one device against the thermal width of another with the same dimensions (figure 3.3), as the gradient of this plot is equal to the width parameter ratio for the two devices. Figure 3.3 Compares mmm1 and mmm2, both of which are $4.5 \mu\text{m}$ diameter wire resonators. Comparison to the black line shows this plot has gradient 1 and the width parameters are therefore identical for the two lines. Calibrations obtained for a single $4.5 \mu\text{m}$ wire can therefore be applied to all other wires of the same diameter.

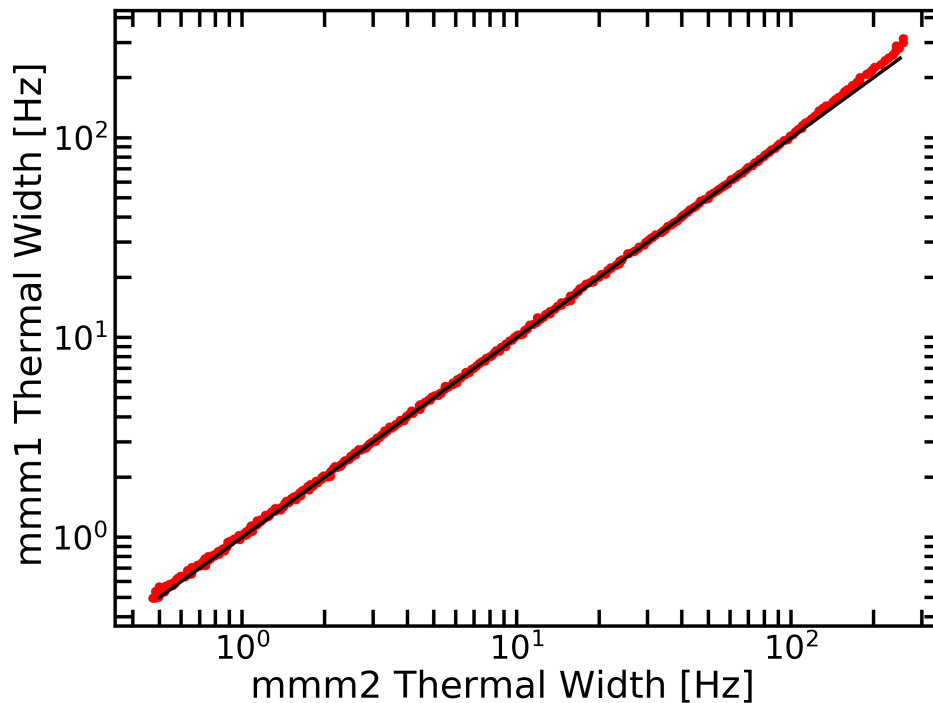


Figure 3.3: Thermal width of wire mmm2 plotted against thermal width of wire mmm1, both wires of diameter $4.5 \mu\text{m}$. The black line of gradient 1 shows the width parameter is the same for both wires.

For other devices, temperature is calculated through comparisons to the $4.5 \mu\text{m}$ wires. This enables any oscillator in the cell to be used as an accurate thermometer without requiring lengthy calibrations. To enable the comparison between the calibrated $4.5 \mu\text{m}$

wire and other devices, the resonance response of each device was measured at a wide range of different temperatures as the cell warms up due to background heat leaks during an experiment. This data was then used to plot the width of wire Mg (0.9 μm diameter) against the width of wire mmm2 (figure 3.4).

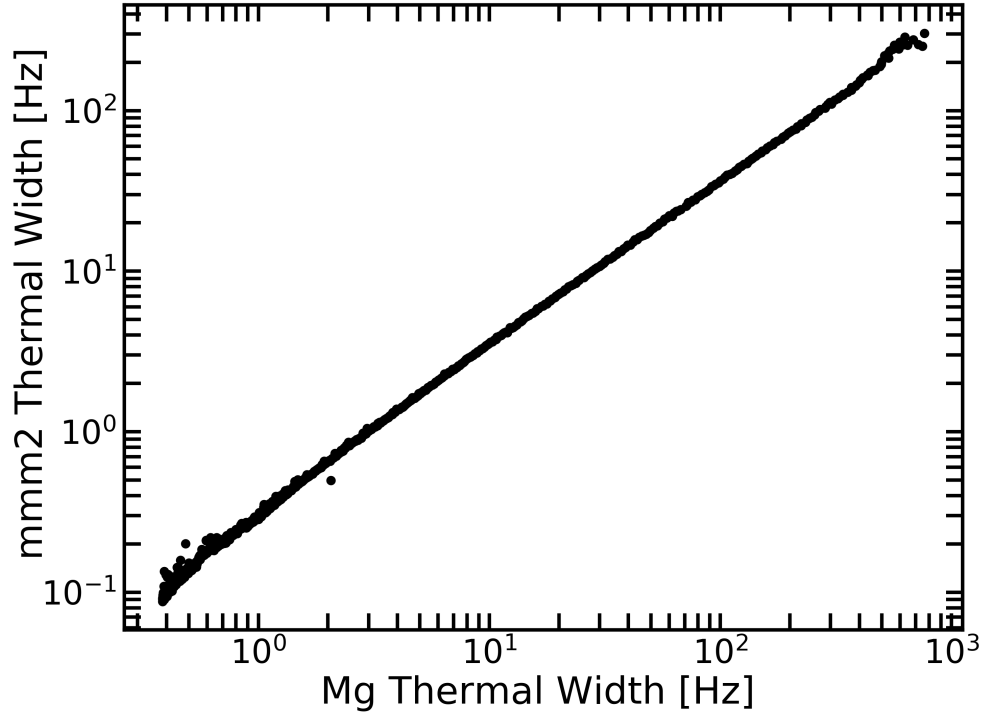


Figure 3.4: Thermal width of wire Mg plotted against thermal width of wire mmm2.

Figure 3.4 can now be applied to enable thermometry from measurements of Mg. The thermal width of Mg, Δf_2^M , can be calculated from the thermal width of mmm2, Δf_2^m , using figure 3.4:

$$\Delta f_2^M = B \Delta f_2^m, \quad (3.53)$$

where B is the gradient of the line shown in figure 3.4. Combining equations 3.52 and

3.53, an expression can now be found for the temperature in terms of the thermal width of Mg and the width parameter of mmm2, labelled A_m for clarity:

$$T = \frac{-\Delta}{k_B \ln \left(\frac{\Delta f_2^M}{A_m B} \right)}. \quad (3.54)$$

Equation 3.54 can then be applied to calculate temperature from the width of Mg without having to perform full calibrations for this wire. By repeating this method, all oscillators can be used as thermometers even though only a single $4.5 \mu\text{m}$ wire has been strictly calibrated.

All temperature measurements for the ^3He experiments are taken by applying this approach to the oscillators in the cell. Typically all oscillators not otherwise in use during a measurement are set to undergo resonance tracking before the measurements are started. The values of this can then be used with the method above to calculate the temperature. As this often enables simultaneous temperature measurements on a number of oscillators, the results obtained with different devices can be compared to check for temperature gradients within the cell.

3.4 Experimental Cell Layouts

To obtain the wide range of different results discussed here, a number of different cells were used. As discussed in section 3.3 the temperature of all ^4He measurements was deduced from the vapour pressure of the helium. This external thermometry means all devices included in the ^4He cells are left free for other uses. The only devices included in the first cell, used to test the multifrequency measurement methods described in section 2.2.5, were two tuning forks. The cell design used for NEMS measurements was very similar, as this cell simply contained two beams. The beams in the NEMS cell were designed to be replaceable, allowing the same cell to be used for testing a wide variety of beams.

In ^4He , where cooling from room temperature to base temperature within a day is possible, simple cells such as these are useful as the cell can be changed between every measurement if necessary. In ^3He , where these time frames are much longer, cells containing a wide range of devices are much more efficient as they allow multiple distinct measurements to be performed using a single cell. For this reason all ^3He measurements discussed here were carried out in the same cell, shown in figure 3.5.

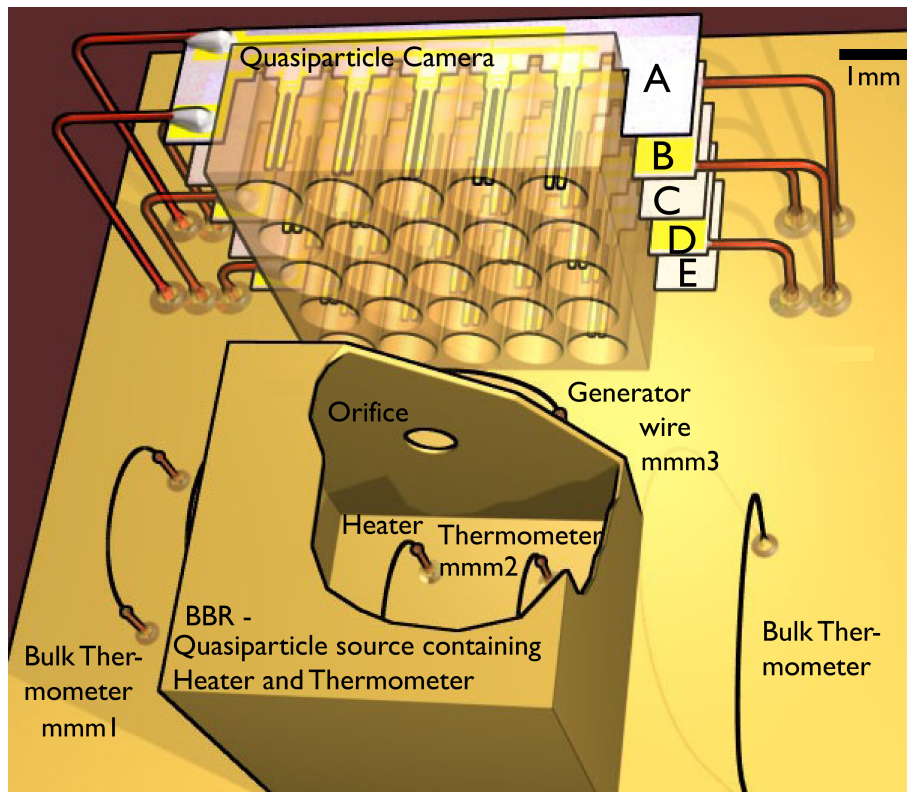


Figure 3.5: Diagram of the devices inside the cell used for all ^3He measurements, showing the geometry of the cell. For a more detailed description of the relevant devices, see text.

Although originally designed to be used together as a quasiparticle camera [12], this cell was chosen for our experiments solely due to the large number and wide variety of devices included. As such, many of the devices visible in figure were not used at all in our experiments. A single fork from within the 25 pixel camera array, labelled D2, was used

for all tuning fork measurements performed here. The four thinnest vibrating wires, one with diameter $0.9 \mu\text{m}$ and three with diameter $4.5 \mu\text{m}$, were frequently used in our measurements. The thinnest of these, referred to as Mg, was used as a thermometer wherever possible as its small size made it the most sensitive for these purposes. As the same device cannot be used for measurements and thermometry at the same time, any of the other three wires could be used as a thermometer when necessary. The three $4.5 \mu\text{m}$ wires are referred to as mmm1, mmm2 and mmm3 and labelled on figure 3.5 for clarity. Mg was placed on the opposite side of the quasiparticle source to the camera array and is not visible in figure 3.5. The bulk thermometer on the right hand side of the quasiparticle source is much thicker than the others, with a diameter of $125 \mu\text{m}$, and is used for thermometry in the normal fluid regime. This wire is therefore primarily used as a diagnostic tool during fridge operation and is not used in experimental measurements.

4 Multifrequency Lock-in Measurements

As detailed in section 3.2.5, two potential improvements to the quasiparticle camera are suggested that require the use of an Intermodulation Products multiple frequency lock-in analyser (MLA) [68]. To check that these new methods are valid, we must first prove that the MLA is capable of producing results equivalent to those obtained using a traditional lock-in amplifier. In these experiments, we use a Stanford Research Systems SR830 lock-in amplifier as the conventional approach.

To test the frequency comb method, measurements were made on a pair of tuning forks. The fork lengths chosen, $L = 2600 \mu\text{m}$ and $L = 2200 \mu\text{m}$, gave approximate resonant frequencies of 12 kHz and 16 kHz respectively. The forks were identical in all other dimensions, with tine width $W = 25 \mu\text{m}$, thickness $T = 90 \mu\text{m}$ and a spacing of $D = 75 \mu\text{m}$ between the tines.

Before any comparisons were made between frequency sweeps and frequency combs, some

basic measurements were taken to test the frequency comb method. As the major potential advantage of a frequency comb is the possibility of faster measurement times, frequency combs were performed at a range of different speeds. These measurements were performed using the 16 kHz fork and, for simplicity, taken in vacuum at room temperature.

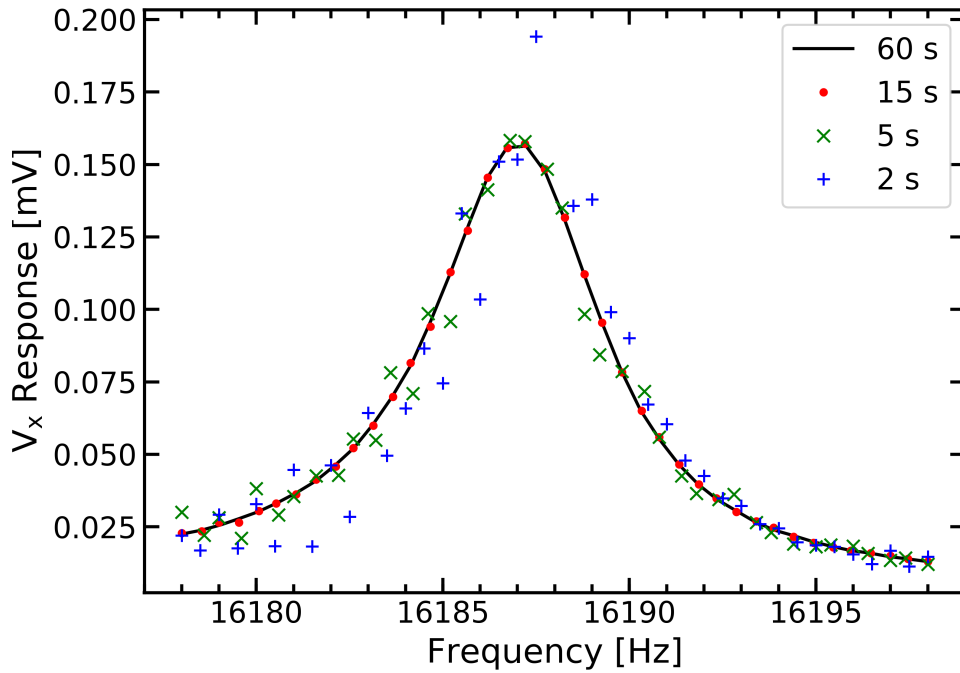


Figure 4.1: Four measurements of the in-phase (V_x) component of the resonance for the 16 kHz fork, obtained using frequency combs at a variety of different measurement durations, showing the improvement of the results with longer measurement times. As frequency combs were used to obtain these results, the quoted times correspond to the total measurement duration.

Firstly, figure 4.1 shows clearly that the frequency comb approach is capable of producing an accurate resonance profile. In terms of measurement times, 60 s and 15 s both give very clear results, with minimal deviation from the expected Lorentzian shape. As demonstrated by the 5 s and 2 s results, reducing the measurement time further visibly reduces the accuracy of the profile obtained. However, though noisier, the shape of the

5 s results is sufficiently close to a Lorentzian lineshape to give reasonably accurate values of properties such as width and resonant frequency in a remarkably short amount of time. Although the 2 s results are too inaccurate to be of much use in any experimental context, it is still remarkable how reasonable the results are given the timeframe of these measurements. Weighing the necessary trade-off between accuracy and measurement time the 15 s data seem to provide the best compromise, appearing very similar in accuracy to the slower measurement despite the shorter time taken.

In preparation for comparisons between frequency sweeps and frequency combs, the experimental setup was designed to allow measurements to alternate between the two methods without any external changes for experimental convenience. This circuit, shown in figure 4.2, used a summation amplifier to apply the output from both generators to the same fork. A 20 dB attenuator was used to reduce the input signal and prevent damage to the sensitive fork. In accordance with the typical approach to fork measurements described in section 3.2, the fork response was passed through a custom made IV converter [67] to change the output current into a voltage measurable by the lock-in amplifiers.

As we are primarily interested in the cryogenic performance, the forks were then cooled using a ^4He immersion cryostat. Varying the pressure of the helium bath of the cryostat gave access to temperatures from 4.2 K down to a base temperature of approximately 1.45 K. The temperature was inferred directly from the pressure above the helium bath. The forks used for the measurements were immersed directly in the bath of the cryostat.

To provide a simple comparison, measurements of the 12 kHz fork were taken using both methods with the fork immersed in helium at the base temperature of the cryostat. The frequency sweep used includes 60 points, with 1 second measurement time per point. For the frequency comb, 40 points were taken and the measurement was performed in 40 s. The measurement times chosen here were largely arbitrary, with the exact values used chosen to ensure there was minimal noise in the data.

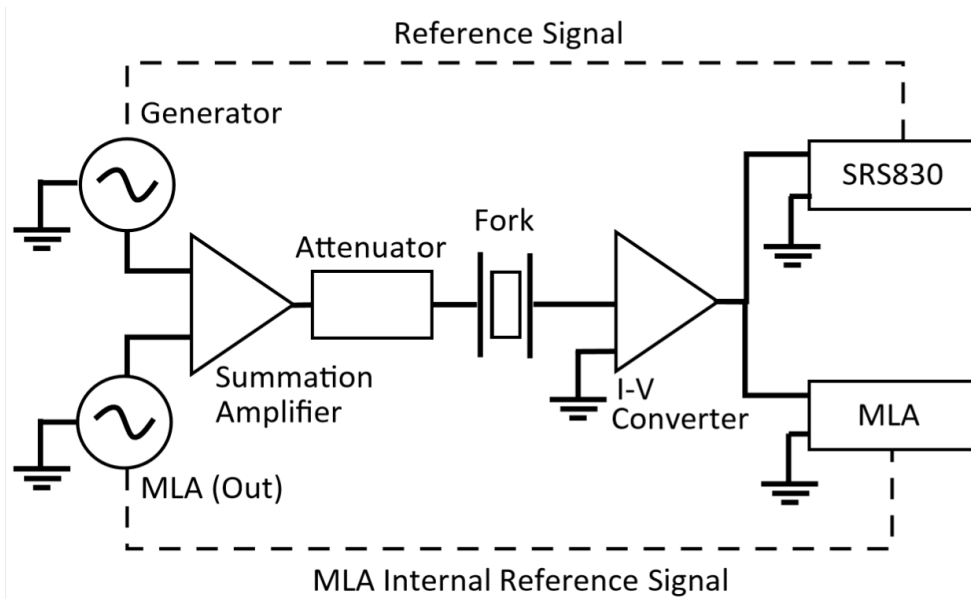


Figure 4.2: Schematic of the circuit used, designed so that measurements could alternate between the two devices [72].

The results of this, seen in figure 4.3, clearly show very close agreement between the two methods. This serves as a rough proof of concept by showing that, at least in the most basic possible case, the new frequency comb does give analogous results to the traditional method. To enable this agreement, the measured response must be normalised to account for differences in the size of the drive applied in each method. The normalised signal shown was obtained by dividing the output current produced by the applied input voltage.

Due to the different approaches used, different values of the excitation voltage applied were necessary. For the frequency sweep, a constant voltage of 50 mV was applied for all points in the sweep. As all frequencies are excited simultaneously during a frequency comb, a smaller per point excitation of 20 mV was chosen to keep the maximum applied power close to that of the frequency sweep. For comparisons, values of the power were calculated electrically ($P = IV$) with the total power for the frequency comb acquired by summing over all simultaneously driven frequencies.

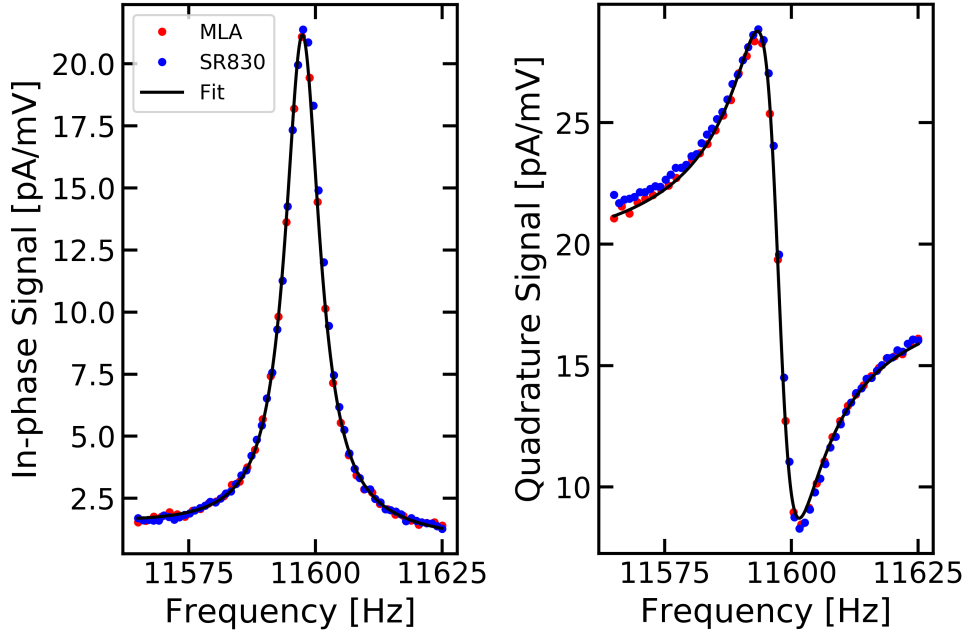


Figure 4.3: Comparison of the in-phase and quadrature components of the 12 kHz tuning fork resonance as measured with both methods in superfluid ^4He at approximately 1.5 K. The signal is given as a normalised response to account for differences in applied excitation between the two approaches.

Calculating the peak powers applied, we find that the frequency sweep has a peak power of approximately 0.4 pW, while the simultaneous measurements of the frequency comb lead to a higher peak power of 0.6 pW. It is worth noting that the case will be very different for total power, where the greater excitation magnitude and larger number of measured points will lead to a higher total applied power for the frequency sweep method. Although the full calculations depend on the exact values chosen for the applied drive and number of points measured, in general the peak power will always be higher for the frequency comb. The parameters must therefore be chosen carefully when applying this method as excessive peak power will lead to the nucleation of turbulence and so introduce non-linearity to the system. Although not yet tested experimentally, this non-linearity is expected to compromise the accuracy of the frequency comb method through the creation

of unwanted intermodulation products.

Stronger proof of the viability of the frequency comb approach can be obtained by extending these comparisons to the full temperature range measurable, thereby demonstrating that the two methods give equivalent results under a wide range of different experimental conditions. In practice this was achieved by using both methods alternately while the temperature was reduced from 4.2 K to 1.5 K. Values of the resonance frequency and width were obtained by fitting a Lorentzian to the results of each individual sweep or comb. Assuming the drag is purely hydrodynamic, theoretical predictions for the temperature dependence of the damping are given by equations 2.25 and 2.29. The values of ρ_{He} , ρ_{N} and η required for these calculations are taken from Donnelly and Barenghi [35]. Comparisons between the theoretical and experimental sets of results ensure the measurements are consistent with the theory used.

As shown in figure 4.4, comparisons between SR830, MLA and theoretical calculations all agree very closely throughout the whole temperature range tested. The value of $C = 0.404$ obtained for the fitting parameter is slightly smaller than previous measurements on 75 μm width forks. Typical values for the 75 μm forks range from $C = 0.518$ to $C = 0.757$, with a trend towards higher values as frequency increases. Prior experiments with larger forks of similar resonant frequency typically report higher values of the fitting parameter C , so it is reasonable to assume the lower value recorded for the 25 μm forks used here is also attributable to the reduced width.

Fits to the frequency ratio (figure 4.5) are clearly not as close, with significant disagreement between the experimental results and the theoretical predictions at the lowest measured temperatures. In fact, this discrepancy can largely be removed by treating the vacuum frequency of the oscillator as an additional fitting parameter. Unsurprisingly the value of $f_0 = 11749$ Hz given by the fit is very close to the experimentally determined value of $f_0 = 11730$ Hz. However, as shown in figure 4.6, this small change in vacuum frequency

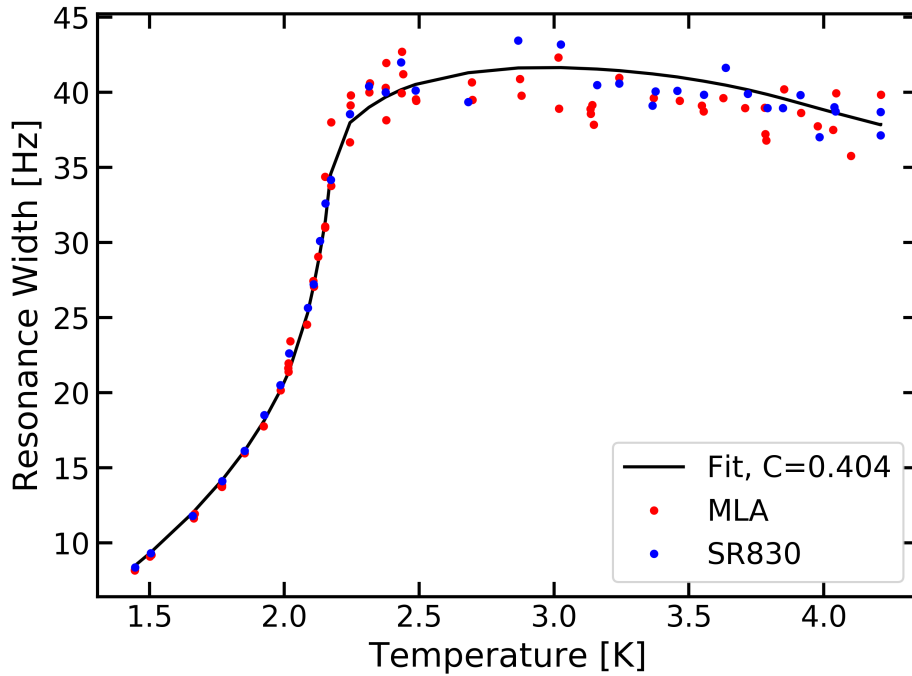


Figure 4.4: Resonance width as a function of temperature, measured for the 12 kHz fork using MLA (red) and SR830 (blue). The black line is a fit to equation 2.29.

causes a significant change in the quality of the fit.

Close inspection reveals that this corrected fit is still not perfect, with some disagreement now visible in the normal fluid results just above the transition to superfluid. Although the improvement to the fit in the superfluid regime supports figure 4.6, this new fit can only be considered valid if a suitable physical explanation for the shift in vacuum frequency can be found. Thankfully, changes in the vacuum frequency are plausible in the cryostat used.

As all experiments were performed in the main bath of the cryostat there is a reasonable possibility of contamination with impurities such as oil or water present in the helium supply. Due to the low temperature any potential impurity would be solid and therefore capable of adhering to the surface of the fork. Such unexpected additions to the mass

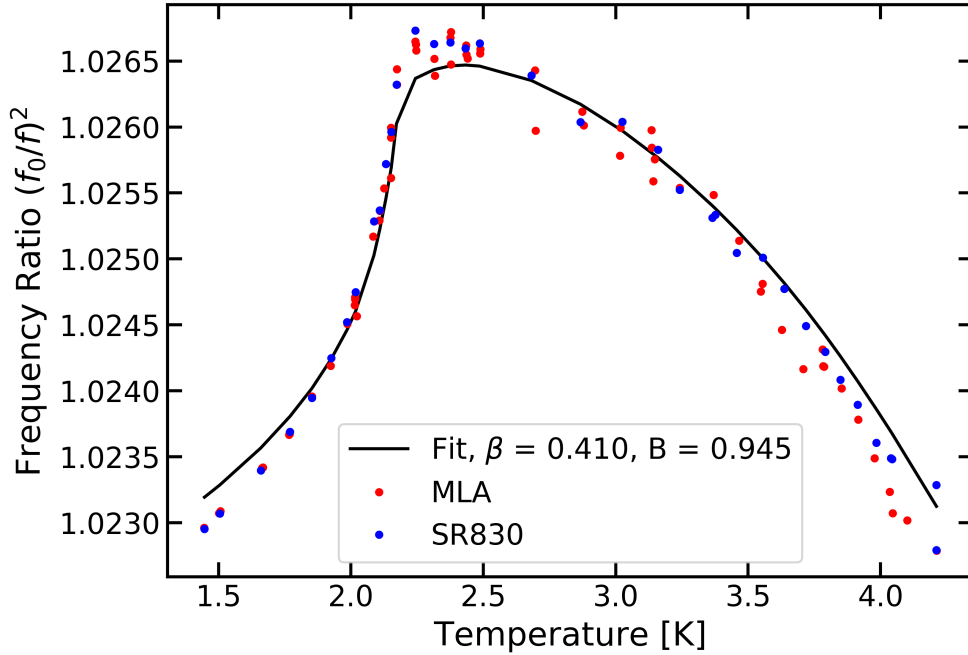


Figure 4.5: Frequency ratio as a function of temperature, measured for the 12 kHz fork using MLA (red) and SR830 (blue). The black line is a fit to equation 2.25.

and profile of the oscillator would inevitably lead to variation in the resonant frequency. The increase in vacuum frequency seen here is inconsistent with an addition to the effective mass, but could be explained by an imperfection present from previous experiments detaching from the fork.

Such variations in effective mass were often observed qualitatively during these experiments, with values of the fitting parameters proving highly difficult to reproduce exactly over consecutive experiments. Despite the changes in the values of the fitting parameters, every different set of measurement still showed solid agreement between the measured data and the theoretical fits. This strongly suggests the model is still valid and the change in fitting parameters is therefore best explained by variation in one of the values treated as a constant.

Regardless of these minor issues with the physical interpretation, in terms of the exper-

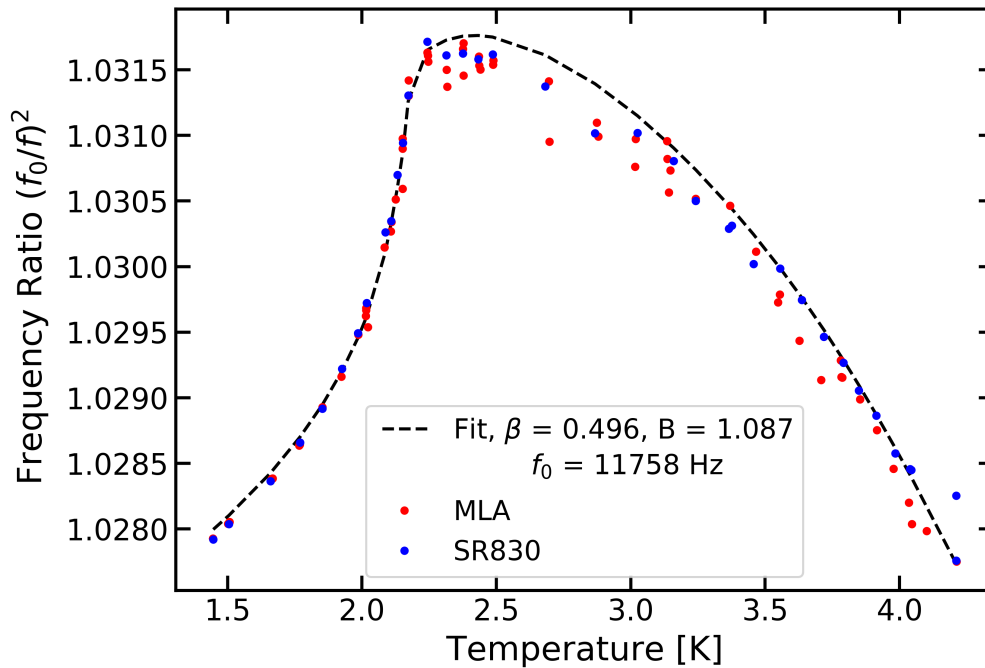


Figure 4.6: Frequency ratio as a function of temperature, measured for the 12 kHz fork using MLA (red) and SR830 (blue). The black line is a fit to equation 2.25, with the resonance frequency now treated as an additional fitting parameter.

imental techniques tested the results obtained reveal a great deal of success. As shown in figures 4.4 and 4.6, the values of resonant frequency and width as measured by the frequency comb approach agree closely with those obtained using traditional frequency sweeps throughout the whole temperature range tested. Significant amounts of noise are visible in the results of both methods, though there appears to be little difference in the magnitude of this noise between the different techniques. Perhaps most importantly, there is no sign of any systematic offset between the values obtained. This proves that the agreement shown in figure 4.3 is not a specialised case and we can therefore assume that the two approaches are indeed equivalent so long as the response of the device measured remains linear.

Before commenting on the plausibility of employing these new methods to improve the

quasiparticle camera, it is important to note that any such application would require the use of multifrequency methods in ^3He . Although leading to significant differences in terms of physical properties such as viscosity, changing the experimental fluid to ^3He should not affect the validity of the frequency comb method and we should in theory be able to use this approach in ^3He without any problems. It would however seem sensible to verify this with some simple measurements in ^3He before applying this method to real experiments. Unfortunately, due to the inaccuracy shown by the very short measurement time results, the frequency comb is not viable as a replacement for the resonance tracking approach used currently in the operation of the quasiparticle camera. Currently the vast majority of tracking measurements are performed with data acquisition rates of either one point per second or ten points per second. Figure 4.1 clearly shows that results taken at this speed using the frequency comb method would be too inaccurate to be of any experimental use. Figure 4.1 does however also show that the frequency comb technique is capable of obtaining a highly accurate profile of the resonance in as little as 15 s. In comparison to the frequency sweeps currently used, this could provide a much faster method of performing the preliminary resonance measurements required on each fork before the tracking method can be applied. This would significantly reduce the time required to calibrate the camera.

5 Probing Superfluid ^4He with Nanomechanical Resonators

One major field of development in terms of instrumentation is the drive towards miniaturisation. The use of microelectromechanical systems (MEMS) and nanoelectromechanical systems (NEMS) is now well established in other fields [63–65], with some of these devices showing exceptional sensitivity to changes in mass. However, the application of these devices to superfluid research is still largely untested. If the sensitivity observed in other applications can be replicated for our purposes, these devices could prove very helpful in future.

Additionally, the small size of these devices may also prove beneficial for future redesigns of the quasiparticle camera experiment. Using smaller devices may allow us to include more devices in the same physical area and so add more pixels without increasing the overall size of the camera.

Our experiments were all performed in a simple ^4He cryostat. All cooling in this setup is then achieved by pumping on the helium, reducing the pressure of the gas produced and so causing cooling due to the shape of the phase diagram. Due to the relatively high power of the vacuum pump used a base temperature of approximately 1.3 K was possible using this approach.

All measurements were taken using a network analyser, using a simple electrical setup. As the network analyser both generates and measures the signal, no other external device was needed. However, due to the small size of the beam, the power applied must be kept low to avoid damaging the device. To achieve this a system of attenuators and amplifiers reduces the outgoing signal to prevent damage to the beam and then boosts the returning signal so that it can be easily detected.

As shown in unpublished preliminary measurements performed in Lancaster, beams such as these typically exhibit a large amount of non-linearity as the applied power increases. Before any other measurements can be performed the input power at which the non-linearities appear must therefore be located to ensure all future measurements are kept below this. The simplest way to do this is to record the resonance characteristics at a wide range of input powers, as the appearance of non-linearities is dramatic enough to be easily visible in these plots. These measurements were performed in a vacuum to ensure they corresponded to the lowest damping case possible.

Performing these measurements for our 50 μm beam gave the characteristics shown in figure 5.1. From figure 5.1 we can observe multiple different non-linearities. At 2.5 pW input power a split resonance begins to appear, with a secondary peak appearing at

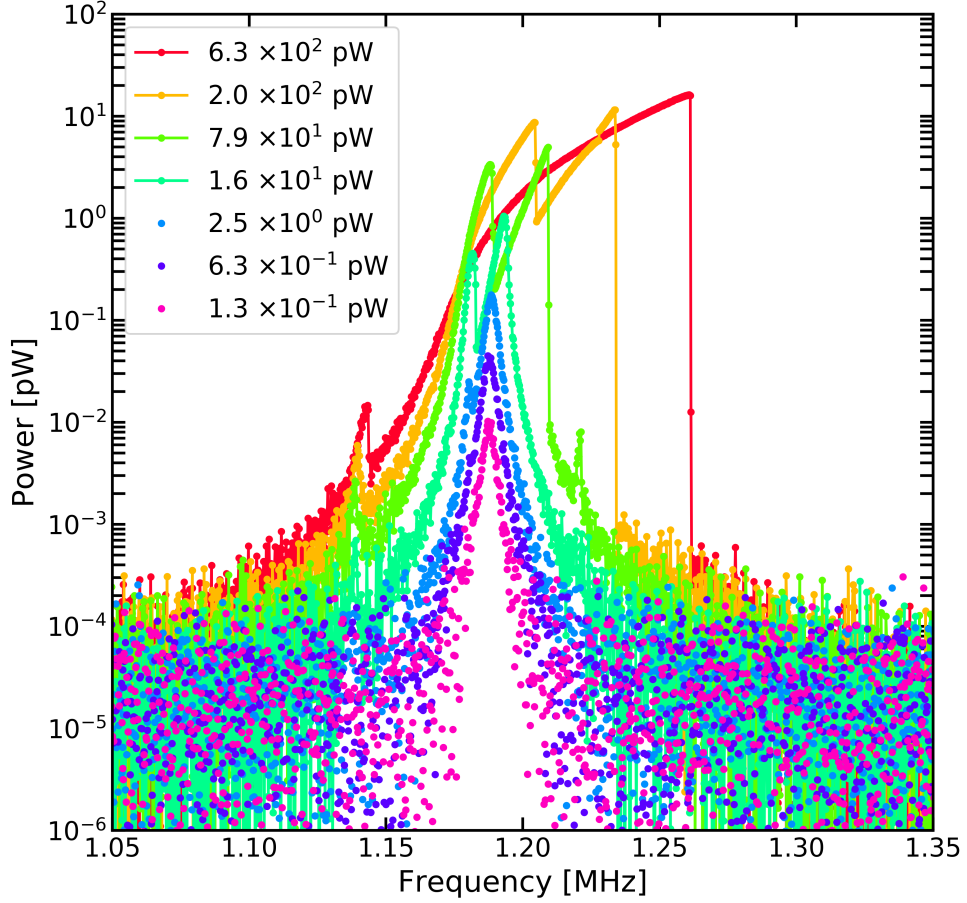


Figure 5.1: Output power before amplification as a function of frequency for measurements at a wide range of different input powers, showing the onset of non-linearity in the resonances.

frequencies just below that of the main resonance. At input powers above 1.6×10^1 pW we also see the shape of both resonances become Duffing-like. At the highest input power tested, 6.3×10^2 pW, the secondary peak vanishes as the Duffing effects dominate. Small additional peaks also appear above and below the main resonance at higher powers. Above 7.9×10^1 pW, two new features appear, one at around 1.15 MHz and the other at roughly

1.22 MHz. However, the feature at 1.22 MHz is hard to spot at even higher powers, presumably due to the increased importance of the Duffing non-linearity for these powers overwhelming the effects of this small feature.

With the vacuum calibrations completed, the beam was immersed in ^4He to see if nanomechanical structures could replicate results obtained with larger oscillating structures. Similar to the measurements described in section 4, the properties of the beam resonance were monitored as the temperature of the ^4He was reduced from 4.2 K to 1.3 K. As the simplest possible way to prove that the properties of the beam were changing due to the surrounding helium, the resonance response was plotted at a range of different temperatures. All of these measurements were taken using an applied power of -30 dBm, this drive was kept constant to ensure all changes observed are due to variations in the drag applied.

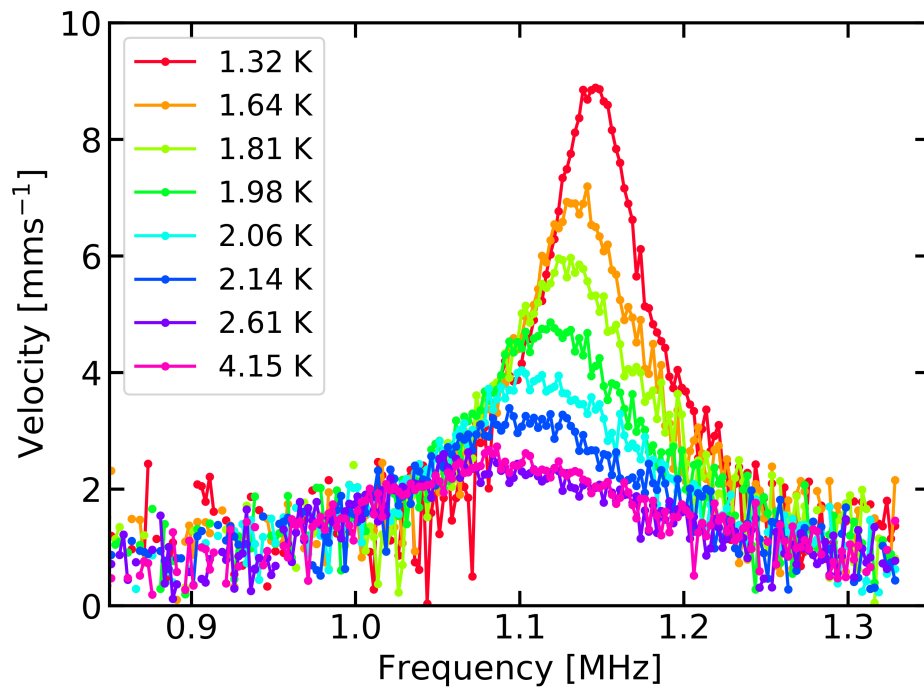


Figure 5.2: Oscillator velocity as a function of frequency for measurements at temperatures ranging from 1.32 K to 4.15 K.

Figure 5.2 shows the results of this, revealing data that is entirely consistent with the expectations due to immersion in helium. Comparing the data taken at 2.61 K and 4.15 K show little change, with very little difference between the two data sets. This is as expected, as both of these are above the transition to superfluid and little variation should occur due to such small temperature changes in normal fluid. All the data taken below the superfluid transition also behave exactly as expected, with the amplitude of the resonance increasing steadily as the temperature falls. This is easily explained by the decrease in drag as the fraction of superfluid present increases. The velocities shown in figure 5.2 were obtained using equation 3.44. The values of width needed for this calculation were obtained by fitting to the raw measurements.

To provide even stronger confirmation of the successful measurement of superfluid properties using NEMS, the variations observed with temperature need to be quantified and compared to the relevant theoretical predictions. The method used here is identical to that applied in section 4. As detailed in section 2.1.4, expressions for the changes in resonance width and resonant frequency as temperature changes can be derived. The expressions obtained are restated below as equations 5.1 and 5.2:

$$\frac{f_0^2}{f_{\text{He}}^2} = 1 + \frac{\beta \rho_{\text{He}}}{\rho} + \frac{B \rho_{\text{N}} S}{\rho V} \sqrt{\frac{\eta}{\pi \rho_{\text{N}} f_{\text{He}}}}, \quad (5.1)$$

$$\Delta f_2 = \frac{CS}{2m} \left(\frac{f_{\text{He}}^2}{f_0^2} \right) \sqrt{\frac{\rho_{\text{He}} \eta f_{\text{He}}}{\pi}}, \quad (5.2)$$

where β , B and C are geometrical coefficients, expected to be of order unity.

By taking many measurements as the cryostat is cooled, the experimental results can be compared to these theoretical predictions across the whole range of temperatures available. Agreement between these will therefore prove that the temperature dependence of the sweeps shown in figure 5.2 is indeed caused by the changes in the properties of the helium.

In practice this comparison is performed by attempting to fit equations 5.1 and 5.2 to the measured data, treating the geometrical coefficients as fitting parameters. The temperature dependence of these equations appears in the variation of the properties of the helium (ρ_{He} , ρ_{N} and η) with temperature [35]. If the measured data agrees with the predictions the theoretical fits should match well to the data using a sensible value of the fitting parameters.

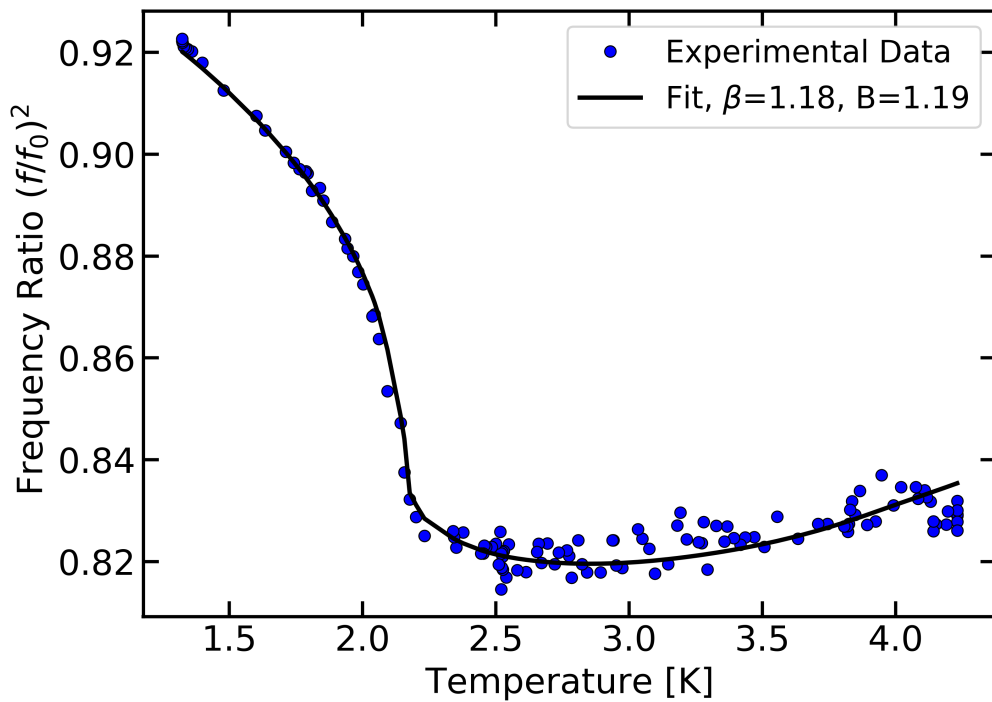


Figure 5.3: Comparison between experiment and theory for the frequency shift observed as the helium temperature changes.

Figure 5.3 shows very good agreement between actual measurements of the frequency shift and the behaviour predicted from changes in the helium properties due to the transition to superfluid. As expected the most significant feature in this plot is the dramatic change due to the superfluid transition at 2.2 K, a feature clearly visible in both data sets. As further proof, both calculated and measured data show the same curvature across the whole

temperature range measured. This agreement is best below the transition to superfluid, with additional noise above the transition leading to greater spread in this region. However, even with this noise the general shape of the different sets of data still agree well.

Further evidence for the success of these measurements can be found by considering the obtained values of the geometric coefficients, $\beta = 1.18$ and $B = 1.19$. These values are of order 1, as anticipated, and also agree well with values obtained in similar experiments using more traditional resonators such as vibrating wires and tuning forks.

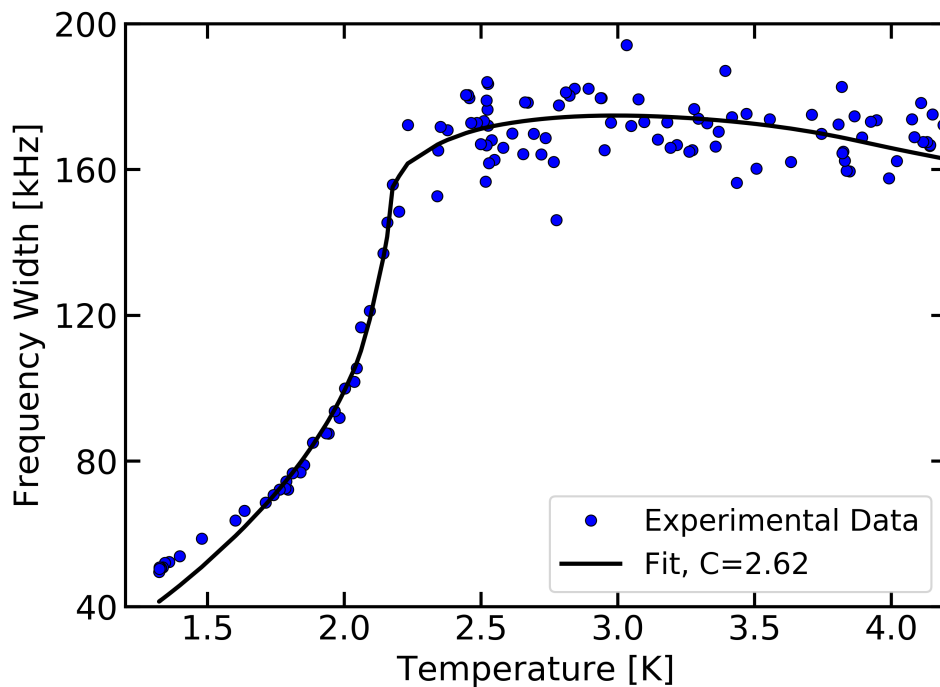


Figure 5.4: Comparison between experiment and theory for the change in width measured as the cryostat is cooled.

While figure 5.4, comparing measurements of frequency width to predictions, still shows good agreement between both sets of data it does also reveal some discrepancies. Above the superfluid transition the theory and experimental results do match across the whole range of values, though this regime contains a significant amount of noise with a large

spread visible even between data at very similar temperatures. Since this issue can be adequately explained by additional noise it does not contradict the agreement between the data sets.

However, a much more interesting discrepancy occurs at the lowest temperatures measured. Below temperatures of approximately 1.7 K the agreement between theory and experiment breaks down somewhat, with the measurements consistently higher than the theoretical prediction. Since this only occurs for a small subset of the total data range it does not invalidate our theory, but it does show that the model used is incomplete.

A likely reason for this discrepancy can be found by considering the viscous penetration depth of superfluid ^4He , shown earlier as equation 2.21 and restated here for convenience:

$$\delta = \sqrt{\frac{\eta}{\pi \rho_N f_{\text{He}}}}. \quad (5.3)$$

As stated in section 2.1.4, the derivation of the hydrodynamic damping model used assumes the viscous penetration depth is smaller than the size of the oscillator. Due to the very small size of the beams used this condition may not be true, in which case the model used is unlikely to be completely accurate. To test this suggestion, values for the viscous penetration depth were calculated across the whole temperature range of the experiment. The results obtained are shown in figure 5.5. Comparing figures 5.4 and 5.5 appears to confirm our suspicions, with the breakdown of the hydrodynamic damping model happening at a temperature of 1.7 K, the same temperature at which the viscous penetration depth becomes equivalent to the size of the resonator.

There are however several other potential additions to the theory that could explain the extra damping visible. One potential explanation would be acoustic emission, as this is a known damping mechanism not included in the model used. Additionally acoustic effects typically become relevant at high frequencies and so may be more important for high frequency NEMS than the lower frequency devices used traditionally. The additional drag

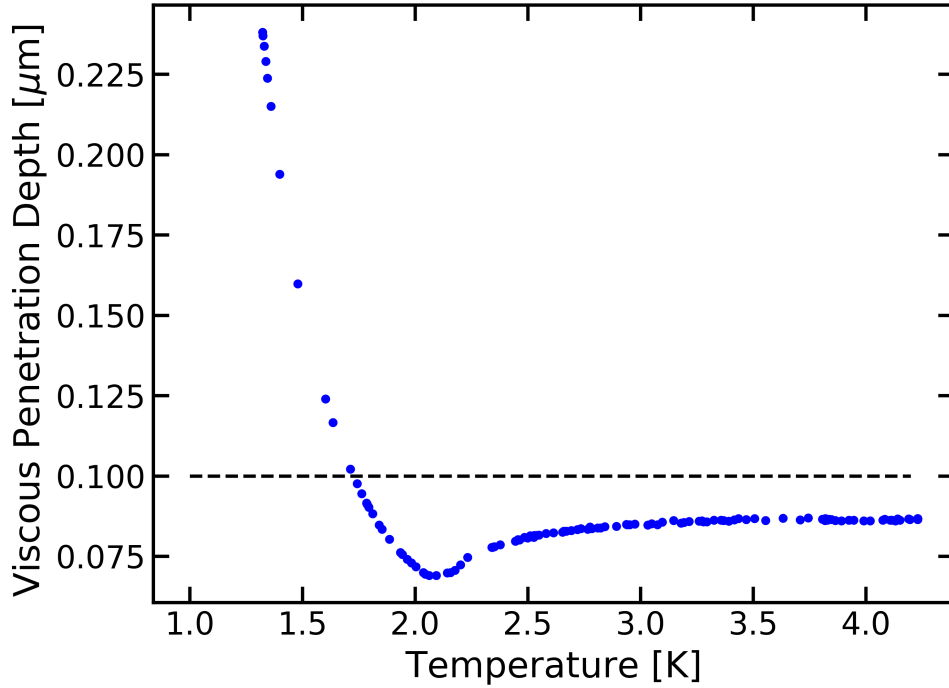


Figure 5.5: Calculated values of viscous penetration depth for the beam used as a function of temperature. The dashed line shows the width of the beam and intersects the penetration depth at a temperature of approximately 1.7 K.

measured could also be explained by the generation of vorticity, another mechanism not considered in our theory that could easily produce additional drag. Although vorticity production generally only occurs at velocities above those considered here, the novelty of performing these measurements with such small devices means there are no previous results to refer to. Unfortunately without significant further work these effects cannot be modelled, so all efforts to explain the breakdown in agreement between experiment and theory remain purely speculation. Of course, now we know the beams are pushing the limits of the theoretical model used, it is possible that the damping is still purely hydrodynamic and the model no longer applies.

To expand these results, similar measurements were also performed using other beams of

different length. Beams with length 15 μm , 25 μm , 75 μm and 100 μm were all tested. These correspond to vacuum frequencies of 8.47 MHz, 4.60 MHz, 0.972 MHz and 0.602 MHz respectively. The results obtained were very similar to those presented above for the 50 μm beam. All devices clearly showed the influence of the fluid, with dramatic changes in the resonant properties around the transition to superfluid.

Measurements of width as a function of temperature for these other beams closely match those shown in figure 5.4, with most results fitting well in the superfluid regime just below the transition temperature. Similar to the 50 μm beam, all others tested also show disagreement between experiment and hydrodynamic theory at the lowest temperatures measured. As suggested by figure 5.5, the temperatures at which the theory breaks down correlate reasonably well with those at which the penetration depth becomes larger than the beam width.

In order to allow clear comparison of the fits for a range of different devices, a new method for comparing theory and experimental results was applied. This method was based on manipulation of equation 5.2. From this equation, we see that a plot of width (Δf_2) as a function of frequency ratio $\left[\left(\frac{f_{\text{He}}}{f_0}\right)^2\right]$ would be expected to appear as a straight line with gradient equal to the constants on the right-hand side of the equation. Any disagreement between theory and experiment should then appear in this plot as a deviation from the straight line behaviour.

In practice, the entire right-hand side of equation 5.2 is calculated first. This should then collapse results for all different beams onto a common straight line dependence of gradient 1. The results of this for all 5 beams tested are shown in figure 5.6.

The results shown in figure 5.6 are largely consistent with what we would expect, although some aspects remain difficult to explain conclusively. The data for the 15 μm and 25 μm beams both fit well to the line of gradient 1 across the full range of data taken, implying that the theory works well for these two devices. With respect to the 15 μm beam this is

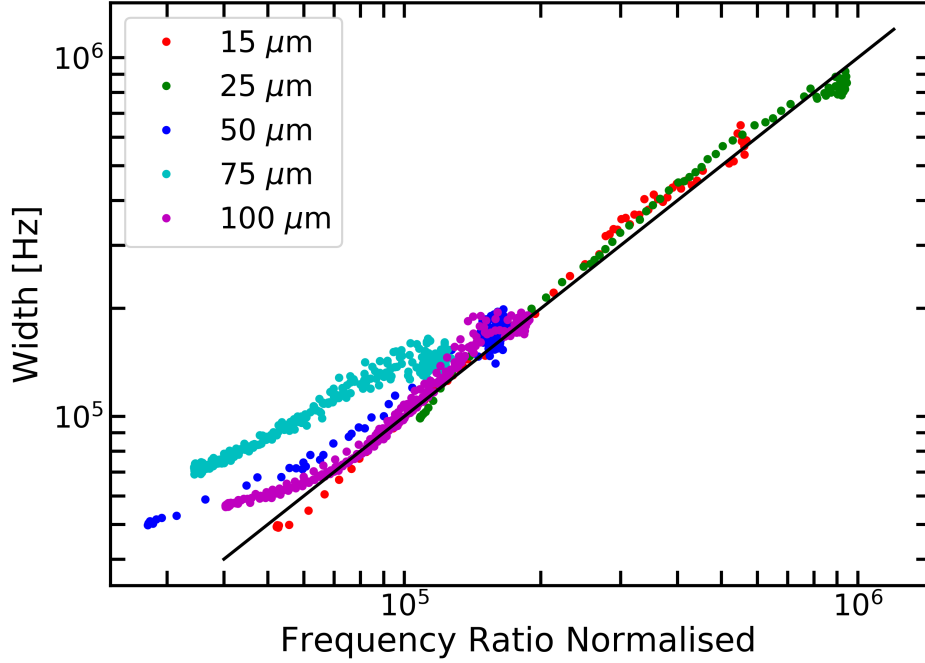


Figure 5.6: Width as a function of normalised frequency ratio for beams of different length. The black line of gradient 1 is included as a visual aid. The frequency ratio is normalised by calculating the right-hand side of equation 5.2

not quite true however, as the fit to frequency ratio for this beam fails in the normal fluid regime. This in turn highlights one drawback of the method used in figure 5.6, as only the quality of the fit to width is represented in this normalisation method. Issues with the fit to frequency ratio do not appear in figure 5.6 as C is the only geometric constant present in the normalisation. This is unlikely to be a serious issue however, as for all other devices the fit to frequency ratio appears much more reliable than the fit to width.

Figure 5.6 also appears much as expected with regards to the $50 \mu\text{m}$ and $100 \mu\text{m}$ beams. Both of these devices fit reasonably well to the theory above and just below the transition to superfluid, with the disagreement becoming most visible at low temperatures. This is what we see in figure 5.6, as results for both devices lie close to the line of gradient 1 at

large values of the width and only begin to diverge as the width falls.

The one hardest aspect of figure 5.6 to understand is the data taken for the $75\ \mu\text{m}$ beam, which does not collapse onto the dependence expected. To help with the interpretation of this result, the full plot of width as a function of temperature for this beam is shown in figure 5.7.

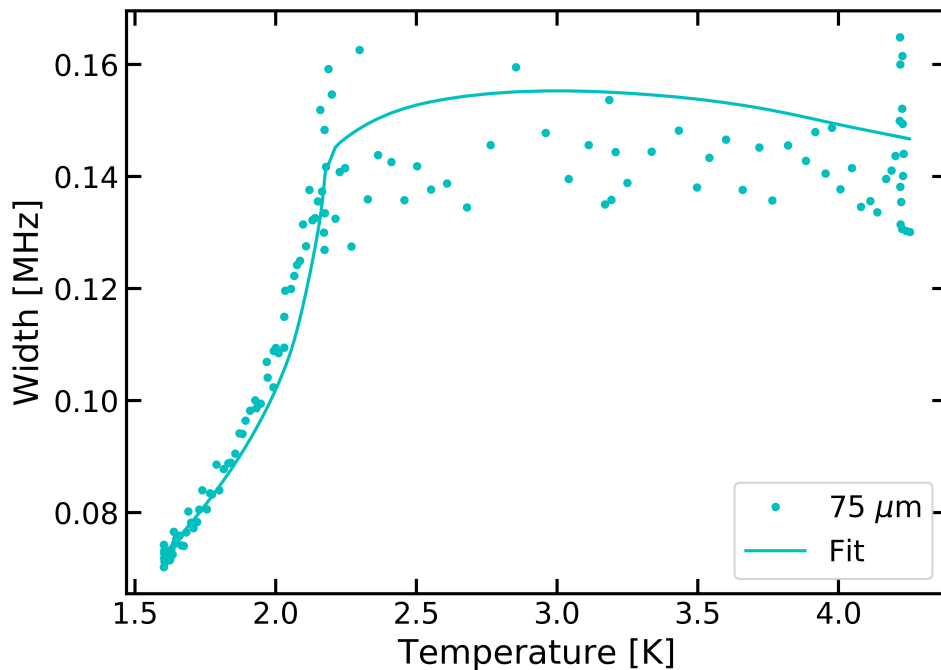


Figure 5.7: Width as a function of temperature for the $75\ \mu\text{m}$ long beam, showing the reduced quality of the hydrodynamic fit for this device.

From figure 5.7, two main differences are visible between the experimental data and the theoretical fit. The first is a fairly major disagreement between the two data sets in the normal fluid regime. This is unlikely to explain the issues seen in figure 5.6, as a similar problem is also present in the data for the $25\ \mu\text{m}$ beam without preventing these results from collapsing to the expected dependence. In practical terms, this disagreement in the normal fluid regime is likely related to the errors used when fitting. As the width can

be more accurately measured for the well defined resonances observed in the superfluid regime, these points have a lower uncertainty and are therefore given more prominence when calculating the fits.

The second issue appears in the data just below the transition to superfluid, where another disagreement between the theoretical and experimental data is clearly visible. For most other beams the points just below the superfluid transition are typically where the fit is most reliable, suggesting this is likely the reason for the incorrect scaling of the 75 μm data in figure 5.6.

The discrepancy in the 75 μm data at high widths could potentially be due to an incorrect value of C, as errors in this parameter will lead to corresponding errors in the normalisation. The incorrect gradient as width decreases cannot possibly be explained by fitting problems however and must therefore be caused by problems with the experimental results. This could potentially be due to the measurement power used as the data for the 75 μm beam was taken at a lower power than all other data, leading to less well defined resonances and therefore increased uncertainty in the calculated values of the resonant parameters.

Distinct deviations from the expected linear dependence are also visible in figure 5.6 for data taken with the 50 μm and 100 μm beams at low widths. This suggests the hydrodynamic model is less applicable to beams with low resonant frequencies. A possible explanation for this can be found by considering the viscous penetration depth. As shown in equation 5.3, the viscous penetration depth is inversely proportional to frequency and so will be larger for longer beams. Since the hydrodynamic model used is expected to break down when the viscous penetration depth becomes comparable to the beam width, we would expect the theoretical fits to be less reliable for these devices.

Overall, we can draw two main conclusions from these results. Due to the rapid changes in width seen at temperatures of approximately 2.17 K, we can be certain that the beams are

indeed probing the properties of the fluid. However, as demonstrated by the discrepancies shown in figure 5.6, we must also conclude that the damping experienced by these devices cannot be explained purely in terms of hydrodynamic drag. A more advanced model of the damping is therefore necessary to fully understand future measurements.

In addition to these measurements of the damping, efforts were also made to investigate the force-velocity characteristics of NEMS immersed in superfluid in an effort to test the possibility of turbulence generation using nanoscale oscillators. For this purpose, these measurements were performed using the 15 μm , 25 μm , 75 μm and 100 μm beams. Of these, the results taken for the 75 μm and 100 μm beams are uninteresting, remaining entirely within the linear regime.

In contrast to these trivial measurements the results obtained using the 15 μm beam show unexpected behaviour but are nearly impossible to interpret, with the non-linearity inherent in these devices complicating the results. The final set of data does however provide reasonably compelling evidence of interesting behaviour, with measurements of the 25 μm beam showing an increase in drag that could be interpreted as the generation of turbulence. The relevant force velocity plots, measured both in vacuum and in fluid at a temperature of approximately 1 K, are shown in figure 5.8.

Figure 5.8 clearly shows the expected signature of the transition to turbulence, with an increase in the drag visible above a certain critical velocity. This evidence is strengthened by the switch from one straight line dependence into another, as this implies a change in damping regime rather than an anomalous change in the drag. However, for this particular dataset there are two issues that must be resolved before the results can be considered conclusive. The first is related to the non-linearity expected in all measurements using NEMS. By comparing the f-sweep results in fluid to those taken in vacuum, we can show that the non-linearity observed in vacuum does not appear in any of the fluid measurements.

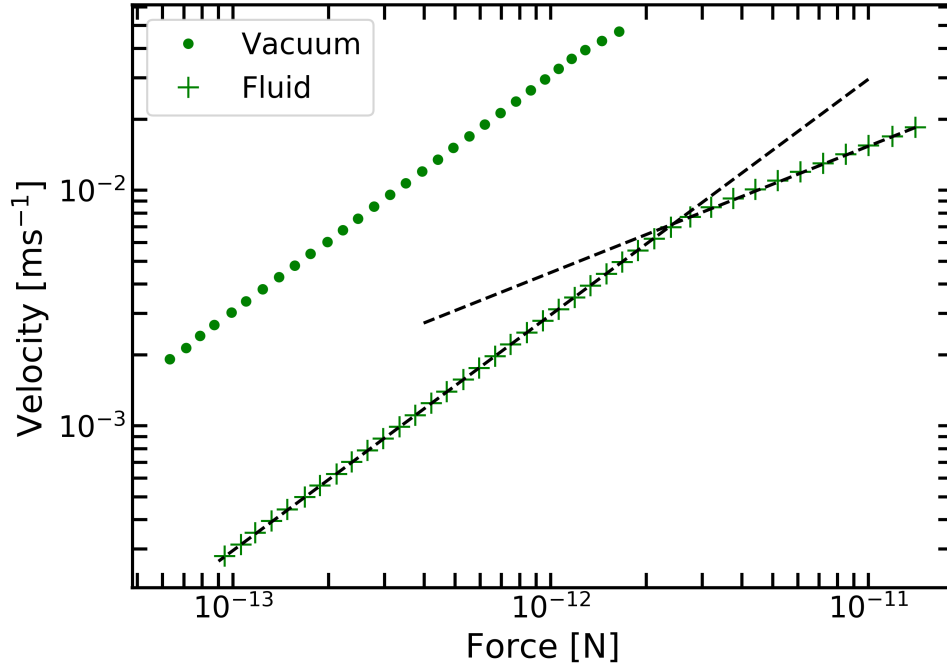


Figure 5.8: Device velocity as a function of force for the $25 \mu\text{m}$ beam, measured in both vacuum and superfluid at approximately 1 K. The dotted black lines are guides for the eye, added to emphasise the point at which the gradient changes in the fluid data.

Figure 5.9 provides additional evidence supporting the interpretation of these results as turbulence, as it shows that the non-linearity present in the vacuum results is not seen in fluid measurements. In vacuum the force-velocity results remain linear right up to the transition to the Duffing-like non-linearity shown in figure 5.9. If the change in gradient visible for the fluid results in figure 5.8 was caused by the inherent response of the beam, we would expect to see the same form of non-linearity observed in vacuum. This is not the case, with the fluid results remaining mostly linear up to the highest velocities measured. The second issue complicating the interpretation of the results in figure 5.8 is related to the fitting process used to extract values of the amplitude, width and resonant frequency from frequency sweep results. As shown in figure 5.9, the fluid data is slightly non-

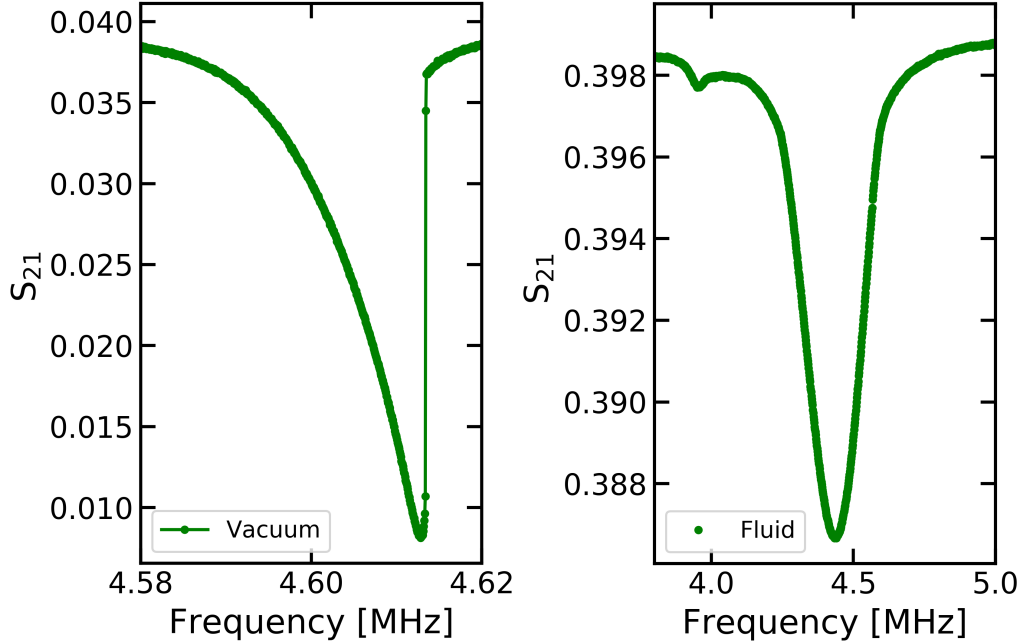


Figure 5.9: Raw frequency sweep data used to obtain the highest velocity data points included in figure 5.8. Note the difference in resonance profile, with significant non-linearity visible in the vacuum data but not seen in fluid.

linear at high velocities with a small secondary peak observed below the main resonance. This peak causes imperfections in the fitting and therefore introduces a possible error to the calculated values of the resonance properties. Due to the position of the non-linearity, this fitting problem primarily manifests as issues with accurately determining the background. This then leads to slightly overestimated values of the peak amplitude but does not significantly affect the determination of width and resonant frequency.

As described in section 3.2.4, the force and velocity are both proportional to the power lost due to resonance, which is itself dependent on the amplitude of S_{21} squared. This means errors in the value of amplitude will appear equally in velocity and force and so affect the values of both but not the relationship between them. The errors expected are therefore incapable of causing the change in gradient observed in figure 5.8, so we must

once again conclude that the generation of turbulence is the most plausible explanation.

Another point worth considering when discussing turbulence is the critical velocity at which the transition to the turbulent state occurs. Theoretical studies [73, 74] suggest that the onset velocity for turbulence in superfluid ^4He should be given by the following equation:

$$v_c = 2.6\sqrt{\kappa\omega}, \quad (5.4)$$

where κ is the circulation quantum. For the $25\ \mu\text{m}$ beam used here, the frequency of 4.6 MHz can be used to calculate an expected critical velocity of $v_c = 1.76\ \text{ms}^{-1}$. This is vastly different to the experimentally determined value, which we estimate from figure 5.8 to be approximately $7.2\ \text{mms}^{-1}$, almost three orders of magnitude smaller than the expected value. The imperfections in amplitude fitting for the fluid data could be responsible for changing the values of velocity used, but this change could not possibly be large enough to account for the full difference between prediction and measurement. It is possible that the size of the NEMS is responsible for this, as no other observations of turbulence using nanoscale oscillators are available for comparison. The theory should apply regardless of size however, so this explanation seems somewhat unlikely. As it would be premature to simply discard our observations, the most reasonable course of action would be to attempt similar measurements using other NEMS to see if the results described here can be replicated.

In terms of future directions, there are two main possibilities from here. Firstly, a better understanding of the drag force experienced by the NEMS is essential for further application of these devices in ^4He . As the physical dimension of these devices is roughly equivalent to the viscous penetration depth at the relevant temperatures, neither of the traditional simplifications used to solve similar theoretical problems are fully appropriate for this case. Therefore our best hope is to consider additional contributions to the drag,

such as that caused by acoustic emission, and investigate the combination of this and the hydrodynamic drag.

Although the discrepancies observed in figure 5.6 casts some doubt on the validity of the model used at very low temperatures, the clear change in behaviour visible at the superfluid transition temperature in figures 5.3 and 5.4 is enough to confirm that the beams used are successfully probing the properties of the helium. Since our ultimate aim is to use these devices in ^3He , a perfectly accurate model of drag in ^4He is not necessary for these goals as the theoretical background for the damping is entirely different in ^3He . Therefore, now we are confident that NEMS can be used to successfully probe liquid helium, a possible next step is to obtain a complete understanding of high frequency drag in superfluid ^3He . This should provide useful background for the long-term goal of using NEMS in ^3He .

The second avenue of investigation relates to the intriguing if inconclusive results shown in figure 5.8. Turbulence generation appears to be the most plausible explanation for the increase in drag observed experimentally, though the velocity at which the potential turbulence is observed is very different to theoretical predictions. It would therefore be very interesting to repeat the measurements using another beam of the same size. If the results can be reproduced similar experiments using beams of different length, and therefore different resonant frequencies, could provide a way of investigating how changes in frequency affect the critical velocity.

6 Frequency Dependence of Thermal Drag in $^3\text{He-B}$

To enable accurate interpretation of results obtained using an oscillating device in fluid, a detailed model of the drag force applied by the motion of the object is very important. As discussed previously in section 2.2.5, the drag experienced by oscillating structures in superfluid $^3\text{He-B}$ can be split into three distinct components as shown in equation 6.1:

$$F = F_0 + F_T + F_{\text{pb}}, \quad (6.1)$$

where F is the total drag force and F_0 , F_T and F_{pb} are the intrinsic, thermal and pair breaking components respectively.

By following the derivation described in section 2.2.5, an expression can be obtained to normalise the thermal force for an oscillating structure such that all results for a device collapse onto the same dependence. For clarity, the expected dependence is restated in equation 6.2,

$$F_r^T = \frac{(1 - \exp(-\lambda v^*))}{\lambda}. \quad (6.2)$$

This model is not valid for all oscillators however, as the derivation of this expression is strictly only true if the time for an excitation to traverse the flow field around the oscillator is much shorter than the period of the oscillations. In this case the flow field can be considered stationary with regards to the excitations and the assumption of a static flow field used in the derivation is valid [62]. Due to this, equation 6.2 is unlikely to be valid for particularly high frequency oscillators such as the nanobeams discussed in section 5. By studying other more readily accessible high frequency oscillators we can test the limits of equation 6.2 and obtain a better understanding of the thermal drag force applied to high frequency oscillators. This knowledge will hopefully prove useful on future experiments based around nanobeams in ^3He .

To make this possible, we must define the point at which the current theoretical model breaks down. By calculating rough values for the relevant time periods, we can quantify this limit and so check if the devices used satisfy this criterion. All of our experiments are performed in the low temperature, low pressure regime, where the average group velocity of an excitation is roughly equal to one third of the Fermi velocity:

$$v_g \approx \frac{v_F}{3}. \quad (6.3)$$

This can then be used to calculate an approximate value for the time taken for an excitation to traverse the flow field, t_{ex} :

$$t_{\text{ex}} \approx \frac{3L}{v_F}, \quad (6.4)$$

where L is in general terms the length of the oscillator transverse to the direction of oscillation, given by the diameter for the specific case of a vibrating wire resonator and the thickness for a tuning fork. For the derivation of equation 6.2 to remain valid this must be shorter than the time taken for the oscillations to change direction, equivalent to half the oscillator period:

$$\frac{3L}{v_F} < \frac{1}{2f_0}, \quad (6.5)$$

$$f_0 < \frac{v_F}{6L}. \quad (6.6)$$

By considering this limit, we have an easy way of checking whether equation 6.2 can be safely applied to a device. However, this limit also provides an interesting way of testing the theory. Theoretically the case where the flow field cannot be treated as stationary becomes very difficult to solve. However, the high frequency responses of tuning fork overtone modes means approaching the limit shown in equation 6.6 experimentally should be relatively straightforward. By attempting to apply equation 6.2 regardless, we can investigate how the results change for devices outside of the stationary flow regime.

To obtain data at relatively low frequency, two conventional wire resonators were used. The wires chosen for this were mmm3, with frequency 355 Hz and diameter 4.5 μm , and

Mg, with frequency 843 Hz and diameter $0.9 \mu\text{m}$. Higher frequencies were obtained using fork D2, with resonant frequency 25.4 kHz. Using the first overtone mode of the same fork, labelled D2ov1, enabled measurements at a frequency of 158 kHz.

With the devices chosen, we can use the physical dimensions to estimate the frequency required to exceed the condition stated in equation 6.6. For these calculations, an approximate value of $v_F = 60 \text{ ms}^{-1}$ will be used for the Fermi velocity. By using the diameters listed above as the physical dimension, wires Mg and mmm3 were found to have frequency limits of $f_0 \approx 11 \text{ MHz}$ and $f_0 \approx 2 \text{ MHz}$ respectively. These limits are far larger than the actual frequencies, proving that the flow can safely be considered stationary for both wires.

For the fork, the choice of physical dimension is not trivial, and can have significant implications for the results. Using the tine thickness ($90 \mu\text{m}$) gives a limiting frequency of $f_0 \approx 110 \text{ kHz}$ while the tine width ($50 \mu\text{m}$) corresponds to a limit of $f_0 \approx 200 \text{ kHz}$. In comparison to the actual frequencies of the modes we can see that the fundamental is, unsurprisingly, significantly below both possible limits. The interpretation for the overtone mode is more complex, as the frequency of this mode lies between the two calculated limits. Previously, the thickness has been used in earlier examples of similar analysis [62], so use of this value makes sense for the sake of consistency. Both possible limits are to the same order of magnitude as the actual frequency, however, which means the condition that the excitation travel time remains much shorter than the oscillation period is violated regardless. We therefore expect to see some deviation between theoretical predictions and experimental reality in the results for D2ov1.

For each of the three devices, measurements were then taken at a range of different temperatures. Experimentally, each data set was obtained using an amplitude sweep. As described in section 2.2.3, the measurements from each amplitude sweep can be used to obtain values for the drag force and the velocity of the oscillator.

Since we are interested in the effects of Andreev reflection on the drag force, only the thermal component of the force is relevant here. If a value is known for the intrinsic drag, the thermal drag force can be easily obtained by subtracting the intrinsic component from the total measured force. Fortunately, the cryostat base temperature of approximately $110 \mu\text{K}$ is low enough that the intrinsic drag can be measured experimentally. The intrinsic force-velocity characteristics for the relevant devices are shown in figure 6.1.

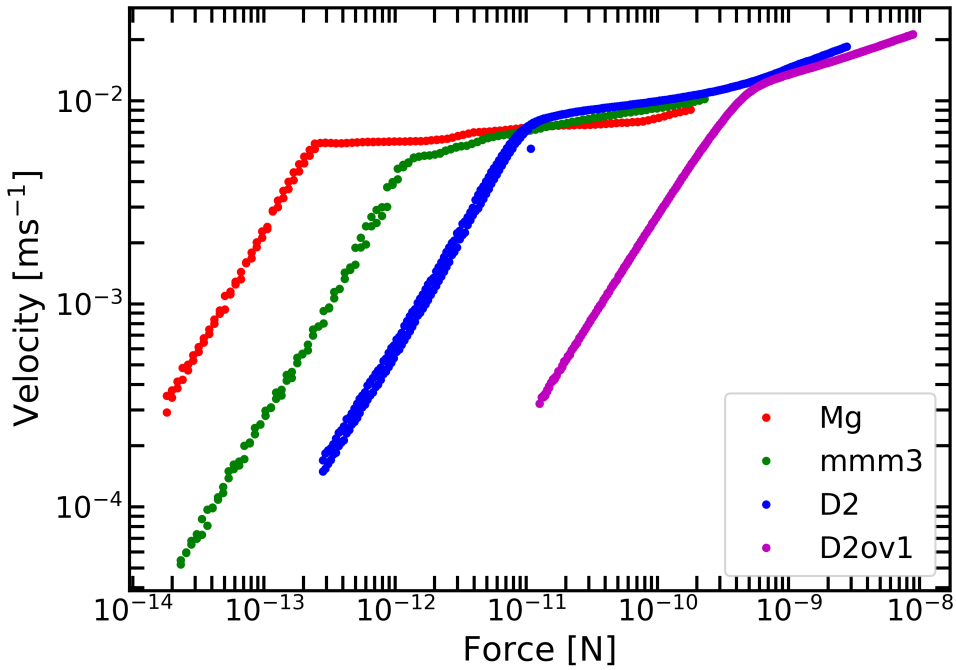


Figure 6.1: Intrinsic Force-Velocity plots for the four devices used. As all measurements shown were performed separately, the exact temperature is different for each sweep. The results for Mg, mmm3 and D2ov1 were all measured at approximately $110 \mu\text{K}$, while the data for D2 was measured at a slightly higher temperature of approximately $120 \mu\text{K}$.

At sufficiently low temperatures, the thermal contribution to the drag is negligible and so the damping should be constant up to the point at which pair-breaking effects appear. This is true of all data shown in figure 6.1, as the low velocity response matches the straight line behaviour expected. Recent results have shown that acoustic effects can become important

in $^3\text{He-B}$ at frequencies above approximately 100 kHz [75], and are therefore likely to be present in the results for D2ov1. These acoustic effects are temperature independent however, meaning we can still extract the thermal contribution to the damping of D2ov1 by subtracting the force shown in figure 6.1 from measurements at higher temperatures.

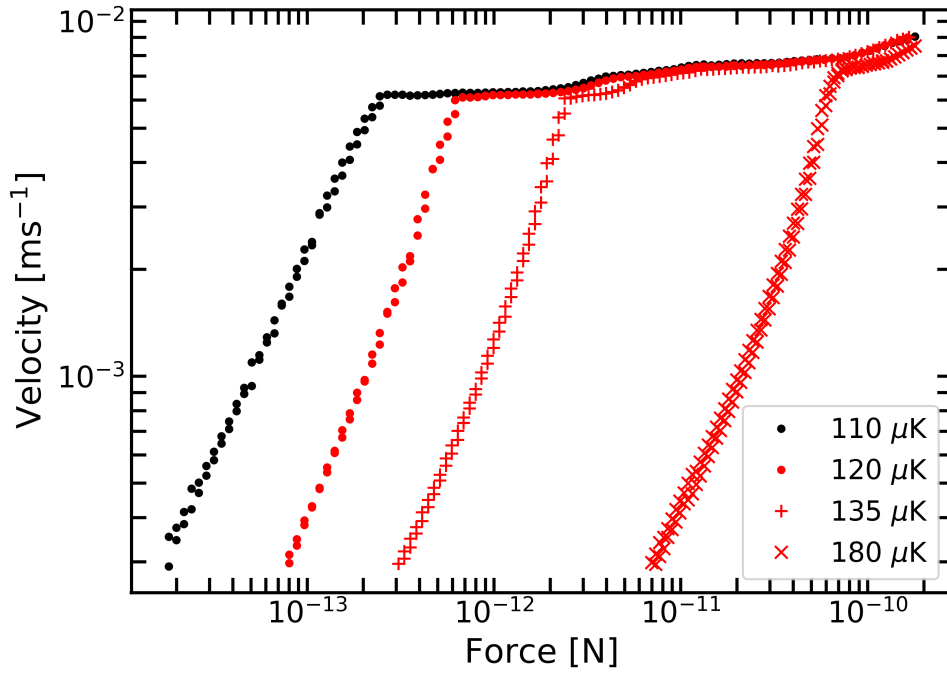


Figure 6.2: Force-Velocity plots for Mg at a range of temperatures. The points in black correspond to the intrinsic sweep shown above.

The effects of the thermal component on the overall drag is immediately apparent when comparing the intrinsic data to measurements taken at higher temperatures. As temperature increases the extra excitations present will exert an additional force on the oscillator and so the initial drag should be higher than observed for the intrinsic sweep. As velocity increases Andreev reflection becomes important, shifting the balance of excitations colliding with the oscillator and increasing the drag experienced. At higher velocities the increase in drag becomes less pronounced as the damping tends towards the maximum

possible value due to collisions with thermal excitations. Once pair-breaking occurs the drag due to thermal effects becomes negligible in comparison and so temperature changes should not change the behaviour in this region. All of these effects are confirmed by the force-velocity characteristics measured for wire Mg at a range of temperatures (figure 6.2). As shown in figure 6.1 the intrinsic drag is much larger for the tuning fork, with the overtone mode D2ov1 experiencing a drag force approximately three orders of magnitude larger than the force on Mg. The difference this larger intrinsic drag makes with regards to the overall drag can be seen by comparing figure 6.2 to a force-velocity plot of the D2ov1 data (figure 6.3).

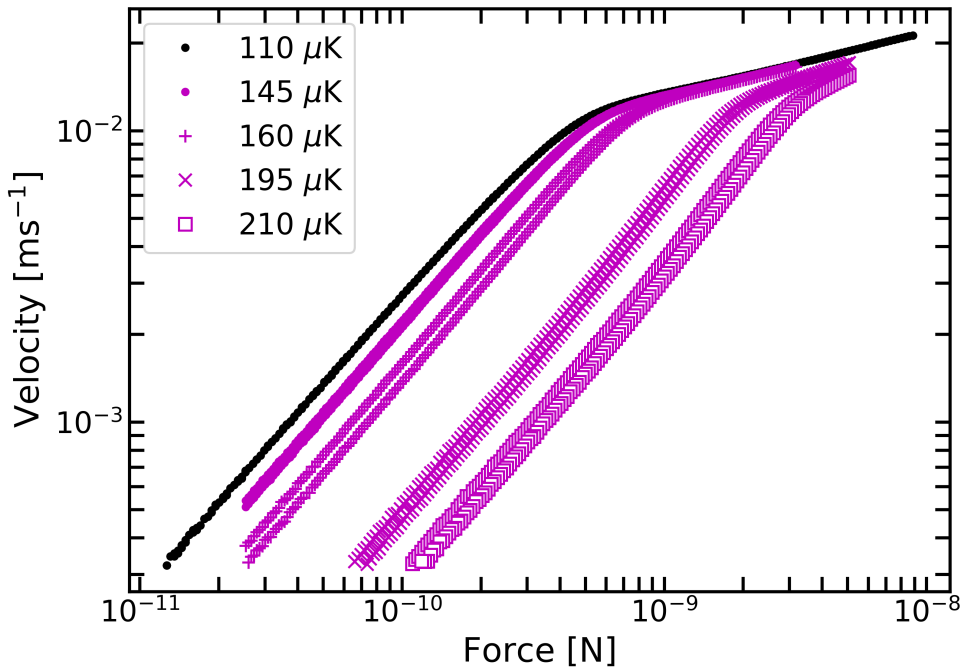


Figure 6.3: Force-Velocity plots for D2ov1 at a range of temperatures. The points in black are taken from the intrinsic sweep shown in figure 6.1.

Figure 6.3 shows that the force-velocity behaviour for D2ov1 follows the same general trend as the data for Mg, although there are significant differences. A major difference

can be seen in the thermal component of the damping. For Mg, the effects of Andreev reflection on the thermal damping are visible in all sets of data plotted, with a significant deviation from the low velocity gradient observable in the 180 μK results. For D2ov1 the influence of Andreev reflection is much subtler, with the gradient measured at 145 μK and 160 μK staying mostly constant right up to the transition to pair-breaking. The expected signature of Andreev reflection is visible in the higher temperature (195 μK and 210 μK) data, though even here the effects are much less obvious than for Mg. Despite this reduction in the importance of Andreev reflection on the overall response of D2ov1, the fact that the data for this high-frequency mode still follows the general behaviour expected suggests that the model used remains relevant beyond the predicted limits.

Another difference in the thermal damping of D2ov1 when compared to Mg can be understood by considering the relative sensitivity of the two devices. The differences in thermal sensitivity can easily be seen by considering the force-velocity plots for Mg (figure 6.2 and D2ov1 (figure 6.3). For Mg, the thermal contribution to the drag changes the total force by three orders of magnitude for a temperature change of just 70 μK . In contrast the thermal force for D2ov1 only covers two orders of magnitude for a temperature change of 100 μK .

To quantify comparisons between these results, the data must be normalised using the procedure detailed in section 2.2.3. The first step in this process is to obtain the thermal component of the force by subtracting the intrinsic behaviour from the higher temperature data. The results of this for the D2ov1 data are given in figure 6.4.

The plots of thermal force for D2ov1 demonstrate the changes expected in this component as the temperature increases. The extra drag due to additional thermal excitations at higher temperatures is shown by the increase in the gradient at low velocities. The curvature away from this initial gradient visible at higher velocities in the high temperature data shows the rate of drag increase slowing as the Andreev reflection contribution tends

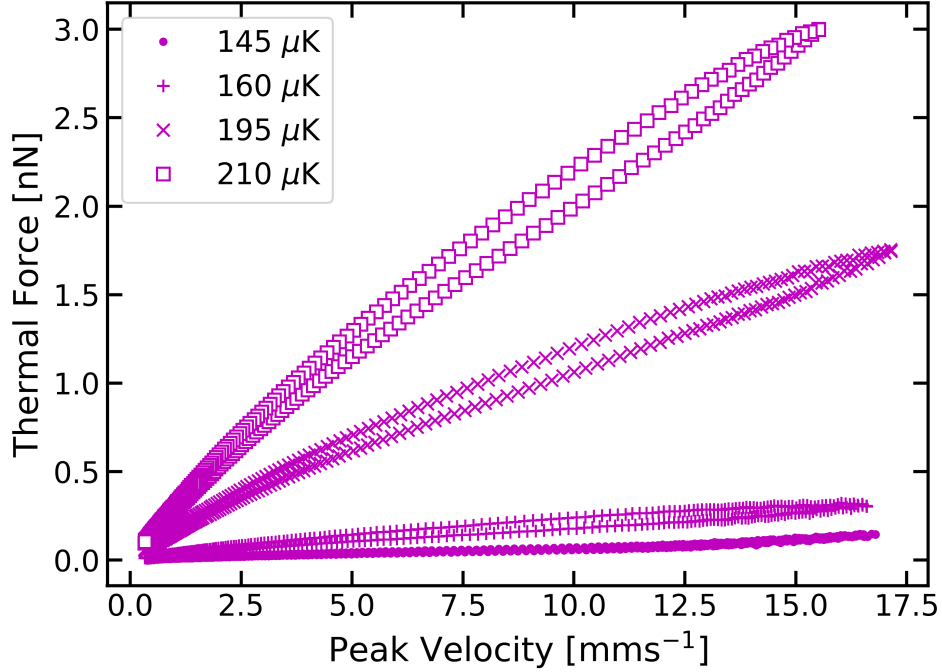


Figure 6.4: Thermal force as a function of peak velocity for D2ov1, showing data taken at a range of different temperatures.

towards its maximum value.

Unfortunately producing an equivalent plot for Mg is difficult due to the additional sensitivity of this oscillator. The vastly different scale of the thermal force for this wire means we must use a logarithmic scale for the thermal force to give equal prominence to all datasets, though this also makes the results more difficult to interpret.

Figure 6.5 shows the thermal component of the drag force as calculated for Mg. Due to the logarithmic scale used here, the expected behaviour in the absence of Andreev reflection is not represented as simply as on a linear scale and so it is not possible to visually observe the presence of the Andreev reflection effects. The increase in drag due to the increased density of excitations at higher temperature is however very easily observable by comparing the forces measured at low velocity.

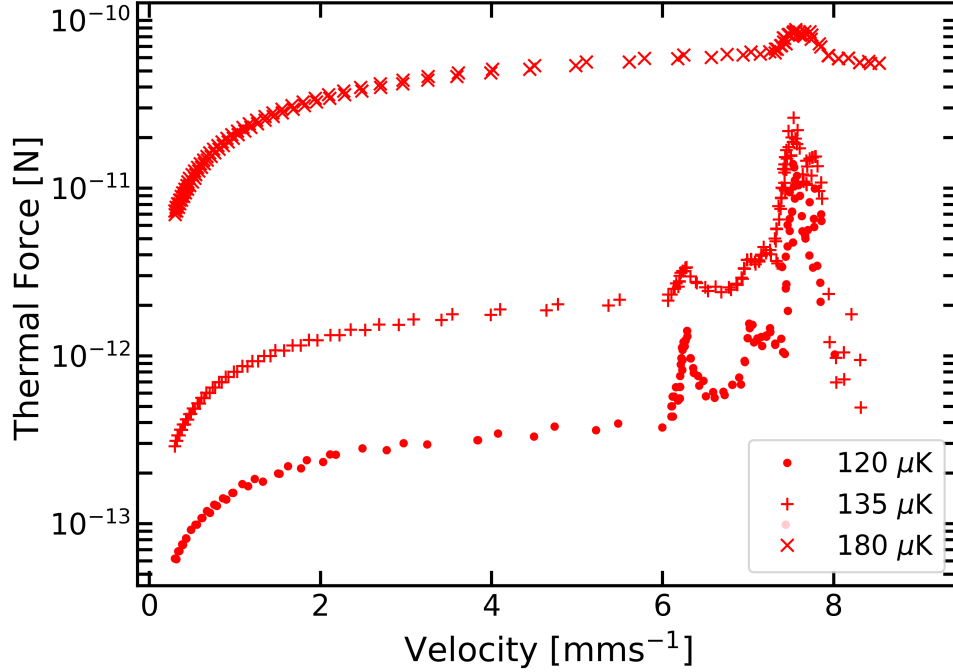


Figure 6.5: Thermal force as a function of peak velocity for Mg. The logarithmic scale for the y-axis is necessary to show all data due to the high sensitivity. Deviations from the expected behaviour above 6 mms^{-1} are due to the onset of pair-breaking, for further details see text.

One obvious feature of figure 6.5 is the major deviations from the expected trend in the first two datasets above velocities of 6 mms^{-1} . These discrepancies are artefacts of the thermal force calculation process, appearing when the intrinsic force is subtracted. Due to the exceptionally shallow gradient of the velocity-force plot (figure 6.2) in the pair-breaking regime, small differences in the exact transition velocity can correspond to large differences in the force. These large variations in the force than create the visible measurement artefacts when the intrinsic force is subtracted.

Despite this simple explanation, close inspection of the exact nature of these artefacts does lead to an interesting observation. The peaks visible in figure 6.5 above 6 mms^{-1} appear at the same velocities for all results. Even the relatively smooth results taken at $180 \mu\text{K}$

show a small peak at velocities just below 8 mms^{-1} at a location entirely consistent with the peaks seen in the much noisier lower temperature results. The reproducible nature of these features strongly implies that this is not simply a random effect but rather something that warrants closer inspection.

A closer look at the data in the pair-breaking regime of the velocity-force plots for Mg (figure 6.2) reveals the origin of this effect. The force-velocity characteristics beyond the pair-breaking transition are not smooth as would be expected. Instead, the characteristics consist of plateaus in which the velocity hardly changes interspersed with regions where the velocity increases comparatively rapidly. The regions of rapid velocity change, which we will refer to as steps for simplicity, appear to occur at the same velocity for all datasets while remaining somewhat variable in terms of force. This then clearly explains the measurement artefacts seen in figure 6.5, with the peaks corresponding to the velocities at which the steps occur. Other measurements of a similar phenomenon will be discussed in more detail in section 7.

With the thermal force known, the next step in the normalisation process involves finding the gradient of the linear plots of thermal force against velocity. Since Andreev reflection does not occur at low velocities, dividing the total thermal force by the gradient at low velocity removes the dependence on the excitation density and leaves just the effects of Andreev reflection. Plotting this against the reduced velocity $v^* = \frac{p_F v}{k_B T}$ should remove all temperature dependence and so collapse measurements from a wide range of temperatures to a single dependence. The results of this for D2ov1 are shown in figure 6.6.

As derived in section 2.2.3 results for any temperature should be described by equation 6.2, where F_r^T is the normalised force and v^* is the normalised velocity. Although some spread is still visible in the data, the agreement between the data sets in figure 6.6 proves that the normalisation works as intended.

For D2ov1, however, this is a surprising result. As the frequency of this device is outside

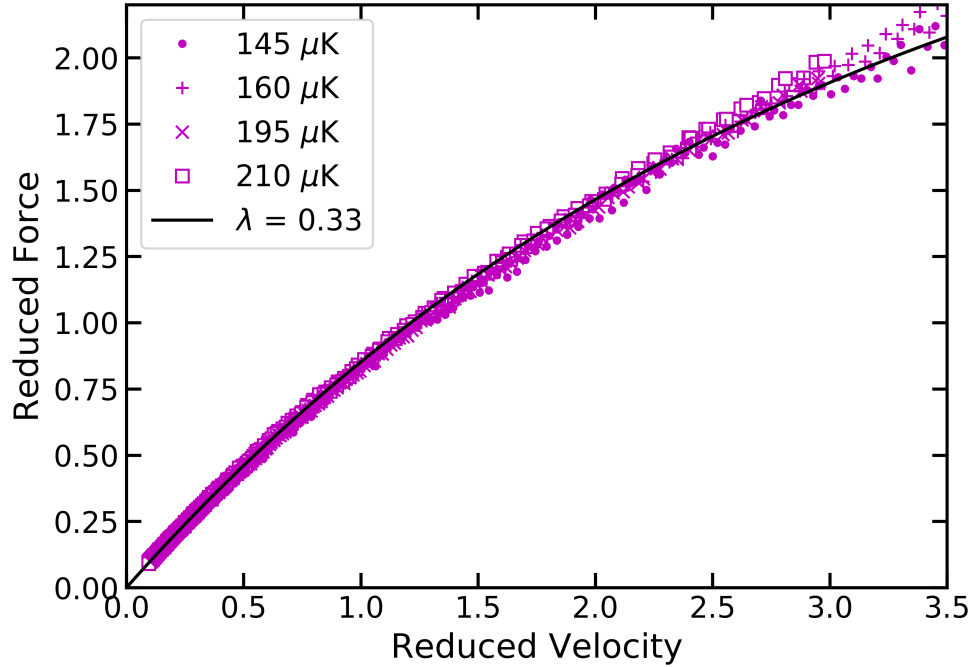


Figure 6.6: Reduced Force-Velocity plot for D2ov1, showing the range of temperatures investigated. The black line is a fit to equation 6.2, with λ treated as a fitting parameter.

the limit defined by equation 6.6, equation 6.2 should no longer be valid for this device. The value of λ calculated for D2ov1 is significantly smaller than any values measured in previous experiments. At low values of lambda the significance of Andreev reflection on the overall response of the device reduces. This implies that crossing the frequency limit (equation 6.6) reduces the importance of the Andreev reflection contribution without breaking the form of the model. More data from different devices would be necessary to confirm this however. Another alternative, also consistent with the results, is that the model becomes steadily less applicable beyond the limit rather than breaking down dramatically.

However, the fit to the D2ov1 data shown in figure 6.6 is not perfect, with the fit values slightly larger than the measured at low reduced velocities and slightly smaller at high

reduced velocities. This effect becomes even more pronounced if the measurements are extended to higher values of reduced velocity. Results at higher values of reduced velocity are however close to the transition to pair-breaking, so the problems with the fit could alternatively be attributed to effects due to pair-breaking. As shown in figure 6.3 the transition to pair-breaking for D2ov1 is rather smooth, making it difficult to locate the exact point at which the change of regime takes place and therefore difficult to determine exactly where the reduced velocity data should be cut.

With the effectiveness of equation 6.2 confirmed by figure 6.6, the same normalisation procedure can now be applied to measurements taken with the other devices. To make the differences between the two devices as clear as possible, data from all these devices are shown on the same axes in figure 6.7.

Figure 6.7 clearly proves the validity of equation 6.2, as data for all four different devices can be collapsed successfully onto a device specific dependence matching equation 6.2. The four data sets fit the trend suggested by the D2ov1 results, with smaller values of λ observed for the higher frequency oscillators.

The values of λ obtained here are roughly consistent with past measurements, with a previous experiment obtaining $\lambda = 0.69$ for a $4.5 \mu\text{m}$ diameter vibrating wire resonator (labelled mmm7) and $\lambda = 0.45$ for a quartz tuning fork (referred to as F1 here) [62]. The wire resonator mmm7 had a diameter of $4.5 \mu\text{m}$, the same as wire mmm3 used here, and a resonance frequency of 740 Hz. Fork F1 however was significantly larger than D2, with tine width $100 \mu\text{m}$ and thickness $220 \mu\text{m}$. The tine length of 2.3 mm gave F1 a resonance frequency of 32.3 kHz.

To better demonstrate the trend deduced from figure 6.7, figure 6.8 shows the relationship between λ and frequency. Before plotting, the frequency was normalised using the dimension of the device and the excitation group velocity. The equation used for this normalisation was obtained by rearranging equation 6.6:

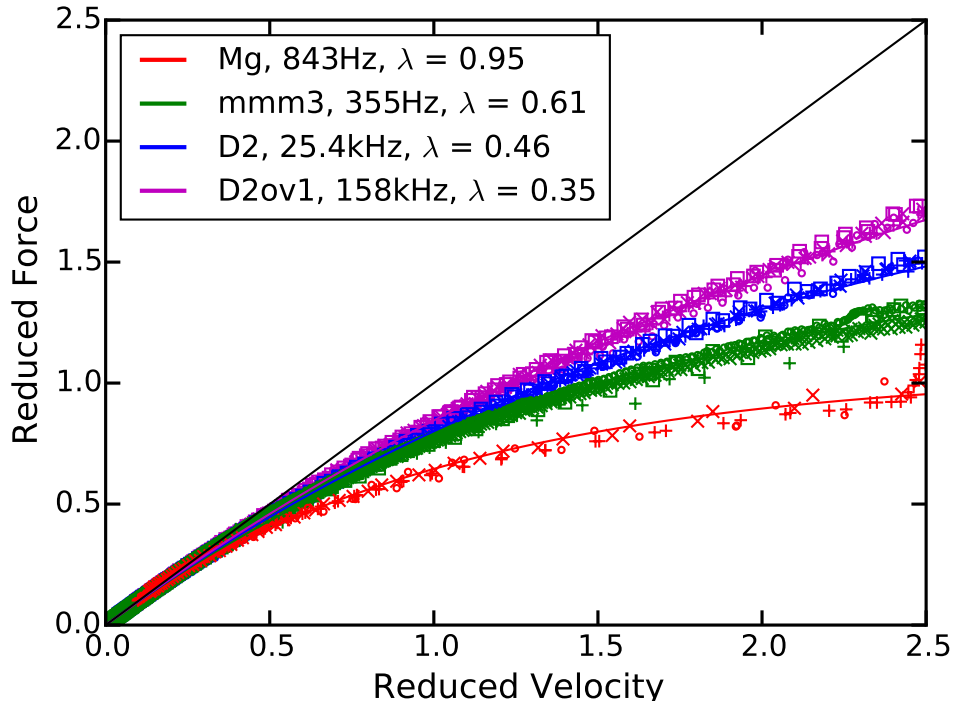


Figure 6.7: Combined plot of reduced Force-Velocity data taken for all 4 devices. Values of the constant lambda are obtained by fitting the data to equation 6.2. The black line of gradient 1 shows the behaviour expected without Andreev reflection.

$$\frac{6f_0L}{v_F} < 1. \quad (6.7)$$

Plotting lambda as a function of $\frac{6f_0L}{v_F}$ therefore shows how lambda changes as the limit is approached, the results of which give strong evidence of the reduced importance of Andreev reflection in high frequency motion. Devices close to the high frequency limit clearly show reduced prominence in the effects of Andreev reflection, represented by the smaller values of lambda.

Less encouragingly there is a very significant amount of spread visible in figure 6.8, which strongly implies the tendency towards lower values of lambda close to the limit is a rough

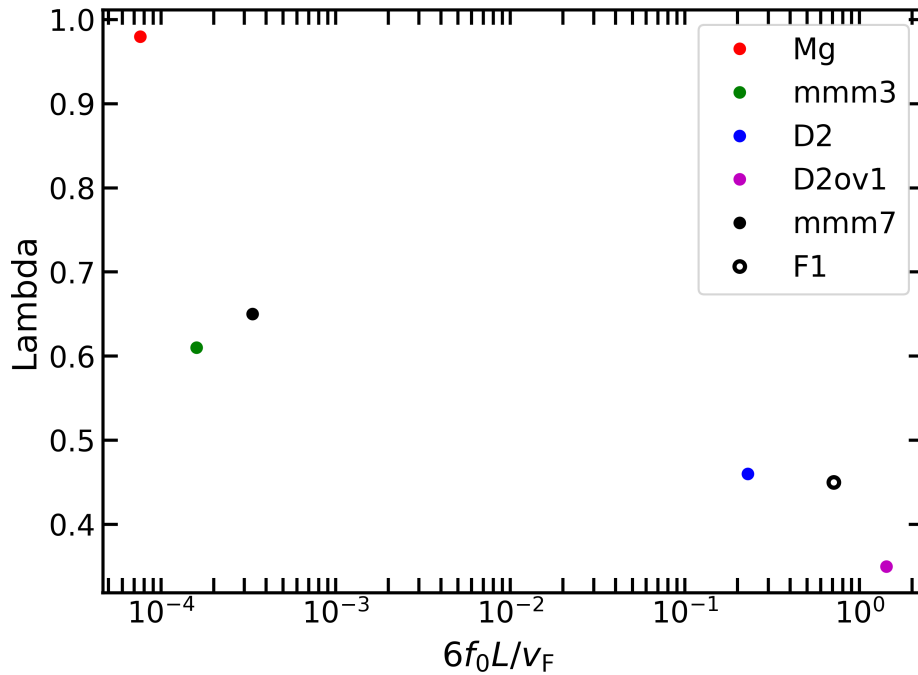


Figure 6.8: Lambda as a function of normalised frequency for a range of devices. For full details of the normalisation applied see text. Results for mmm7 and F1 are taken from Bradley et al [62].

trend rather than a strong dependence. Since the limiting condition depends on both frequency and dimension, careful choice of both parameters could enable more rigorous tests of the trend observed by enhancing the range of parameters accessible. As an example, using the second overtone of a tuning fork would increase the frequency without changing the device size and so allow us to vastly exceed the limit. Unfortunately we were not able to obtain a response sufficient for measurements on this mode for any of the forks in the cell. This suggests any fork intended for this purpose would require adjustments to the pattern of the fork electrodes to optimise response for the overtone mode.

It is also worth applying this limit to predict how a nanomechanical oscillator might behave in ^3He . Considering the nanomechanical oscillators discussed in section 5, we use the beam

width (100 nm) as the physical dimension. In terms of frequency, these resonators ranged from ≈ 0.6 MHz to ≈ 8.5 MHz based on the length of the beam. Applying these values gives $\frac{6f_0L}{v_F} = 6 \times 10^{-3}$ for $f_0 = 0.6$ MHz and $\frac{6f_0L}{v_F} = 8.5 \times 10^{-2}$ for $f_0 = 8.5$ MHz. Both of these results are significantly below 1, implying nanomechanical resonators of this type should also follow equation 6.2. Additionally, this would also place results obtained using these objects around the untested range in the middle of figure 6.8, providing an intriguing extension of the result discussed here.

7 Anomalous Damping of a Wire Resonator in Superfluid $^3\text{He-B}$

7.1 Expected Damping in Superfluid $^3\text{He-B}$

As described in section 2.2.3, the damping on an oscillating object in superfluid $^3\text{He-B}$ can be split into three distinct components. Typical measurements of this damping, such as those shown in figure 7.1, are described very well by this model.

The three different components of the total damping force are all visible in figure 7.1. The most basic contribution, present at all possible parameters, is the intrinsic component. Due to its small magnitude, this component is typically overwhelmed by the others at all but the lowest temperatures. As temperature increases additional thermal excitations are added to the system, introducing a thermal contribution to the damping. Andreev reflection due to the motion of the object then alters the proportion of particles and holes incident on the object and therefore increases the drag (see section 2.2.5 for a detailed description of this mechanism). This thermal drag is linear with velocity for small values of velocity, tending towards a fixed maxima set by the excitation density at larger velocities. As velocity increases further pair-breaking becomes possible, the large amount of energy lost due to this process leading to a vast increase in the drag force.

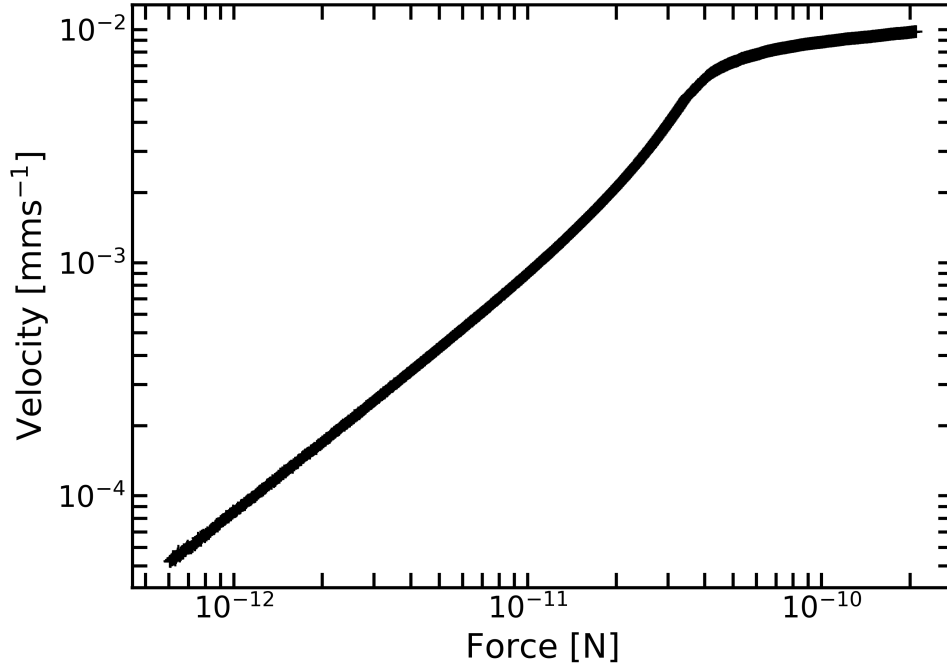


Figure 7.1: Force-Velocity plot for mmm3, a $4.5 \mu\text{m}$ diameter vibrating wire with resonant frequency 355 Hz, at a temperature of approximately $150 \mu\text{K}$. For a full description of how the different contributions to the total drag manifest in the results, see text.

7.2 Observed Deviations from Expected Damping

For the majority of the devices tested, the observed damping matches the expected behaviour very well. One of the vibrating wires tested did not match the predictions however, with unexpected plateaus appearing in the force-velocity characteristics of a $4.5 \mu\text{m}$ diameter wire resonator of resonant frequency 460 Hz we refer to as mmm1. It is important to note that there is nothing special about this wire, and we would therefore naively expect it to provide more or less identical results to other wires of the same thickness.

Figure 7.2 shows the response of wire mmm1, with two major plateaus clearly visible at velocities of approximately 2 mms^{-1} and 4 mms^{-1} . In physical terms, these plateaus mean the force applied is increasing without any associated increase in the velocity and therefore

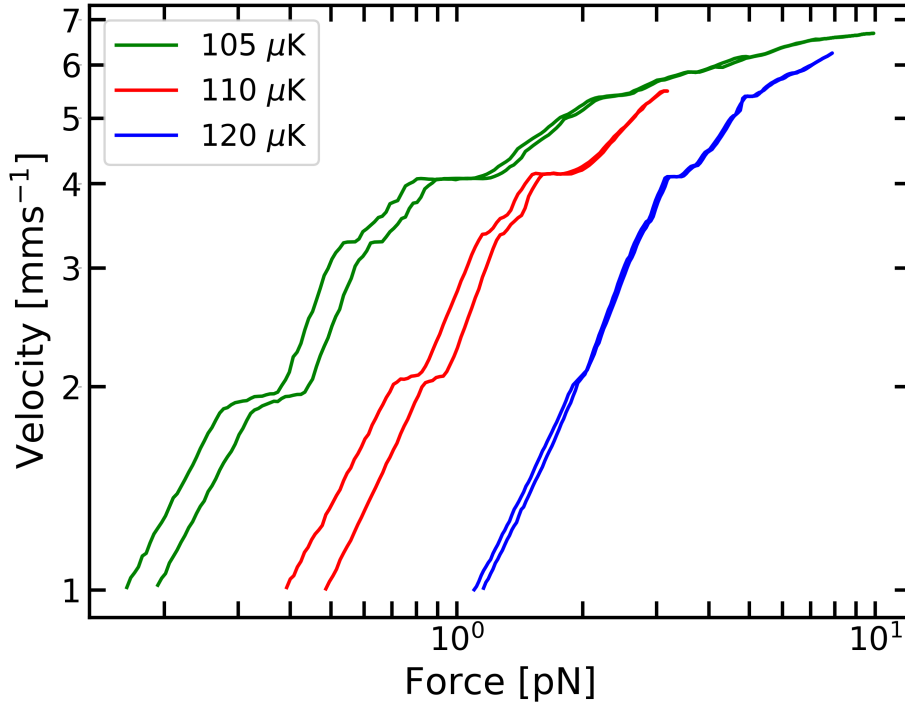


Figure 7.2: Force-Velocity plot for vibrating wire mmm1, showing multiple unexpected plateaus. Each measurement shown was taken during a different demag, showing that the plateaus remain present.

must correspond to vastly increased damping. As the velocities involved fall well below the transition to pair-breaking, these measurements cannot be explained by the current theory.

In an effort to minimise noise in these results the measurements were performed slowly, with a total of 1000 points per sweep. A typical measurement would therefore take roughly 4 hours to measure 2000 points, one sweep with increasing drive and another as the drive is decreased back down.

In comparisons between the three different temperatures tested, figure 7.2 suggests the size of the plateaus is temperature dependent. A slight temperature dependence is definitely

present, with the length of the plateaus reducing at higher temperature, though this effect is heavily exaggerated by the logarithmic scale used in figure 7.2. The strength of the temperature dependence also seems different for the two major plateaus observed, with the feature at 2 mms^{-1} appearing much more heavily temperature dependent than that at 4 mms^{-1} . This potentially suggests a different mechanism is responsible for the two plateaus, though interpretation is difficult.

A detailed study of figure 7.2 also reveals further intriguing details. In addition to the large plateaus, there are two smaller deviations from the smooth behaviour expected at velocities of approximately 3.4 and 3.6 mms^{-1} . Also of note are changes in the gradient around the first plateau, with the gradient becoming noticeably steeper after the plateau. These results can therefore only be explained by a mechanism that can explain both the massive increase in damping and the subsequent reduction. Similar analysis of the gradient around the second plateau is unfortunately complicated by its proximity to the pair-breaking regime. As shown by figure 7.1 the transition to pair-breaking can be relatively smooth for some vibrating wires, particularly at higher temperatures. It is therefore difficult to separate gradient changes due to the pair-breaking transition from potential gradient changes associated with the plateau.

Another feature worth discussing in this plot is the obvious hysteresis, with clear differences between increasing and decreasing drive measurements. To emphasise the plateaus, these measurements were taken slowly to allow 1000 points per sweep. Due to this the sweeps take a long time, creating a significant temperature difference between the start and end of the measurements. For the data shown in figure 7.2, the measurements were started at $109 \mu\text{K}$ and finished at $114 \mu\text{K}$. The excitation density is therefore higher at the end of the measurements, leading to increased thermal damping and giving rise to the hysteresis. In an attempt to find a more reliable way of identifying the location of the deviations from the linear behaviour seen in figure 7.2, the derivative of force with respect to velocity was

calculated and plotted as a function of velocity. The plot of this derivative for the data discussed above is shown in figure 7.3.

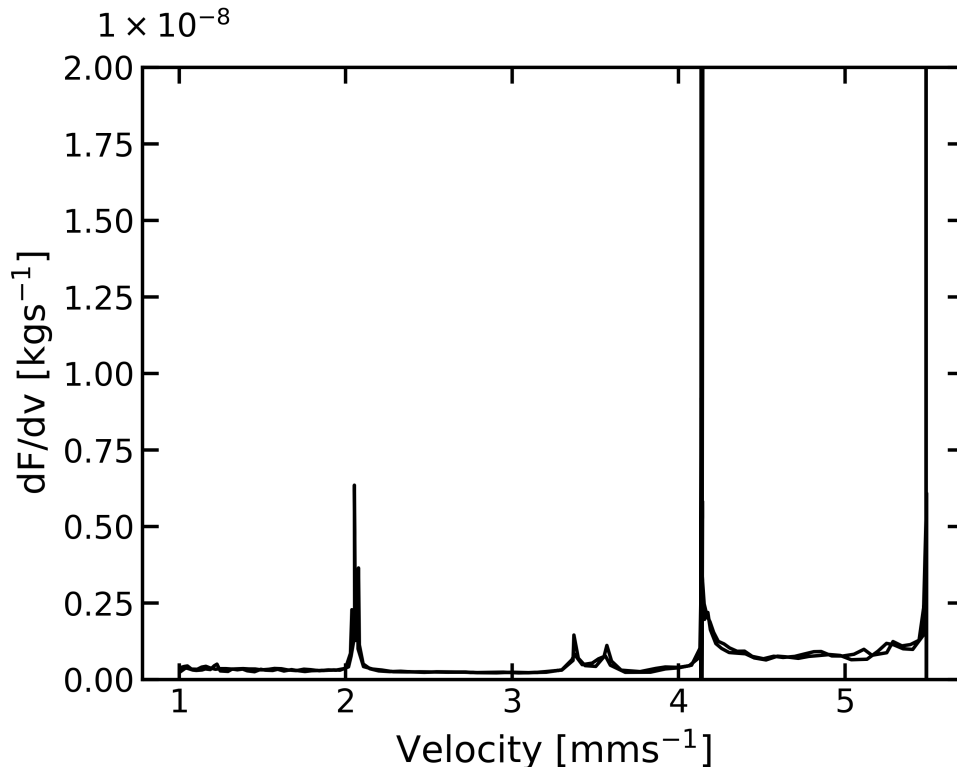


Figure 7.3: Plot of the derivative of force with respect to velocity, calculated from the force-velocity characteristics of the $110 \mu\text{K}$ data shown in figure 7.2. The large spikes are caused by rapid changes in the gradient of the force-velocity plot and should therefore correspond to the observed plateaus.

As Figure 7.3 demonstrates, the derivative of force with respect to velocity is useful for identifying plateaus in the force-velocity characteristics as the changes in gradient around these features are clearly represented as spikes in the derivative. The five main spikes seen in figure 7.3, at 2.1 mms^{-1} , 3.4 mms^{-1} , 3.6 mms^{-1} , 4.1 mms^{-1} and 5.5 mms^{-1} can all be related to features visible in figure 7.2.

Another interesting observation can be made by considering the relative sizes of the spikes. Due to the nature of the derivative, a larger spike relates to a sharper change in the gradient

of the force-velocity plot. By comparing figure 7.2 and figure 7.3, the differences in peak size are clearly reflected in the force-velocity plot. On the most basic level, this is shown in the 3.4 mms^{-1} and 3.6 mms^{-1} features, as there are much smaller than any of the others. Unfortunately, with no theoretical explanation to turn to the meaning of these differences is currently unclear.

To reduce the contribution of noise to the overall results, each point used in the calculation of the derivative was obtained by averaging over the nearest 5 points in the raw data. Due to the large size of the raw data sets, this process could be applied without sacrificing definition in the final results. We can therefore feel confident that all significant features visible in the derivative plots correspond to a relevant feature in the force-velocity plots.

Comparisons between the different sets of results in figure 7.2 show major similarities. The plateaus observed are present in all the measurements, despite the fact each was taken during a different demag. These features are therefore reproducible, which strongly suggests that these observations must have some physical explanation.

7.3 Potential Physical Explanations

When contemplating possible explanations for the anomalous damping observed, we must consider the physical meaning of the force-velocity characteristics obtained to ensure the theory provided can sufficiently explain what is seen. At the plateaus additional force is applied to the wire without a corresponding increase in velocity, meaning that energy provided to the system through the increase in force is being converted to a form we cannot measure using the techniques applied. Therefore, applying conservation of energy to this, any mechanism used to explain the results seen must be able to account for this excess energy.

The most obvious way to explain these observations is to assume that this excess energy is lost into the system in the form of vorticity. One benefit of this approach is that it can

potentially explain why only one of the 4.5 μm diameter wires tested shows this behaviour. Experiments in ^4He have shown that vortex generation depends heavily on small lengths of vortex line that are always present in the system [73]. These remanent vortices persist by attaching to boundaries [29], implying that the properties of an object surface can alter the number of attached vortices and hence affect the generation of turbulence. If we assume the same remains true in ^3He , it follows that differences in the microscopic structure between two wires could allow only one to readily produce vorticity.

To test this possibility, we can calculate the total length of vortex line required to account for the lost energy due to one of the plateaus. Using the expression for power in terms of force and velocity ($P = Fv$) we can estimate the change in power across a plateau, $\Delta P = v\Delta F$, where ΔF is the change in force across the plateau. By applying the definition of power ($E = Pt$) the time taken to traverse the plateau can be used to estimate the energy lost, $\Delta E = \Delta Pt = v\Delta Ft$

As a test, this can then be applied to the plateau observed at 4 mms^{-1} in the 110 μK data from figure 7.2. Using this calculation, we find that the total energy converted to vorticity in the 250 seconds it takes to traverse the plateau is approximately 0.39 pJ.

As shown in section 2.1.2, an equation for the energy of a vortex line can be derived. For clarity, this expression is restated below:

$$\frac{E}{l} = \frac{\rho_S \kappa^2}{4\pi} \ln \left(\frac{b}{\xi} \right), \quad (7.1)$$

where ξ is the superfluid coherence length. Rearranging this to find the length of vortex line:

$$l = \frac{4\pi E}{\rho_S \kappa^2 \ln \left(\frac{b}{\xi} \right)}. \quad (7.2)$$

These measurements were performed at 110 μK and 0 bar pressure. These parameters can be used to obtain the values of ρ_S , κ and ξ . For the characteristic length scale, b , there are two options available, with both the wire diameter (4.5 μm) and the typical spacing between vortices ($\approx 100 \mu\text{m}$ [76]) plausible choices. Using equation 7.2 to estimate the total length of vortex line produced for both possible choices of the characteristic length scale, $b = 4.5 \mu\text{m}$ gives $l = 1.61 \text{ Mm}$, while $b = 100 \mu\text{m}$ gives $l = 0.914 \text{ Mm}$.

This will be an overestimate however, as this approach only considers the energy of the superfluid component. In reality there will also be an energy associated with the normal fluid core of the vortex that must also be accounted for. This core energy can be estimated by applying Fermi liquid theory to this region at an effective temperature of the superfluid critical temperature, $T_c = 929 \mu\text{K}$ at 0 bar pressure. To calculate the energy we must first obtain expressions for the volume of the vortex core and the number of normal fluid excitations present. The volume of the vortex core V_c can easily be found by treating the core as a cylinder with length l and radius equal to the coherence length:

$$V_c = \pi\xi^2l. \quad (7.3)$$

The number of excitations can be estimated using Fermi liquid theory. An expression for the number of excitations in terms of the Fermi momentum can be obtained by rearranging equation 2.31:

$$N = \frac{Vp_F^3}{3\pi^2\hbar^3}. \quad (7.4)$$

The final thing necessary is the energy of each of these excitations. The energy of a single excitation can be calculated using the temperature:

$$E_P = 1.76k_B T_c + k_B T. \quad (7.5)$$

The energy of the excitations considered here can be estimated by assuming the temperature is equal to the critical temperature of the superfluid:

$$E_P = 2.76k_B T_c. \quad (7.6)$$

The total energy associated with the vortex core is given by the number of excitations multiplied by the energy of each, $E = N E_P$. An expression for the energy per unit vortex line length can now be obtained by combining equations 7.3, 7.4 and 7.6:

$$\frac{E}{l} = \frac{0.92k_B T_c \xi^2 p_F^3}{\pi \hbar^3}. \quad (7.7)$$

The total energy of the vortex line is then given by adding the contribution of the superfluid (7.1) to that of the normal fluid core (7.7):

$$\frac{E}{l} = \frac{\rho_S \kappa^2}{4\pi} \ln\left(\frac{b}{\xi}\right) + \frac{0.92k_B T_c \xi^2 p_F^3}{\pi \hbar^3}. \quad (7.8)$$

Applying equation 7.8, we find that a total line length of $l = 3.59$ cm is necessary to account for the the 0.39 pJ of energy lost during the plateau. This result is vastly different to the $l = 1.61$ Mm result calculated from just the superfluid component, showing that the energy in the vortex core is many orders of magnitude larger than the superfluid contribution.

By considering the frequency of the oscillator, the amount of vortex line produced during a single cycle can also be estimated by dividing the total line length by the number of cycles. Multiplying the time taken to cross the plateau and the frequency of the oscillator then gives the number of oscillations completed during this time.

Using 441.7 Hz as the frequency of the resonator we find that 1.1×10^5 complete oscillations occur while traversing the plateau considered here. By applying this we find that approximately 0.33 μm of vortex line would need to be produced per oscillation to account

for the energy discrepancy measured.

To provide further context for this result we can also estimate the expected size of vortex ring produced by the resonator used. The typical vortex ring production mechanism is known to be most efficient if the frequency of the oscillations is the same as the Kelvin wave resonance frequency of the vortex produced. The resonant frequency of the Kelvin wave on a vortex ring can be estimated by using the equation below [1]:

$$\omega = \frac{\kappa k^2}{4\pi} \ln \left(\frac{1}{k\xi} \right), \quad (7.9)$$

where k is the wavenumber of a vortex ring of length a , $k = \frac{1}{a}$. Solving equation 7.9 numerically, we find that vortex production is most efficient for rings of length $a \approx 7 \mu\text{m}$ for the 442 Hz wire used here.

The results obtained can now be combined to estimate the number of vortex rings produced per cycle by dividing the line length per cycle by the typical vortex size. Using the numbers calculated above, we therefore find that 4.7×10^{-2} vortex rings would need to be produced per cycle to explain the energy loss measured. This roughly corresponds to the production of 1 ring every 21 cycles, or alternatively 21 rings per second. The fact that rings are not produced every cycle appears to imply that we would expect the drag to increase only for the oscillations which produce a ring. However the rate of ring production is significantly larger than the rate at which measurements are taken, meaning many rings are emitted between each recording and any discrete behaviour will be obscured by this.

Overall this result seems fairly plausible, with a believable amount of vorticity produced. However, for completeness, we will also consider the possibility of excitation emission as a potential explanation for the observed behaviour. To test the validity of this hypothesis we first calculate the typical energy of an excitation at the temperature considered here by applying equation 7.5. Deciding on the value of temperature to use for T is not trivial, as although the temperature of the experimental volume is known the excitations will exist

at some undetermined higher temperature. In practice this choice is not hugely important, as the temperatures involved are much smaller than the critical temperature and so the result will be dominated by the first term. Using an estimated value of $T = 200 \mu\text{K}$, the quasiparticle energy is found to be $E_P = 2.46 \times 10^{-26} \text{ J}$.

Dividing the total energy lost across the plateau (calculated previously to be $E = 0.39 \text{ pJ}$) by the energy of a single quasiparticle shows that approximately $N = 1.59 \times 10^{13}$ quasiparticles must be produced in total to account for this lost energy. Using 250 s as the time taken, this is found to correspond to roughly 6.34×10^{10} quasiparticles created per second.

Since it is difficult to get an intuitive grasp on the plausibility of this result, we can test it by calculating the thermal quasiparticle number at the temperature of these measurements and comparing the two values. The thermal quasiparticle number can be obtained from the quasiparticle flux. An equation for the quasiparticle flux, derived in section 2.2.5, will be restated here for clarity:

$$\langle nv_g \rangle = g(p_F) k_B T \exp\left(-\frac{\Delta}{k_B T}\right), \quad (7.10)$$

where $\langle nv_g \rangle$ is the quasiparticle flux and $g(p_F)$ is the density of states in momentum space. An equation for $g(p_F)$ can then be obtained by applying Fermi liquid theory:

$$g(p_F) = \frac{m_3^* V p_F}{\pi^2 \hbar^3}, \quad (7.11)$$

where m_3^* is the effective mass of the helium and V is the volume of the cell. Combining equations 7.10 and 7.11, we obtain a value of $\langle nv_g \rangle = 1.07 \times 10^{11} \text{ m}^{-2} \text{ s}^{-1}$ for the quasiparticle flux. Dividing this by the group velocity $v_g = 15.3 \text{ ms}^{-1}$ gives a thermal excitation density of $5.63 \times 10^{10} \text{ m}^{-3}$ at a temperature of $110 \mu\text{K}$.

Comparing these two results, we see that the number of excitations produced per second

is very similar to the total number of thermal excitations present at the temperature of these measurements. A naive reading of this result would suggest that we should therefore expect a large temperature increase due to the plateau, which is not seen in practice. A more detailed interpretation is difficult however, as the change in the thermal excitation number depends on the balance of the heat produced by background heat leaks and the heat removed as excitations are absorbed by the copper surrounding the cell. Since we cannot accurately quantify either of these effects, detailed calculations of the exact heat balance are not possible.

Though both proposed solutions are possible, we speculate that vortex emission appears more likely. The interpretation of this possibility is largely complete, returning a reasonable value for the amount of vorticity produced with minimal assumptions required. Although the values calculated for excitation production give roughly the correct order of magnitude, more detailed analysis is impossible without a full understanding of the heat balance within the cell. Without this the analysis remains incomplete and we cannot say for certain that excitation creation can adequately explain the energy loss observed. In addition to this, it is more difficult to theoretically justify the emission of excitations below the transition to pair-breaking.

In terms of future experiments, there are few obvious ways to extract further useful information from the devices currently available to us. Repeat experiments found the anomalous signals to be reproducible between experiments, which proves that some physical phenomena is responsible but provides us with no clear way to adjust our measurements to learn more. Another device in the same cell showing similar features would be very helpful, as it would allow us to compare and contrast between the two sets of plateaus at the same time. Without an understanding of the origin of the plateaus we cannot engineer this ourselves however, meaning a deeper knowledge if this phenomenon remains out of reach for now.

Due to the ambiguity surrounding the origin of these plateaus, it is very difficult to predict whether or not they will be an issue for measurements using NEMS in ^3He . Since most observations of similar phenomena occur using highly sensitive probes, the extra sensitivity possible using NEMS may prove to have negative consequences by increasing the probability of observing these effects. In the long term this may not necessarily prove to be a bad thing however, as each additional device capable of observing these plateaus gives us an additional chance to investigate.

One of the most confusing aspects of the plateaus is that they are clearly visible on some wires but completely absent on other more or less identical oscillators. Perhaps the most compelling explanation attributes this to differences in roughness of the oscillators on a microscopic scale, with such difference common in almost all devices used. While this roughness is likely to still be present in NEMS the differences in the scale of the devices should significantly affect the types of roughness possible.

Additionally, due to the vastly more precise methods used to produce NEMS, it is likely that these devices will be significantly smoother on a microscopic scale when compared to vibrating wires. Whether these changes make the observation of plateaus more or less likely is hard to predict. Either case is likely to be beneficial however. If plateaus are not seen, results obtained using NEMS will be easier to interpret and these objects will prove useful as precise probes for future studies. If plateaus are seen more regularly we are more likely to be able to perform a more detailed study on this phenomenon, hopefully revealing the underlying mechanism.

8 Conclusions

In this thesis, we have described a significant amount of background work, performed in the hope of laying some of the groundwork for a future improvement of the quasiparticle camera used for imaging turbulence in ^3He . In an effort to improve the instrumentation,

we have tested a new method for rapidly measuring the properties of a resonance. This method, referred to as a frequency comb, uses a multiple frequency lock-in amplifier to excite 40 frequencies equally spaced around the resonance simultaneously.

This allows us to determine the properties of the resonance in a single measurement, and has been shown to produce accurate results in as little as 15 s. In terms of future applications by far the biggest potential advantage is provided by this increase in measurement speed. The most obvious use for a frequency comb is as a rapid way of performing the resonance measurements necessary to calibrate the oscillators in the cell at the start of a new cooldown.

Next, we report on the first successful use of a nanomechanical resonator as an experimental probe in liquid helium ^4He . Measurements of the oscillator resonance from 4.2 K down to 1.3 K clearly show the influence of the liquid. Little variation is seen in the resonance properties between 4.2 K and 2.2 K, with rapid change seen below the transition to superfluid. An attempt to fit a hydrodynamic damping model to the measured resonance properties across this temperature range was mostly successful, with fits to the shift in resonance frequency fitting well. Fits to the width match well throughout the majority of the temperature range but diverge somewhat below approximately 1.7 K. This disagreement is attributed to the size of the oscillators, as the width is of similar size to the viscous penetration depth at low temperatures, violating one of the assumptions used to derive the applied model.

Despite this issue, this result is an important foundation for future uses of NEMS in quantum fluids research, proving that nanoscale devices can be used in a superfluid. Although unlikely to replace tuning forks as the resonator of choice when convenience is required, the promise of increased sensitivity should present a wide range of situations in specialist experiments where NEMS prove very useful. With regards to the quasiparticle camera the most exciting opportunity provided by NEMS is miniaturisation, which could lead to

significantly increased spatial resolution.

Using the NEMS, we have also obtained force-velocity characteristics for the 25 μm beam that show an increase in drag resembling the transition to a turbulent state. Unfortunately the measured critical velocity of 7.2 mms^{-1} is very different to the value of 1.76 ms^{-1} predicted theoretically using the device properties. All other evidence is consistent with the generation of turbulence however, so we cannot say for certain yet if the result is genuine or not. The most obvious way to move forward is to attempt similar measurements using different sizes of beam to see if the experimental results can be reproduced.

We have also used a range of different devices to investigate the effects of frequency on the thermal damping component of drag in ^3He in the low temperature limit. By using the first overtone mode of a tuning fork, we have managed to exceed the limit at which the theoretical model applied is expected to break down. Surprisingly the model still seems to be applicable beyond this limit, though the thermal component investigated appears to become less prominent for high frequency oscillators. Since the relevant limiting condition depends on device dimension as well as frequency, the NEMS devices applied earlier are predicted to fall well below the limit and so should be well described by the current theoretical model. This is promising as it implies we may be able to successfully interpret measurements of the drag taken using NEMS in ^3He without requiring large amounts of additional theoretical work.

Finally, we have also investigated observations of additional drag in superfluid ^3He that cannot be explained using the current theoretical approach. Measurements show that the anomalous plateaus seen in the force-velocity plots are highly reproducible using one resonator and completely absent from other nominally identical oscillators.

In an effort to understand the physical origin of these results, both vorticity production and excitation emission have been investigated as potential explanations. Calculations show both are numerically plausible. In terms of vorticity a vortex ring of approximate

length $7\ \mu\text{m}$ would need to be produced every 21 oscillator cycles to account for the energy lost due to the anomalous damping. This corresponds to 21 rings per second, a result that appears believable.

In terms of excitations, approximately 6.3×10^{10} quasiparticles would need to be created per second to balance out the lost energy. This is roughly equal to the total number of thermal excitations present at the temperature of this measurement. Further interpretation is difficult however as the rate of change of thermal excitation density is not known. In light of this, and considering the theoretical difficulty in justifying excitation production below the transition to pair breaking, we conclude that the anomalous damping is most likely caused by the generation of vorticity.

Further experimental investigation of this phenomenon is difficult, as only two devices have been observed exhibiting this behaviour. The only devices currently known to produce these plateaus are a vibrating wire with diameter $0.9\ \mu\text{m}$ [77] and the $4.5\ \mu\text{m}$ diameter discussed here. As these are the most sensitive resonators currently used, it is possible some NEMS may also demonstrate this behaviour, potentially providing us with a new avenue for further investigation of this unusual phenomenon.

References

- [1] W. F. Vinen and J. J. Niemela, *J. Low Temp. Phys.* **128**, 167 (2002)
- [2] L. Skrbek and K. R. Sreenivasan, *Phys. Fluids* **24**, 011301 (2012)
- [3] W. F. Vinen, *Proc. Roy. Soc. A* **240**, 114, (1957)
- [4] W. F. Vinen, *Proc. Roy. Soc. A* **240**, 128, (1957)
- [5] M. R. Smith et al, *Phys. Rev. Lett.* **71**, 2583 (1993)
- [6] J. Maurer and P. Tabeling, *Europhys. Lett.* **43**, 29 (1998)

- [7] E. A. L. Henn et al, *Phys. Rev. Lett.* **103**, 045301 (2009)
- [8] J. A. Seman et al, *Laser Phys. Lett.* **8**, 691 (2011)
- [9] S. N. Fisher et al, *Phys. Rev. Lett.* **86**, 244 (2001)
- [10] D. I. Bradley et al, *Phys. Rev. Lett.* **93**, 235302 (2004)
- [11] S. N. Fisher et al, *Proc. Natl. Acad. Sci. USA* **111**, 4659 (2014)
- [12] S. L. Ahlstrom et al, *J. Low Temp. Phys.* **175**, 725 (2014)
- [13] P. Kapitza, *Nature* **141**, 74 (1938)
- [14] J. F. Allen and A. D. Misener, *Nature* **141**, 75 (1938)
- [15] L. Tisza, *Nature* **141**, 913 (1938)
- [16] L. Landau, *Phys. Rev.* **60**, 356 (1941)
- [17] C. Enss and S. Hunklinger, *Low-Temperature Physics*, Springer, 2010
- [18] J. Jäger, B. Schuderer and W. Schoepe, *Phys. Rev. Lett.* **74**, 566 (1995)
- [19] H. Yano et al, *Phys. Rev. B* **75**, 012502 (2007)
- [20] R. Goto et al, *Phys. Rev. Lett.* **100**, 045301 (2008)
- [21] D. I. Bradley et al, *J. Low Temp. Phys.* **154**, 97 (2009)
- [22] E. J. Yarmchuk, M. J. V. Gordon and R. E. Packard, *Phys. Rev. Lett.* **43**, 214 (1979)
- [23] G. P. Bewley, D. P. Lathrop and K. R. Sreenivasan, *Nature* **441**, 588 (2006)
- [24] D. I. Bradley et al, *J. Low Temp. Phys.* **138**, 493 (2005)
- [25] H. Yano et al, *J. Low Temp. Phys.* **138**, 561 (2005)
- [26] R. Blaauwgeers et al, *J. Low Temp. Phys.* **146**, 537 (2007)

- [27] J. Salort et al, *Phys. Fluids* **22**, 125102 (2010)
- [28] N. Hashimoto et al, *Phys. Rev. B* **76**, 020504 (2007)
- [29] D. D. Awschalom and K. W. Schwarz, *Phys. Rev. Lett.* **52**, 49 (1984)
- [30] W. I. Glaberson and R. J. Donnelly, *Phys. Rev.* **141**, 208 (1966)
- [31] W. H. Zurek, *Nature* **317**, 505 (1985)
- [32] D. I. Bradley et al, *Phys. Rev. B* **85**, 014501 (2012)
- [33] A. Salmela, J. Tuoriniemi and J. Rysti, *J. Low Temp. Phys.* **162**, 678 (2011)
- [34] D. Schmoranzler et al, *J. Low Temp. Phys.* **163**, 317 (2011)
- [35] R. J. Donnelly and C. F. Barenghi, *J. Phys. Chem. Ref. Data* **27**, 1217 (1998)
- [36] E. R. Dobbs, *Helium Three*, Oxford University Press, 2000
- [37] L. Landau, *Zh. Eksp. Teor Fiz.* **30**, 1058 (1956)
- [38] L. Landau, *Zh. Eksp. Teor Fiz.* **32**, 59 (1957)
- [39] L. Landau, *Zh. Eksp. Teor Fiz.* **35**, 97 (1958)
- [40] J. Bardeen, L. N. Cooper and J. R. Schrieffer, *Phys. Rev.* **108**, 1175 (1957)
- [41] D. Vollhardt and P. Wölfle, *The Superfluid Phases of Helium 3*, Dover, 2013
- [42] P. W. Anderson and P. Morel, *Phys. Rev.* **123**, 1911 (1961)
- [43] R. Balian and N. R. Werthamer, *Phys. Rev.* **131**, 1553 (1963)
- [44] P. W. Anderson and W. F. Brinkman, *Phys. Rev. Lett.* **30**, 1108 (1973)
- [45] J. C. Wheatley, *Rev. Mod. Phys.* **47**, 415 (1975)
- [46] R. Blaauwgeers et al, *Nature* **404**, 471 (2000)

- [47] S. Autti et al, *Phys. Rev. Lett.* **117**, 255301 (2016)
- [48] P. J. Hakonen et al, *Phys. Rev. Lett.* **51**, 1362 (1983)
- [49] J. P. Pekola et al, *Phys. Rev. Lett.* **53**, 583 (1984)
- [50] E. V. Thuneberg, *Phys. Rev. Lett.* **56**, 359 (1986)
- [51] O. V. Lounasmaa and E. Thuneberg, *Proc. Natl. Acad. Sci. USA* **96**, 7760 (1999)
- [52] V. Eltsov, R. Hänninen and M. Krusius, *Proc. Natl. Acad. Sci. USA* **111**, 4711 (2014)
- [53] D. I. Bradley et al, *Nat. Phys.* **7**, 473 (2011)
- [54] G. E. Volovik and M. A. Zubkov, *J. Low Temp. Phys.* **175**, 486 (2014)
- [55] Y. Okuda and R. Nomura, *J. Phys. Condens. Matter* **24**, 343201 (2012)
- [56] K. K. Nummila, J. T. Simola and J. S. Korhonen, *J. Low Temp. Phys.* **75**, 111 (1989)
- [57] C. A. M. Castelijns et al, *Phys. Rev. Lett.* **56**, 69 (1986)
- [58] D. I. Bradley et al, *Nature Phys.* **12**, 1017 (2016)
- [59] C. J. Lambert, *Physica B* **165/166**, 653 (1990)
- [60] C. J. Lambert, *Physica B* **178**, 294 (1992)
- [61] S. N. Fisher et al, *Phys. Rev. Lett.* **63**, 2566 (1989)
- [62] D. I. Bradley et al, *J. Low Temp. Phys.* **157**, 476 (2009)
- [63] T. P. Burg et al, *Nature* **446**, 1066 (2007)
- [64] J. Chaste et al, *Nature Nanotech.* **7**, 301 (2012)
- [65] J. Moser et al, *Nature Nanotech.* **9**, 1007 (2014)
- [66] D. I. Bradley et al, *J. Low Temp. Phys.* **161**, 536 (2010)

- [67] S. Holt and P. Skyba, *Rev. Sci. Instrum.* **83**, 064703 (2012)
- [68] E. A. Tholén et al, *Rev. Sci. Instrum.* **82**, 026109 (2011)
- [69] D. Platz et al, *Appl. Phys. Lett.* **92**, 153106 (2008)
- [70] D. Platz et al, *Nanotechnology* **23**, 265705 (2012)
- [71] C. Bäuerle et al, *Phys. Rev. B* **57**, 14381 (1998)
- [72] D. I. Bradley et al, *J. Low Temp. Phys.* **184**, 1080 (2016)
- [73] R. Hänninen, M. Tsubota and W. F. Vinen, *Phys. Rev. B* **75**, 064502 (2007)
- [74] R. Hänninen and W. Schoepe, *J. Low Temp. Phys.* **153**, 189 (2008)
- [75] A. M. Guénault et al, *Phys. Rev. B* **100**, 104526 (2019)
- [76] A. W. Baggaley et al, *Phys. Rev. Lett.* **115**, 015302 (2015)
- [77] D. I. Bradley, *Phys. Rev. Lett.* **84**, 1252 (2000)